3-D SEISMIC SURVEY DESIGN VIA MODELING AND REVERSE TIME MIGRATION:

PIERCE JUNCTION SALT DOME, TEXAS

A Thesis

Presented to

the Faculty of the Department of Earth and Atmospheric Sciences

University of Houston

In Partial Fulfillment

of the Requirements for the Degree

Master of Science

By

Suleyman Coskun

University of Houston

May, 2014

3-D SEISMIC SURVEY DESIGN VIA MODELING AND REVERSE TIME MIGRATION:

PIERCE JUNCTION SALT DOME, TEXAS

_____

Suleyman Coskun

APPROVED:

_____

Dr. Robert Stewart (Chairman)

_____

Dr. Shuhab Khan (Member)

_____

Dr. Edip Baysal (Member)

_____

Dean, College of Natural Sciences and Mathematics

ACKNOWLEDGEMENTS

I would like to express my deepest appreciation to my advisor, Dr. Stewart for his guidance, understanding, and patience during my research. I am also very thankful to Dr. Shuhab Khan for his support and comments.

My sincere thanks goes to Dr. Edip Baysal for his invaluable guidance and assistance in the preparation of this research. I would also extend my gratitude to Dr. Orhan Yilmaz and Irfan Tanritanir for their great support at Paradigm.

I also acknowledge companies Paradigm, GEDCO, and Geosoft for technical and software support. Texas Brine Company is also thanked for giving AGL the unique opportunity to work in their facility. I sincerely thank the Turkish Petroleum Corporation (TPAO) for financially supporting me throughout my study.

I thank my fellows in University of Houston: Omer Akbas, Unal Okyay, Kenan Yazan, Sercan Pisen, Gokhan Kose, Eray Kocel, Ozbil Yapar, and all AGL members for their all-time support for this research.

I wish to express my great gratitude to my parents, Edip and Sehnaz Coskun, and my brother Gokhan Coskun for their understanding, support, and encouragement.

Finally, and most importantly, it is difficult to find words to express my gratitude for my beloved wife, Selin Deniz Coskun. Her support, encouragement, quiet patience, and

unwavering love inspired me to be successful both in my life and studies. I am also very grateful to her for bringing two adorable sons, Selim and Cihangir, to our family.

3-D SEISMIC SURVEY DESIGN VIA MODELING AND REVERSE TIME MIGRATION:

PIERCE JUNCTION SALT DOME, TEXAS

An Abstract of a Thesis

Presented to

the Faculty of the Department of Earth and Atmospheric Sciences

University of Houston

In Partial Fulfillment

of the Requirements for the Degree

Master of Science

By

Suleyman Coskun

University of Houston

May, 2014

ABSTRACT

Basic seismic survey design parameter calculations are generally useful to image flat layers and slightly dipping surfaces. However, parameter decisions for surveys over complex structures, such as folds, faults, domes, and reefs become more challenging due to complicated wave field behavior in these areas. In this study, another seismic survey design decision method, acquisition design via imaging, is presented using the Pierce Junction salt dome as an example. Pierce Junction is one of the most prolific fields in Texas. Depths of the top of the salt and its overlying cap rock are about 290 m and 210 m, respectively.

Previous studies, 2-D seismic, topography, and gravity data were gathered to build 2-D and 3-D velocity models of the Pierce Junction salt dome area in the south of Houston, Texas. Two-D seismic data acquired by Allied Geophysical Laboratories (AGL) were processed and velocities of the cap rock and near-surface sediments were extracted. Also, 2-D gravity data were collected with 200 m intervals from an 8 km-long gravity profile in study area. The gravity data were processed and modeled in order to be used in 3-D velocity model. Then, a series of analyses were performed on synthetic seismic data to determine 2-D conventional seismic survey parameters that can be achieved with limited acquisition equipment of AGL. Shot gathers were modeled with a finite difference method using the full (two-way) acoustic wave equation. Next, to generate images, Reverse Time Migration (RTM) method was applied to the synthetic data. The optimum parameters of the 2-D seismic survey, such as maximum offset, group and shot interval, recording time,

and profile length, were obtained by reviewing the quality of the results. Finally, it was proposed that a 2-D seismic survey with 20 m group interval, 40 m shot interval, 3000 m maximum offset, 4 s recording time, and 8 km profile length parameters was able to image the salt dome and surrounding sediments adequately.

The optimum parameters of the 2-D survey were modified for a 3-D seismic survey. Survey dimensions and patch definition were determined by the help of obtained 2-D survey parameters. Group and shot intervals were slightly increased to 25 m and 50 m, respectively. The receiver and shot line intervals were determined as 250 m. An orthogonal geometry was chosen due to its cost effectiveness and spatial continuity advantages over the other survey geometries. Eventually, 33 in-lines and 33 cross-lines were uniformly distributed to 8 km by 8 km survey area. Aspect ratio of the patch was kept as 1:1 with 13 in-lines and 13 cross-lines. After determining the final 3-D survey parameters, RTM images were obtained based on the 3-D velocity model. As a result, the final images including cross sections and depth slices showed that the salt dome and its surrounding sediments were adequately imaged with the 3-D survey using Reverse Time Migration analysis.

TABLE OF CONTENTS

CHAPTER ONE: INTRODUCTION

1.1 Motivation and Scope

A seismic project is comprised mainly of data acquisition, processing, and interpretation. The survey design and acquisition somehow determine the quality of processing and interpretation. Even the best processing techniques cannot reveal good results from the data that have some insufficiencies in acquisition. Therefore, processing and interpretation should be considered in survey design and acquisition part of a seismic study.

The goal of designing seismic surveys is to balance the cost of the survey and imaging needs of the interpreter. Expenses, equipment demands, and time limitations of the surveys force geophysicists considering the survey parameters by taking both economical, logistical, and technical parameters into account. A good survey design can be possible by gathering as much information as possible from the survey area.

Stone (1994) summarized two important survey objectives that should be kept in mind while planning a seismic survey as: **(1) Primary objective** to obtain geophysical data that provide a representation of the subsurface geology that is adequate to meet the interpretational goals, and **(2) Secondary objective** to acquire the maximum amount of data within budgeted funds and time available.

Acquisition parameters calculated by general survey design formulas are usually adequate to image flat layers and slightly dipping surfaces. However, determining these parameters for complex structures, such as folds, faults, domes, and reefs is more difficult due to complicated wave field behavior in these areas. Seismic data acquisition simulations over a model of the study area can provide crucial information for determining the survey parameters. If the model is constructed close enough to the real structure, it is possible to obtain very realistic synthetic seismic data using seismic modeling. Therefore, seismic modeling is one of the most economical ways to establish and test the optimum acquisition parameters so as to get the best image over the complex geological structures.

The Pierce Junction salt dome is one of the hundreds of salt domes in U.S. Gulf Coast. Besides oil and gas production, brine production and underground hydrocarbon storage facilities are established in the field. The brine producing caverns are operated by drilling the edge of the salt dome. Adequately imaging the salt dome flanks can reduce the risk of natural disasters such as sinkholes and hydrocarbon seepage. A 2-D seismic study was carried out in the Texas Brine Company facility by Allied Geophysical Laboratories (AGL). New 2-D and 3-D seismic surveys were also proposed since the original 2-D seismic data can only image a portion of the top of the salt. The motivation of this study is to investigate the feasibility of additional 2-D and 3-D seismic surveys for imaging the salt dome flanks and surrounding sediments by AGL's limited equipment.

The scope of this study is to provide a seismic survey design decision method by an acquisition modeling study using the Pierce Junction salt dome area as an example. Two-D and 3-D velocity models of the area were built as close to the real environment as possible and survey design parameters were determined by updating the initial survey parameters with finite difference modeling and Reverse Time Migration (RTM) images.

1.2 Structural Framework of U.S. Gulf Coast

The Gulf of Mexico Basin is an elongated structural basin with a length of about 1,500 km. As shown in Figure 1.1, the offshore part of the basin comprises the Gulf of Mexico which covers an area of more than 1,500,000 km^2 (Salvador, 1991). The abyssal plain (> 3000 m deep) constitutes 20% of the Gulf while, the continental shelf (< 180 m deep), continental slope (180-3000m deep), and shallow and intertidal areas (< 20m deep) comprise 20%, 22%, and 38% of the Gulf, respectively (Gore, 1992).

The offshore area of the basin is bounded by a low coastal plain to the north and west. The low coastal plain is less than 50 km wide in east-central Mexico and more than 550 km wide in the central part of the United States Gulf Coastal Plain, including the states of Louisiana, Mississippi, and Arkansas. Gulfward limits of the shallow parts of the Florida and Yucatan platforms were formed along the Florida and Campeche escarpments where the floor of the Gulf of Mexico rises steeply to the east and south.

The limits of the Gulf of Mexico Basin are defined by existence of the structural features (Figure 1.2). The southern and eastern limits of the basin are estimated to be the Yucatan

and Florida carbonate platforms, respectively. The foot of the Chiapas massif, the Sierra Madre Oriental of Mexico, and the eastern edge of the Coahuila platform, forms the western limit of the basin. The northern limit of the basin corresponds to a series of structural features. These features, from west to east, are the basinward flanks of the Marathon uplift, the Ouachita orogenic belt, the Ouachita Mountains, the Central Mississippi deformed belt, and the southern reaches of the Appalachian Mountains. The limit between Appalachian Mountains and the eastern limit of the basin is arbitrary, since no apparent structural feature separating the shores of the Atlantic Ocean and Atlantic Coastal Plain is observed (Salvador, 1991).

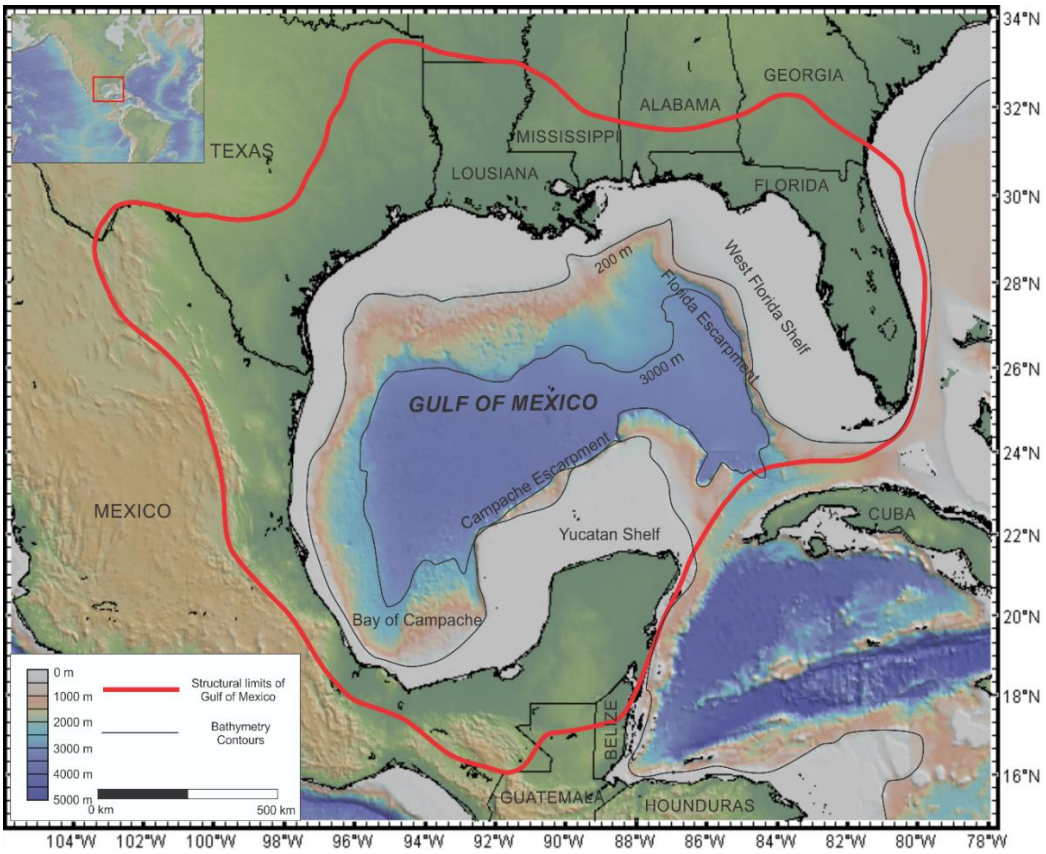

Figure 1.1 Location and structural limits of Gulf of Mexico Basin (modified after Salvador, 1991)

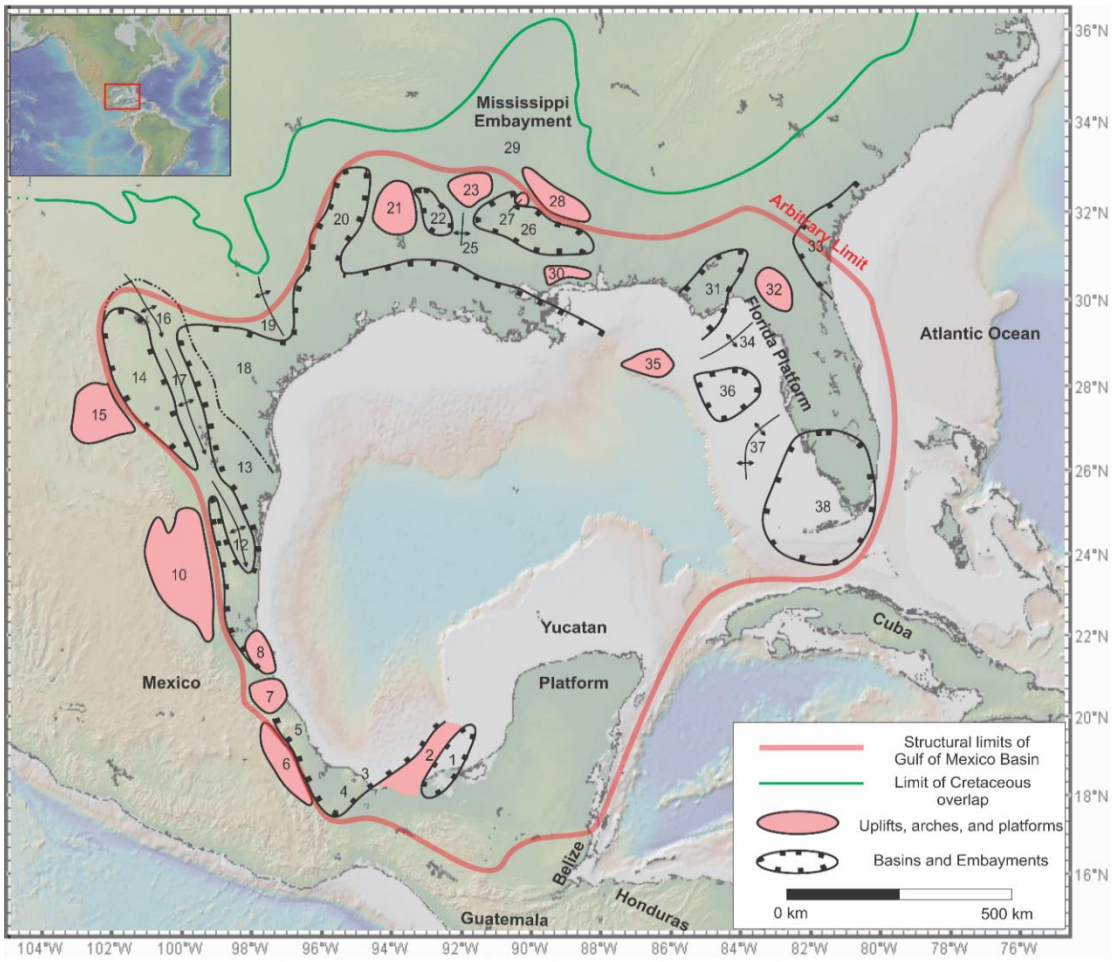

Figure 1.2. Second-order structural features within Gulf of Mexico Basin: 1, Macuspana basin; 2, Villahermosa uplift; 3, Comalcalco basin; 4, Isthmus Saline basin; 5, Veracruz basin; 6, Cordoba platform; 7, Santa Ana massif; 8, Tuxpan platform; 9, Tapica-Misantla basin; 10, Valles-San Luis Potosi platform; 11, Magiscatzin basin; 12, Tamaulipas arch; 13, Burgos basin; 14, Sabinas basin; 15, Coahuila platform; 16, El Burro uplift; 17, Peyotes-Picachos arches; 18, Rio Grande embayment; 19, San Marcos arch; 20, East Texas basin; 21, Sabine uplift; 22, North Louisiana salt basin; 23, Monroe uplift; 24, Desha basin; 25, La Salle arch; 26, Mississippi salt basin; 27, Jackson dome; 28, Central Mississippi deformed belt; 29, Black Warrior basin; 30, Wiggins uplift; 31, Apalachicola embayment; 32, Ocala uplift; 33, Southeast Georgia embayment; 34, Middle Ground arch; 35, Southern platform; 36, Tampa embayment; 37, Sarasota arch; 38, South Florida basin (modified after Salvador, 1991).

The Cenozoic tectonic history of the basin is dominated by salt-related deformation in the Gulf of Mexico. Basinward and landward dipping normal faults, contractional folds and different types of salt structures are the major elements of the salt-related deformation (Figure 1.3). Eight river systems draining into the northern Gulf of Mexico basin, the Norma, Rio Grande, Carriso, Corsar, Houston, Red River, and Central and Eastern branches of the Mississippi River, loaded the sediment in the coastal zone, along with continental shelf and slope (Konyukhov, 2008). Salt flow activity began with the differential loading and gliding the major elements of the driving force of salt flow. A variety of complex structures were formed by deformation caused by the salt flow. A block diagram illustrating schematic shapes of salt structures is shown in Figure 1.4.

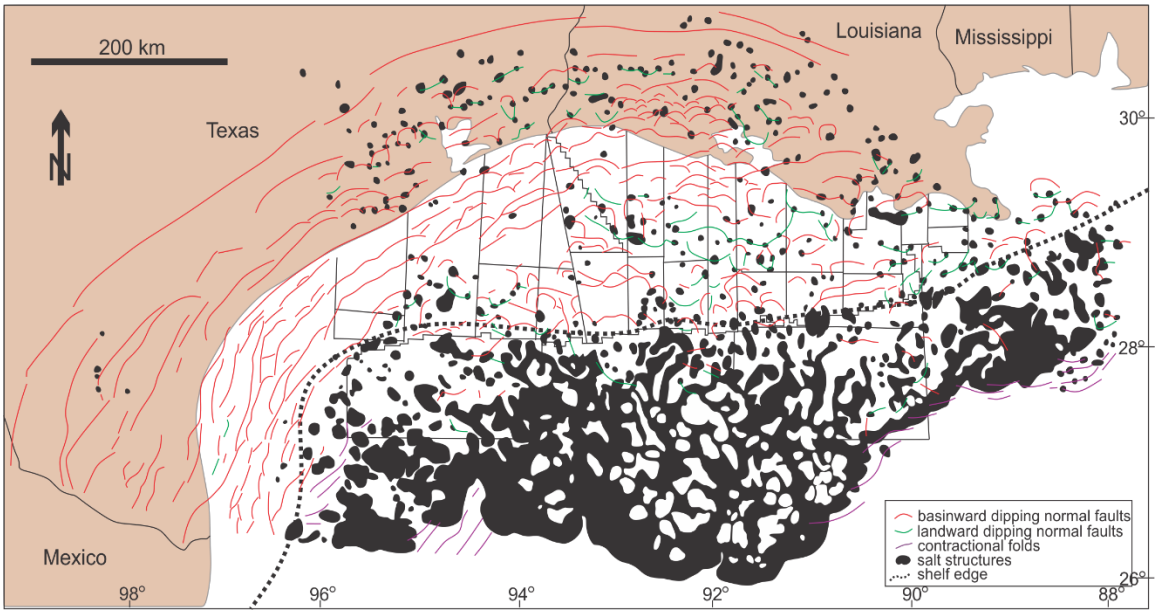

Figure 1.3. Structural elements and salt structures that cause salt-related deformation in the Gulf of Mexico (modified after Konyukhov, 2008).

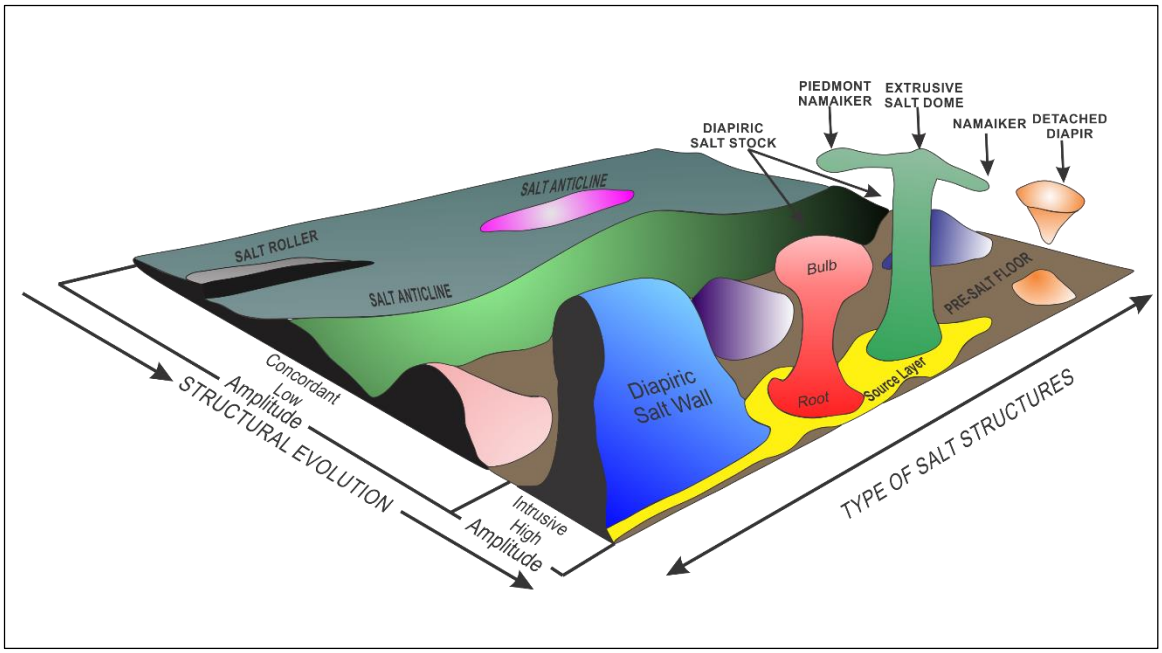

Figure 1.4. Salt structures displaying the evolution of salt tectonics (modified after Jackson and Talbot, 1986)

The Gulf of Mexico can be structurally divided into three major provinces; the northern progradational margin, the eastern carbonate margin, and the western compressional margin (Figure 1.5). The northern progradational margin is the best known part of Gulf of Mexico, since there are extensive oil and gas exploration well data and publications about the area. The northern progradational margin extends from northeastern Mexico to Alabama, and can be subdivided into the interior zone (Mesozoic structures) and the coastal zone (Cenozoic structures). In the interior zone, depositional and active tectonic basins and uplifts, and salt diapirism affected the early mixed clastic-carbonate shelf margin of Late Jurassic and Early Cretaceous age. This zone is also called the interior salt diapir province. In the coastal zone, a thick wedge of Upper Cretaceous and Cenozoic coarse clastic sediments, overlying the Mesozoic strata, have prograded the shelf margin

hundreds kilometers seaward, generating “growth fault” systems and forming the coastal and offshore salt diapir provinces. The Florida and Yucatan carbonate platforms cover the large-scale and poorly known basins and uplifts in the eastern coastal carbonate margins. The western compressional margin covers the area from the Isthmus of Tehuantepec to northeastern Mexico. Laramide (Late Cretaceous-Eocene) folding and thrusting dominated the carbonate margin in the area (Ewing, 1991). Additional discussion will be limited to the northern progradational margin, as it is the main focus of this study.

The interior zone of the northern progradational margin covers a broad complex of embayments, which extends from the San Marcos arch eastward to Alabama. The zone is divided into basin and embayment provinces by the Sabine and Monroe uplifts. The Sabine uplift, located in the center of the embayment, splits the embayment into the East Texas to the west, and North Louisiana and Mississippi salt basins to the east. Also, the Mississippi embayment is separated from the southern basins by the Monroe uplift (Ewing, 1991). Important structural features in the interior zone are, from east to west, the Rio Grande embayment, San Marcos arch, East Texas basin, Sabin uplift, North Louisiana salt basin, Monroe uplift, Desha basin, and Mississippi salt basin.

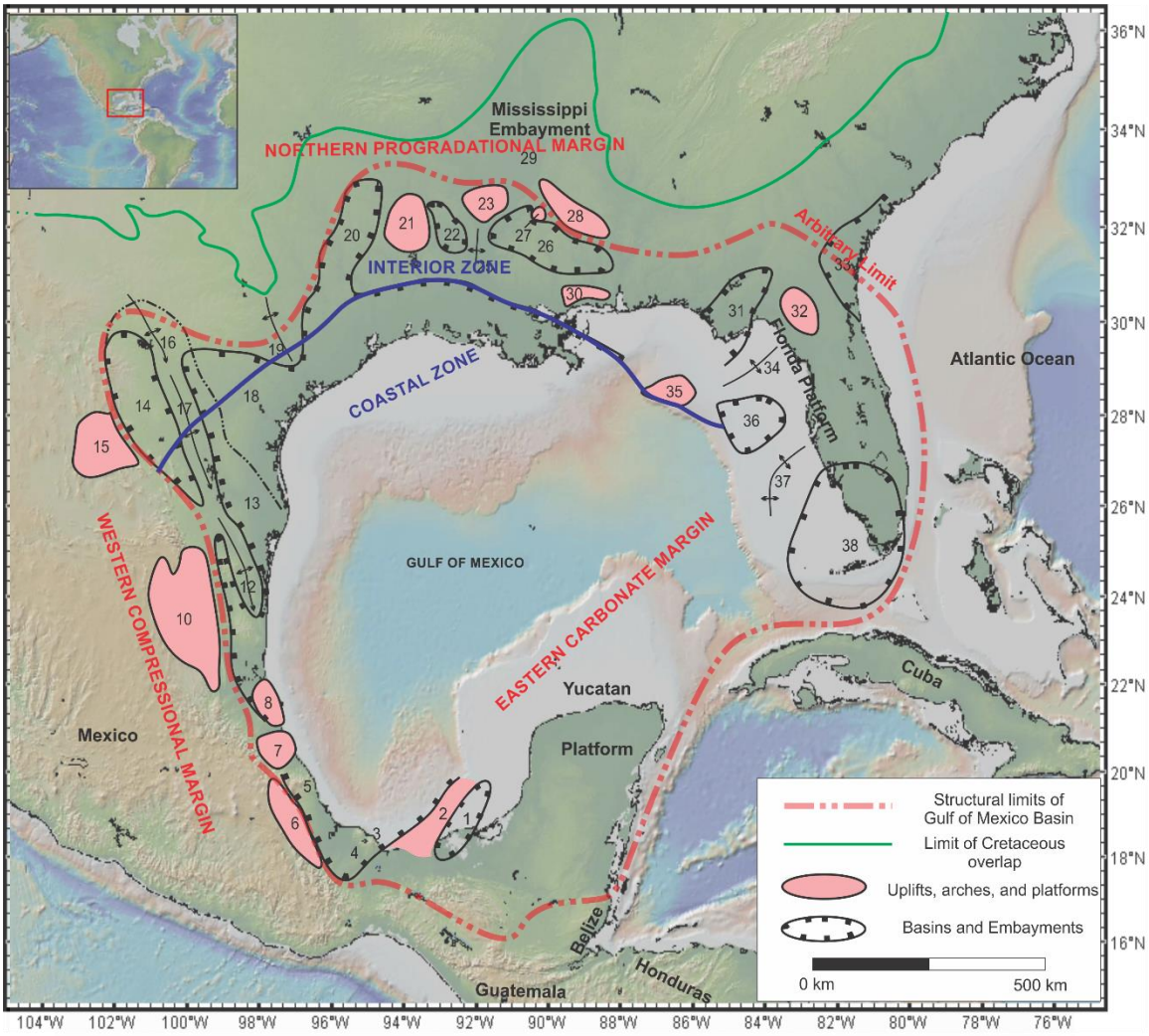

Figure 1.5. Index map showing major structural elements and provinces explained in this chapter. Blue line is the boundary between interior and coastal zone of northern progradational margin. Description of the structural features has given in Figure 1.2 (modified after Ewing, 1991).

The Rio Grande, East Texas, Northern Louisiana, Mississippi, East Central, De Soto Canyon, Texas-Louisiana Slope, Perdido, South Louisiana Shelf, and West Florida salt dome basins are the ten major salt-controlled provinces of the interior and coastal zones of the northern progradational margin (Halbouty, 1967). The difference between styles of

occurrence of salt and/or spatial clustering characterizes these salt diapir provinces. Ewing (1991) states that the salt in diapir provinces may have been deposited in the Jurassic.

The study area, Pierce Junction salt dome, is located in the Houston embayment which is situated in the South Louisiana Shelf diapir province (Figure 1.6). Houston embayment includes about 60 salt diapirs and a few salt pillows. The southern and western boundaries of the province do not contain distinct salt structures. On the other hand, the province merges with the South Louisiana province to the east. The East Texas basin is also connected to the province with a small line of diapirs on the northwest (Ewing, 1991).

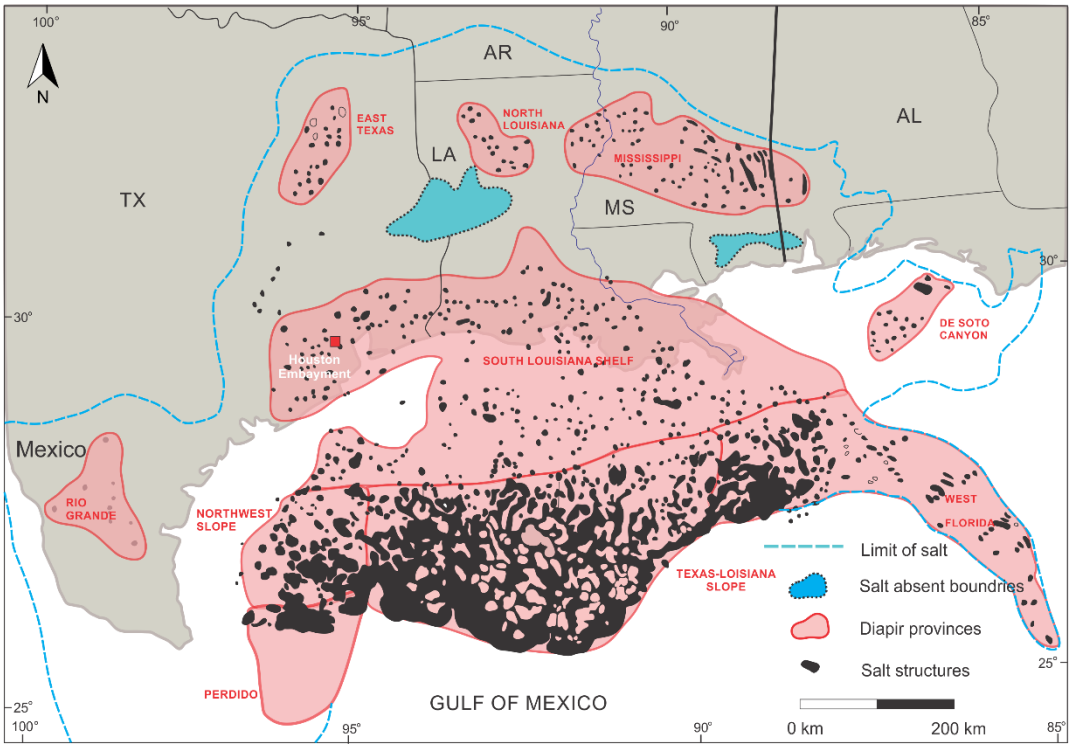

Figure 1.6. Salt diapir provinces of the northern progradational margin. Red square indicates the study area (modified after Ewing, 1991).

1.3 Fundamentals of Salt Dome Geology

1.3.1 Salt Dome Formation

Sedimentary loading after tectonic stability of the Gulf of Mexico caused the development of the salt basins and salt dome basins predominantly in the Gulf Coast region of North America (Halbouty, 1967). Deformation caused by gravity acting on the weak base of abnormally pressured shales and/or salt resulted in two main forms: salt-flow structures and listric-normal faults. Sediments that overlie or load the salt create pressure gradient that provides salt flow. Many types of salt structures were developed by movement of the salt from areas of higher pressure toward areas of lower pressure because of differential loading of the overlaying or loading sediments (Nelson, 1991).

A group of minerals, including both nonradioactive evaporites (halite, anhydrite, gypsum, and trona) and radioactive evaporites (sylvite, carnallite, langbeinite, polyhalite, and kainite), is grouped under the term salt. However, this term is used for halite since the salt contains 90%-98% of this mineral (Kupfer, 1989; Halbouty, 1979). The specific gravity of rock salt is usually greater than the specific gravity of halite (2.164) because of impurities dispersed through the salt. Anhydrite is the most common mineral, which affects the purity of the salt. Hence, average density of the rock salt is often assumed 2.2 g/cc calculated by a salt structure composed of 95% halite and %5 anhydrite. Composition and specific gravity of evaporate minerals are shown in Table 1.1.

Table 1.1. Composition and specific gravity of evaporate minerals (from Carmichael, 1984).

Mineral	Composition	Specific Gravity
Nonradioactive Evaporites		
Halite	NaCl	2.164
Anhydrite	$CaSO_4$	2.960
Gypsum	$CaSO_4 \cdot 2H_2O$	2.320
Trona	$Na_3(CO_3)(HCO_3) \cdot 2H_2O$	2.120
Radioactive Evaporites		
Sylvite	KCL	1.984
Carnallite	$KMgCl_3 \cdot 6H_2O$	1.610
Langbeinite	$K_2Mg_2(SO_4)_3$	2.830
Polyhalite	$K_2MgCa_2(SO_4)_4 \cdot 2H_2O$	2.780
Kalinite	$MgSO_4 \cdot KCl \cdot 3H_2O$	2.130

Salt flow is possible where the driving forces overwhelm the resisting forces. Major driving force of salt flow is differential loading. On the other hand, overburden strength and boundary friction within the salt layer are considered being the principle resisting forces (Hudec and Jackson, 2007). The depth of salt burial, geometry of the salt body, geologic setting, and thermal conditions of the salt determine the type of loading which can be in three ways: gravitational loading, displacement loading, and thermal loading. Combination of the weight of the rocks overlying the salt and gravitational body force within the salt yields the gravitational loading. If the flanks of a salt body are shifted from their original position during a regional shortening or extension, it causes the displacement loading. Thermal loading is a result of deformation in volume of the salt due to changes in temperature (Hudec and Jackson, 2007).

Even though differential loading can be simulated using variety of densities and geometries, it will be beneficial to be illustrated by the condition in which a simple structure is presented on the top of the salt beneath a flat-lying surface. The salt flow direction and the point at which equilibrium is reached is related to the density of the salt and the overlying sediments. Nelson (1991) explained the salt flow mechanism for this model with three cases: sediments in this interval are (1) of the same density as the salt, (2) less dense than the salt, or (3) denser than the salt (Figure 1.7)

In the first case, there is no pressure difference within the salt if the salt and sediment densities are equal; therefore, salt flow cannot be observed in this case. (Figure 1.7a).

In the second case, the density of sediments surrounding local salt high is less than the salt density and the pressure beneath the salt is higher than the pressure beneath adjacent sediments at the same depth. This pressure difference forces the salt to move from local high to salt bed environment (Figure 1.7b). Consequently, the salt high will be suppressed in amplitude and some collisions are observed in the overlying sediment. This case is generally observed where shallow salt sheets are developed.

In the third case, the density of local salt high is smaller than that of adjacent sediments which produces a pressure difference causing the salt flow from the salt bed into the local salt high. As a result of the upward movement of the salt through the local salt high, high-amplitude salt diapirs dominantly seen in Gulf of Mexico basin region are developed (Figure 1.7c)

“Fluid mechanical theory” of Nettleton (1934) basically describes salt-flow principles (Barton, 1933; Halbouty, 1967). According to Nettleton’s theory, initial configuration which localize the dome, the thickness of mother salt layer, the strength or viscosity of overlying rocks, and the strength or viscosity of the salt are the significant factors that determine the final form of a salt dome. Formation of a piercement salt dome can be illustrated in six stages (Figure 1.8). (1) Initial stage of formation doesn’t begin until the deposition of adequate sediments over the salt to produce a pressure difference on the salt bed. (2) While initial upward movement of the salt begins when the sufficient pressure difference is occurred, sediment accumulation still continues. (3) In stage 3, salt piercement through the overburden begins and overlying rocks are carried upward by the salt. Also, drop in the peripheral sink cuts off the salt supply flowing towards the dome. Hence, after this stage formation of the dome will be completed with the amount of the material within the peripheral sink and salt core. (4) At stage four the original material over the dome is almost eroded. (5) After complete erosion of overlying rocks, the cap rock is produced by the action between the salt and circulating ground water. (6) Collision of the upturned beds into the peripheral sink in form of block fault segments shows the final stage of dome growth (Nettleton, 1934; Halbouty and Hardin, 1956; Halbouty, 1967).

Categorizing the salt domes by their forms, sizes, and relationships to host sediments is required to describe the structure better. Salt domes are classified in two ways: descriptively and structurally.

Descriptive classifications refer to: (1) depth of burial of the salt mass below the surface, (2) form or shape of the salt structure, and (3) genetic relationship of salt structure or group of structures. On the other hand, structural classification include the relationship of: (1) the upper portion of the salt to adjacent sediments, (2) the lower portion of the salt mass to the source bed, (3) the salt stock to structural features in adjacent strata, and (4) the salt core to numerous typical fault pattern (Halbouty, 1967).

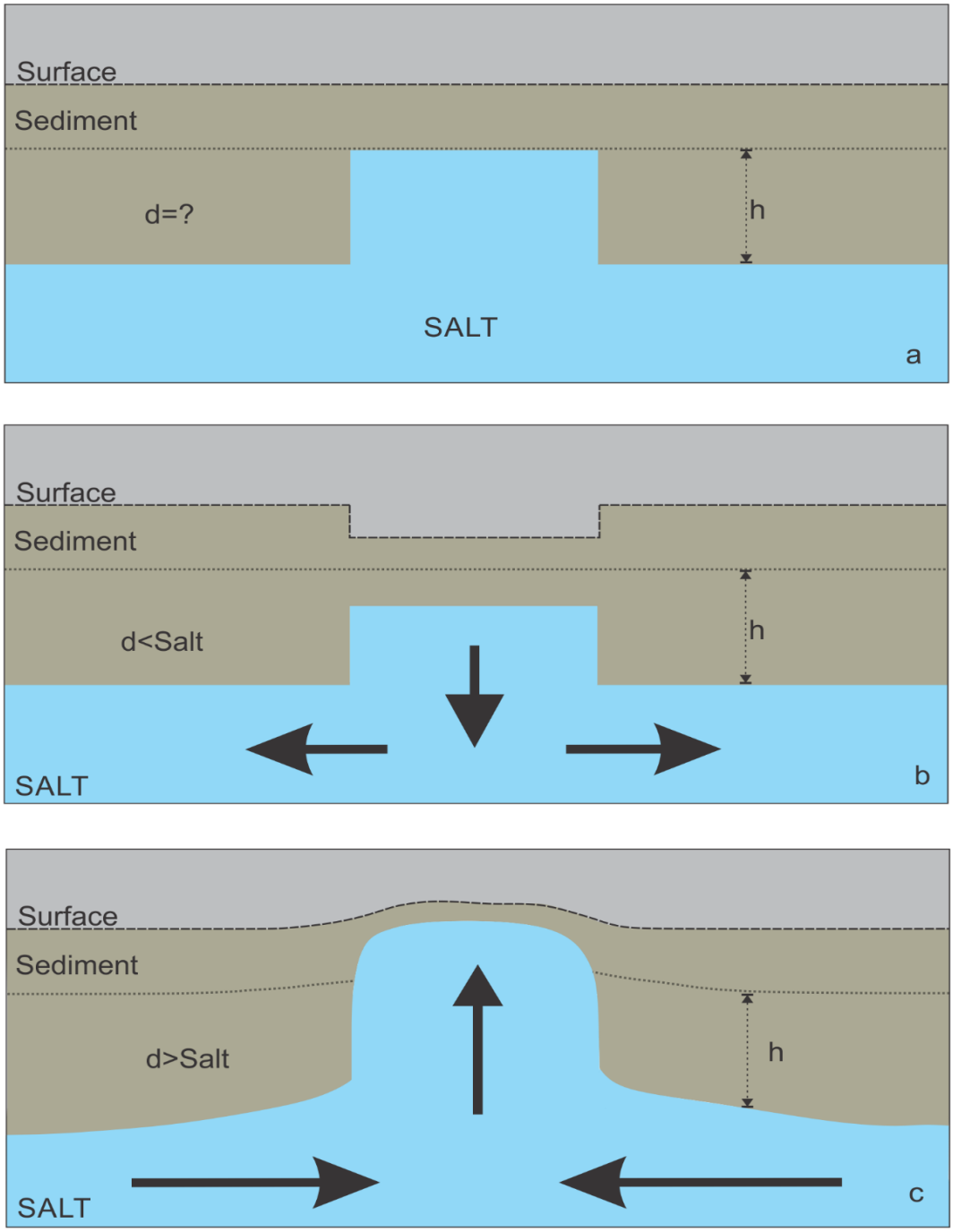

Figure 1.7. Model of differential loading related to structure on the top of the salt; a) Stable condition, b) damping of structural relief on top of the salt, c) model of dipirism. "h" indicates the interval of the overlying sediment (modified after Nelson, 1991).

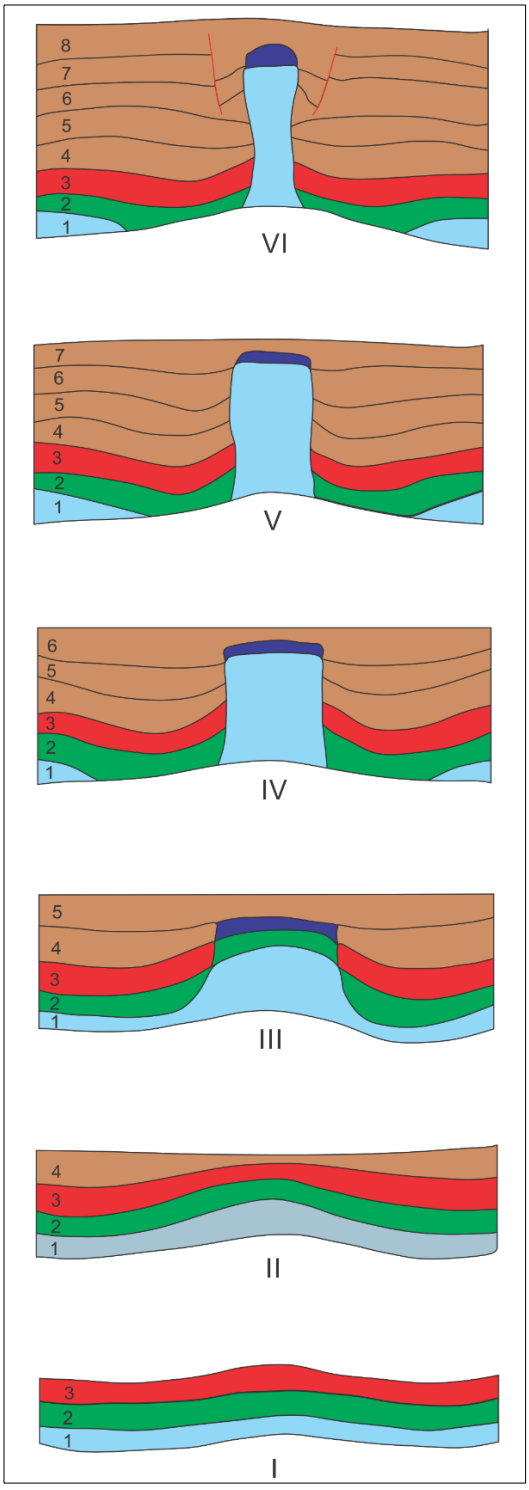

Figure 1.8. Development stages of a shallow piercement salt dome (modified after Nettleton, 1934).

1.3.2 Fault Systems around the Salt Domes

Relative uplift of the sediments flanking the diapir yields to faulting activity around passive piercement salt domes. The reasons of diapir uplift can be accounted to a combination of salt withdrawal from the source layer, continued rise of the salt plug relative to the source layer, and compaction and subsidence of the sediments surrounding the salt plug (Nelson, 1991).

The usual fault patterns around passive piercement salt domes are radial and commonly developed from the salt/sediment interface outward. These faults are larger near the salt plug and become weaker down the flanks of the structure. Relative uplift produces an extensional stress around the circular salt plug. Since the salt plug is biased to move parallel to the salt/sediment interface, the faults are developed perpendicular to that interface in response to the stress (Figure 1.9; Nelson, 1991).

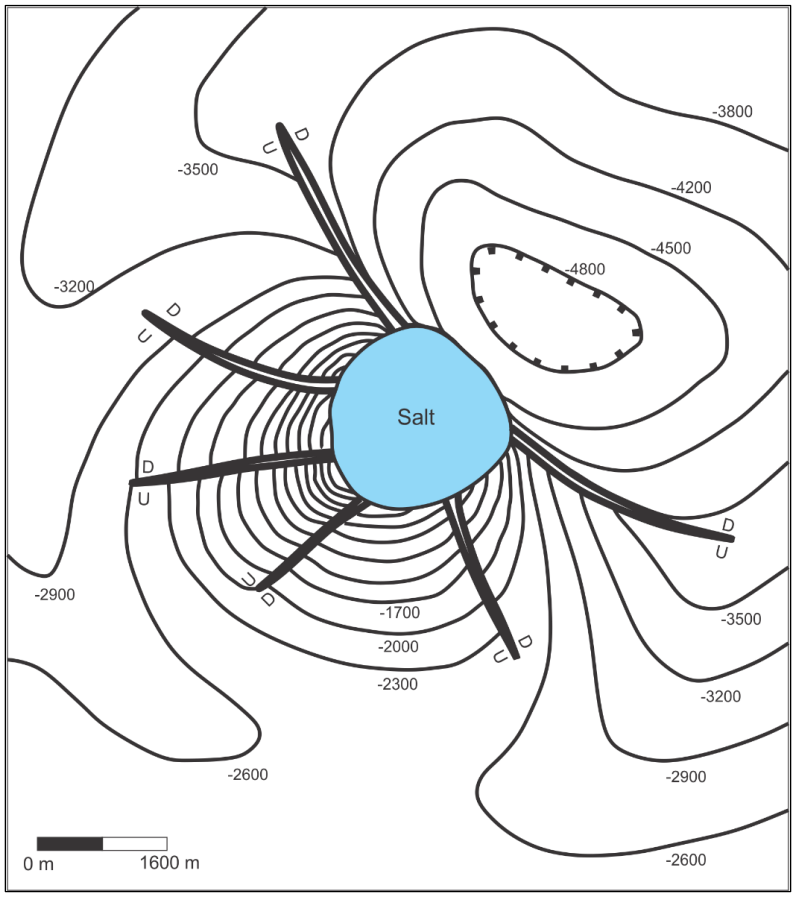

Figure 1.9. Schematic structure map of a sedimentary horizon around a typical piercement salt dome (modified after Nelson, 1991).

1.3.3. The Cap Rock

Cap rocks can be described as layers of anhydrite, gypsum, and calcite that cover the salt plugs of passive piercement domes (Halbouty, 1979). The cross section of a typical cap rock is shown in Figure 1.10. Dissolution of the top of the salt generally by meteoric water yields the formation of the cap rock (Murray, 1961; Posey and Kyle, 1988). Easily soluble minerals, such as halite, are removed under these conditions. Less soluble minerals than halite accumulate more along the salt/cap rock interface through a process called

underplating (Kyle et al., 1987). Biogenic calcite and hydrogen sulfide are originated by bacteria associated chemical reactions of anhydrite and hydrocarbons present in the environment (Feely and Kulp, 1957). In a few situations, elemental sulfur can be formed by conversion of hydrogen sulfide. Hence, elemental sulfur can be preserved and deposited in the cap rock in commercial quantities (Halbouty, 1979).

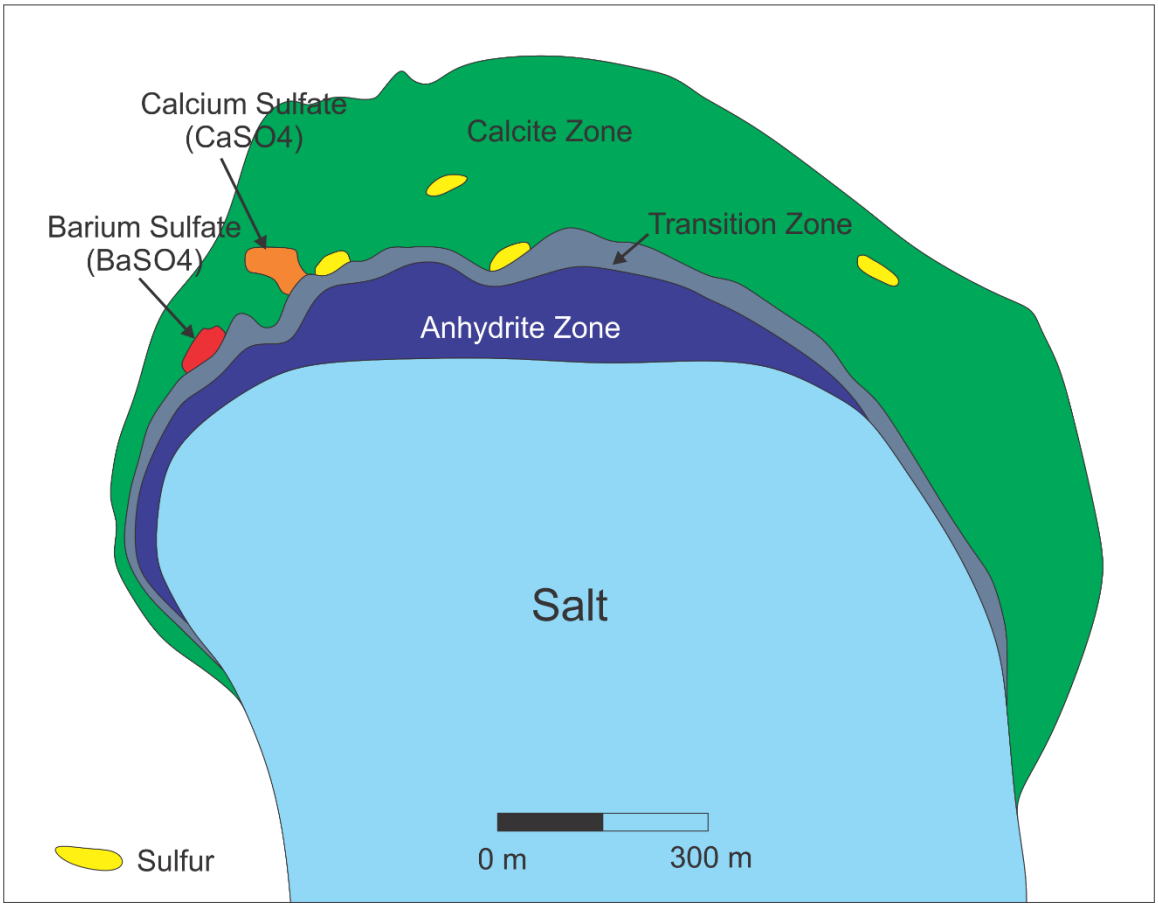

Figure 1.10. Cross section of Jefferson Island dome, Iberia Parish, Louisiana showing three mineralogical zones typical of cap rock on many domes. Accessory minerals such as gypsum and sulfur, if present, are usually associated with the transition and calcite zones overlying the lower anhydrite zone. (modified after Halbouty, 1967).

1.4 Thesis Organization

This thesis consists of six chapters. **Chapter one** introduces the motivation and scope of this study, reviews the structural framework of the Gulf Coast dominated by salt structures, and addresses the fundamentals of the salt dome geology.

Chapter two describes the data and methods used in 2-D and 3-D velocity model building. A detailed information about the Pierce Junction salt dome is presented as a review of previous studies. Next, a series of geophysical data acquired from the area processed and interpreted to gather more information for accurate velocity models.

Chapter three describes the acquisition modeling steps applied in this study. Velocity model building procedures are defined. Then, seismic survey design parameters decision by acquisition modeling is presented. The results and analyzes of the survey designs are also discussed with RTM image examples.

Chapter four discusses the products of this study in terms of feasibility, equipment requirements, and cost of the survey. The problems that can be encountered while acquiring the data in the real environment and their solutions are also discussed in this chapter.

Chapter five addresses the limitations of this study

Chapter six contains a summary and conclusions of this research.

CHAPTER TWO: DATA AND METHODS

2.1 Study Area

The Pierce Junction salt dome is located seven miles southwest of Downtown Houston, in southern Harris County. It is named for its location at the intersection of what was then the Buffalo Bayou, Brazos and Colorado Rivers, and the Houston Tap railroad (Figure 2.1).

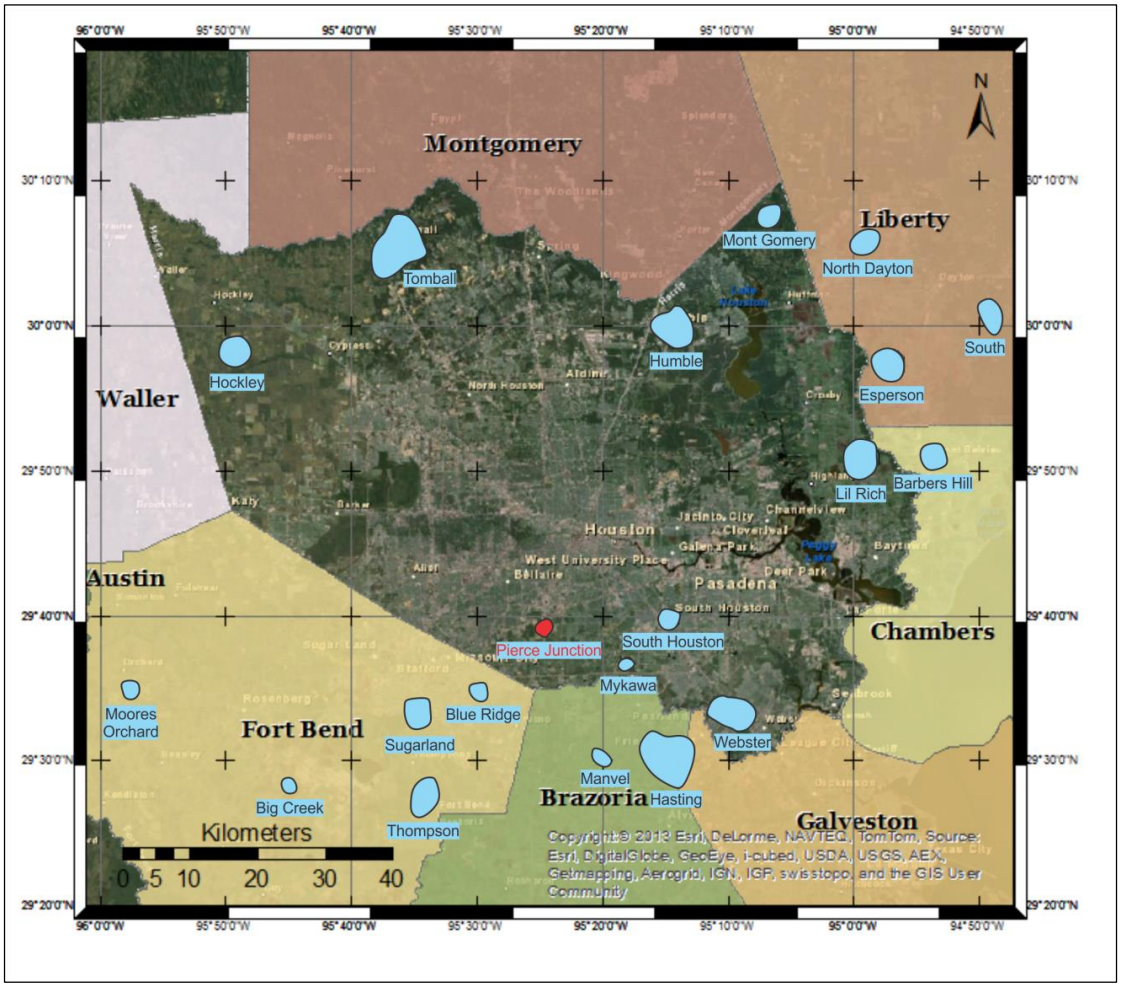

Figure 2.1 Location of Pierce Junction salt dome. Blue polygons represent Gulf Coast salt domes (Huffman, 2004) in the Houston Metropolitan area within Harris County.

The dome is classified as a shallow piercement salt dome. As a typical Gulf Coast salt dome, it is overlain by a cap rock and the salt spine is steep to overhanging. According to Beckman and Williamson (1990), the salt and overlying cap rock are encountered at a depth of approximately 290 m and 207 m, respectively. The dome is almost circular and the area of the top of the salt is about 10 km^2, although it is about 35.25 km^2 at the deepest part (Beckman and Williamson, 1990). Elevation from sea-level differs between 17 and 21 m in the area.

The stratigraphic sequence of formations at the Pierce Junction area is illustrated in Figure 2.2 based on type electric log. Each stratigraphic unit from lower Miocene trough the Jackson contains oil that is mostly accumulated on the flanks of the structure (Glass, 1953). The schematic west-east cross section of the field indicates the stratigraphic convergence and arching of sediment bordering the salt. On the eastern flanks of the dome, in the presence of steeply dipping and overturned beds, the evidence of the increased structural effects of drag between the salt plug and sediment next to it exists beneath the salt overhang (Glass, 1953) (Figure 2.3).

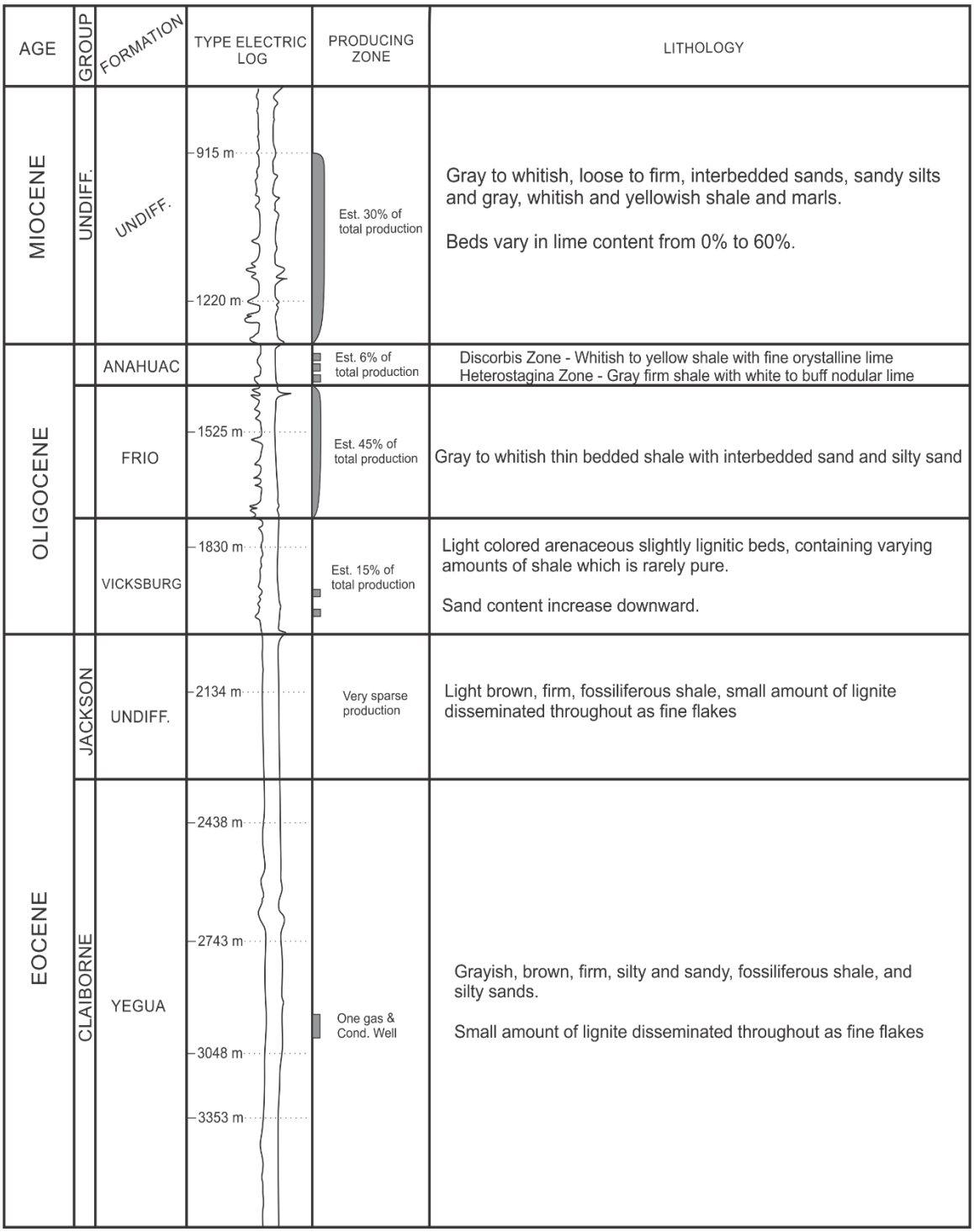

Figure 2.2. Type stratigraphic section of Pierce Junction field (modified after Glass, 1953).

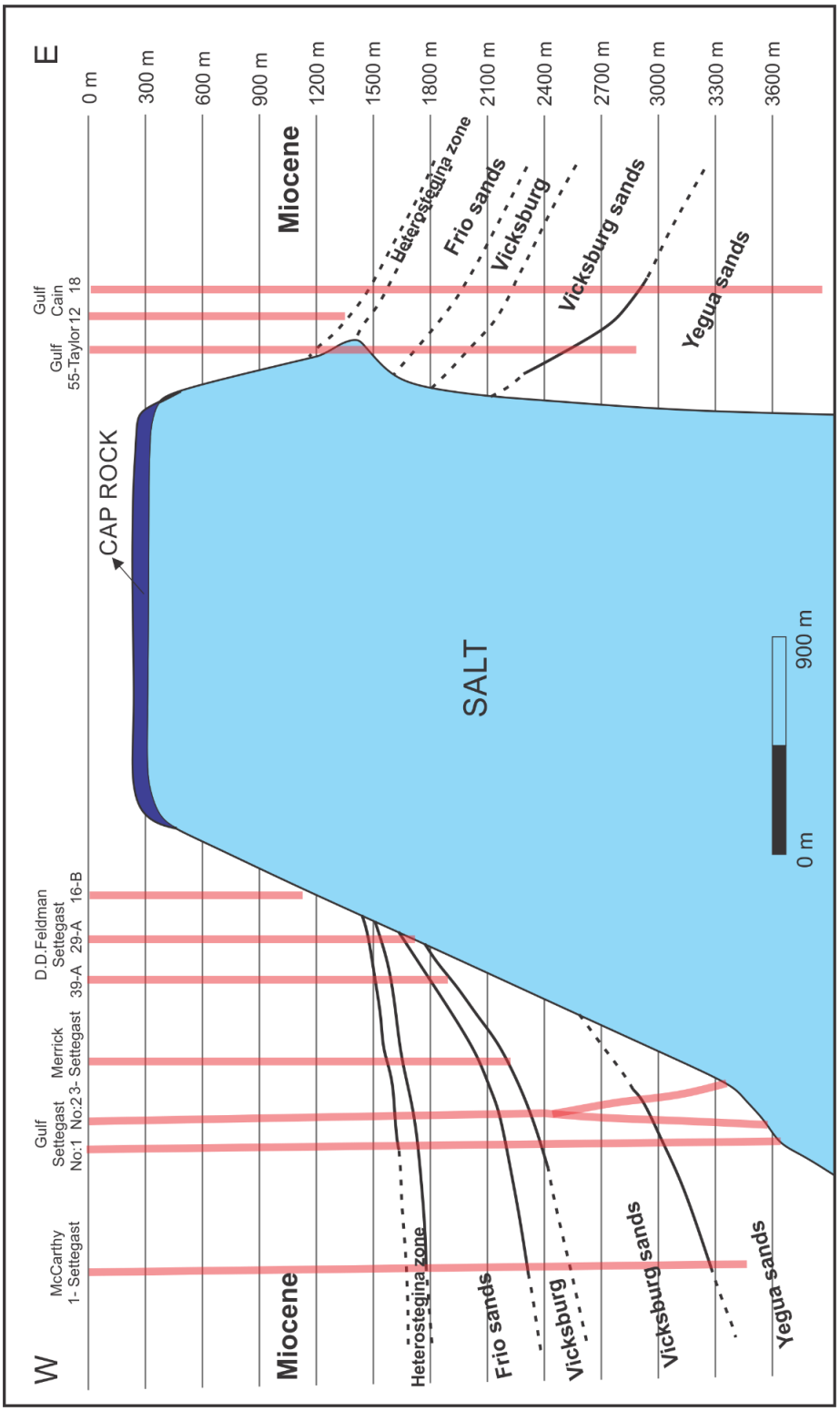

Figure 2.3. West – East Cross section of Pierce Junction salt dome. Line of section and location of the wells are shown on Figure 2.4 (Modified after Glass, 1953)

The radial fault pattern formed by normal faults around the dome can be observed on the contour map of the “heterostegina zone” (Figure 2.4). Throws of those normal faults vary from 15 m to 90 m. Combination of structural effects of faulting and sedimentary movements ends up with a very complex structural pattern at the areas adjacent to the dome. Hence, this complex structure does not provide a reliable structural interpretation at the boundaries of the salt (Glass, 1953).

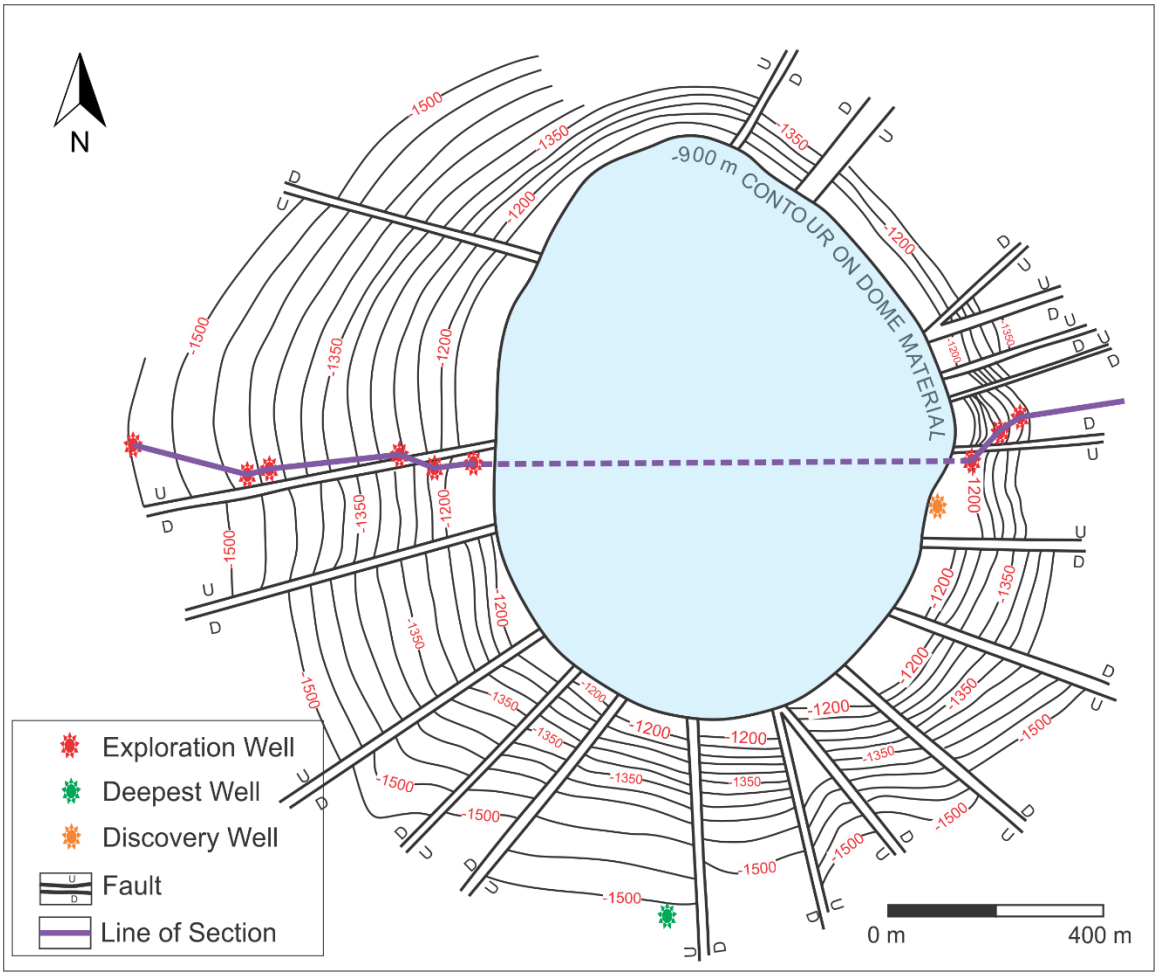

Figure 2.4. Contour map of Top Heterostegina zone around Pierce Junction salt dome (modified after Glass, 1953).

The Pierce Junction salt dome has an important place in oil and gas production history as it is of the earliest oil fields. The salt dome area was evaluated as barely productive in the early 1900s, since the poor drilling technology had not been successful on first fifty four holes. With the developing technology, first production made in 1921 by the South Texas Petroleum Company owned by Hugh Roy Cullen. First, "Taylor" No. 2 gas well completed with a total depth of 1,072 m. Finally, initial flow of 3,000 barrels of oil per day was achieved in the same well at around 1225 m depth. Until the 1930s, 19,637,240 barrels were produced from 86 wells in the area (Darton, 1933; Glass, 1953). Oil production reached its final limits in late 1940s with development of the Vicksburg on the south flank of the dome. In 1950s, the field had produced 40 million barrels of oil with 107 wells producing 4,300 barrels per day in advance stage of depletion. The total oil production until 1979 was recorded as 80 million barrels (Holzer and Bluntzer, 1984). According to Railroad Commission of Texas annual reports, the Pierce Junction salt dome produced 111,232 barrels of oil in 1997. However, the annual production decreased dramatically to 44,375 barrels in 2012. Annual production of the Pierce Junction oil field is depicted in Figure 2.5. Moreover, gas production had continued until 2000 and approximately 15 million cubic feet (Mcf) gas had been produced from the field (Figure 2.6).

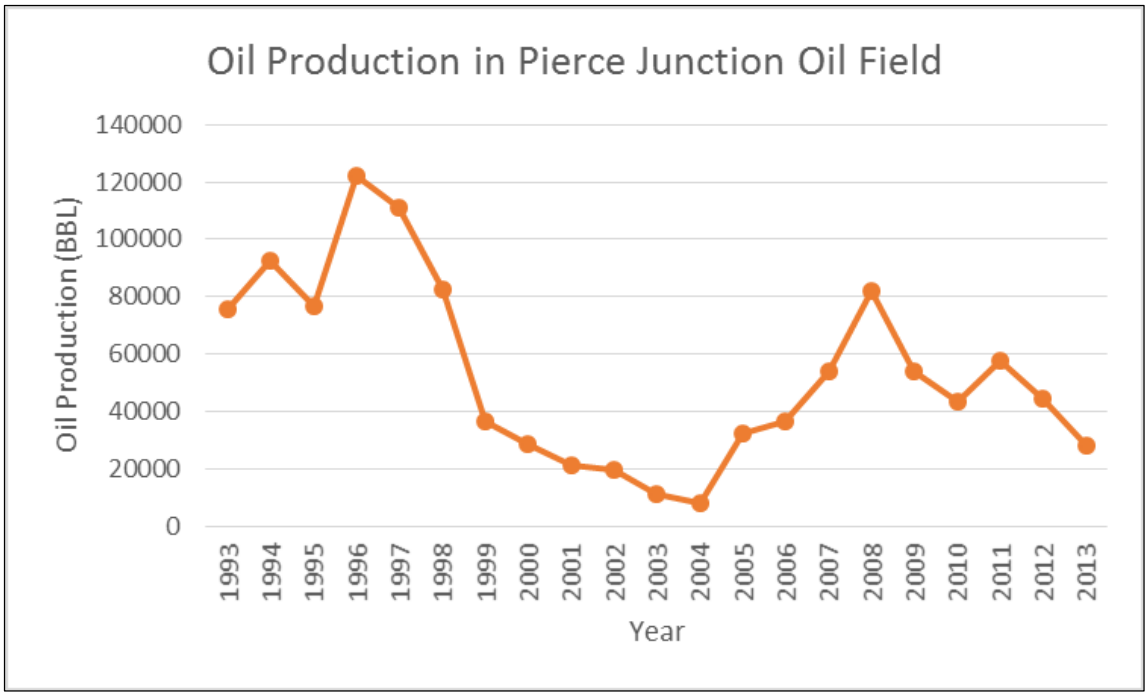

Figure 2.5. Oil Production in Pierce Junction oil field (Railroad Commission of Texas, 2013).

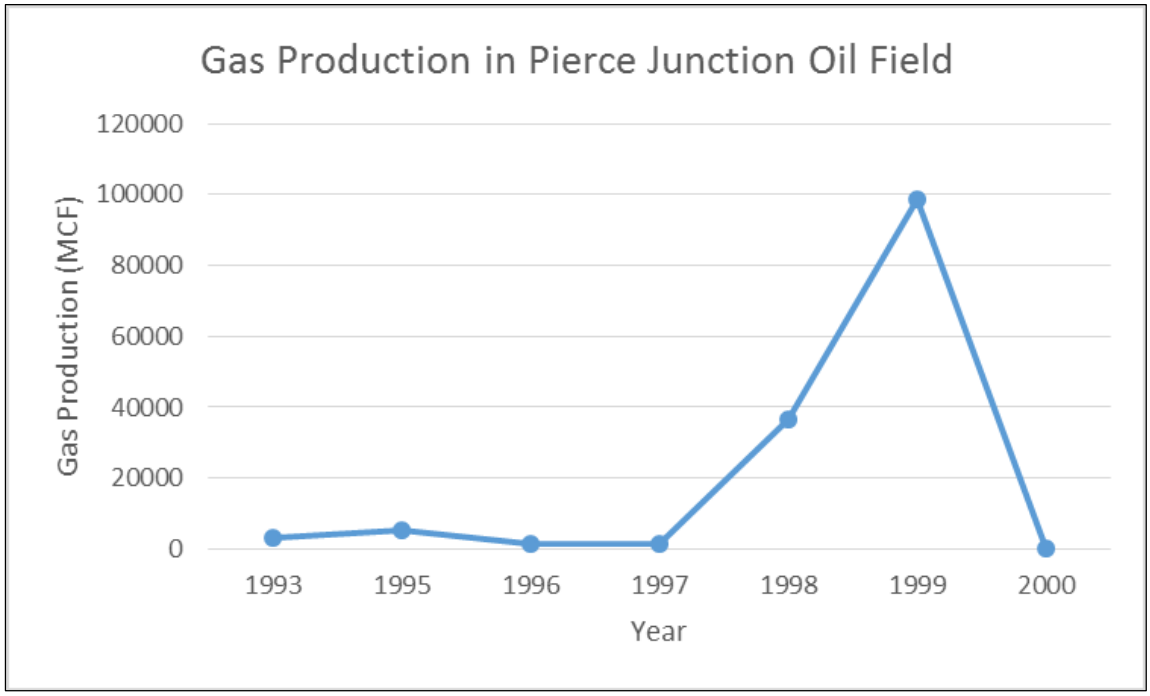

Figure 2.6. Gas Production in Pierce Junction oil field (Railroad Commission of Texas, 2013).

Besides oil production, the Pierce Junction salt dome has been used for brine production and hydrocarbon storage over the last three decades. This field is the first facility where simultaneous brine production and storage is provided in Texas (Querio, 1974; Seni et al., 1984) Materials that do not dissolve salt can be stored in salt caverns securely. Brine production using controlled solution mining provides potential storage caverns in the salt dome (Thomas and Gehle, 2000). Texas Brine Company operates brine production, cavern construction and engineering, and management of storage facilities in the Pierce Junction salt dome.

2.2 Total Station Survey

In 2011, total station survey data were collected at the boundaries of the salt dome for static correction of seismic data.

Total station is a modern electronic/optical surveying instrument that allows reading slope distances from the instrument to a particular point. A total station simply consists of a tripod, a distance measuring device, and a reflector prism (Figure 2.7).

Figure 2.7. Element of the total station survey instrument.

A solid-state emitter within the total station generates an infrared laser signal. This laser signal is then reflected by reflector prism back to the measuring device. The distance between the total station and the reflector prism is calculated by an integrated computer that interprets the modulation pattern of the reflected signal. Most of the total station systems can determine the coordinates and elevation of the point using simple trigonometry and triangulation equations. The data collected from total station survey are used to generate the topographic map of the surveyed area. Total station survey is preferred for detailed studies due to its very high accuracy (~1.5mm).

The survey was carried out at every 5 m where the seismic receivers are deployed in the area (Figure 2.8). Average elevation in the area is about 19 m. Elevation difference

between beginning and end of the line is very small (about 2 meters). The elevation trend decreases slightly from North to South with a slope of about 2° (Figure 2.9).

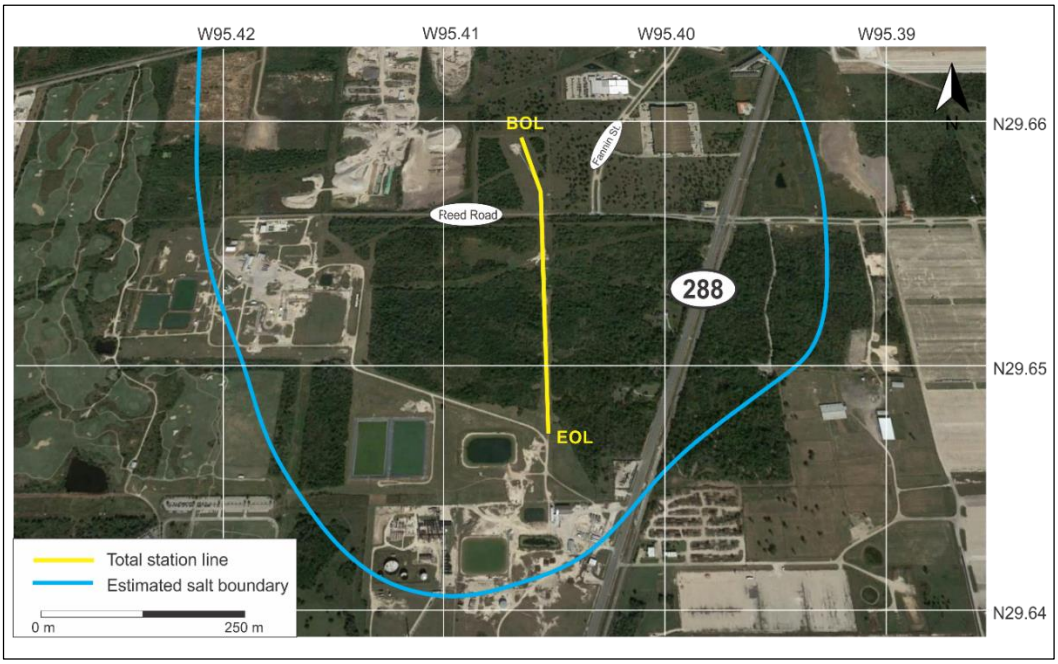

Figure 2.8. Map view of total station survey area. Yellow line represents the total station measurement line and blue line represents the estimated salt boundary (Huang, 2012).

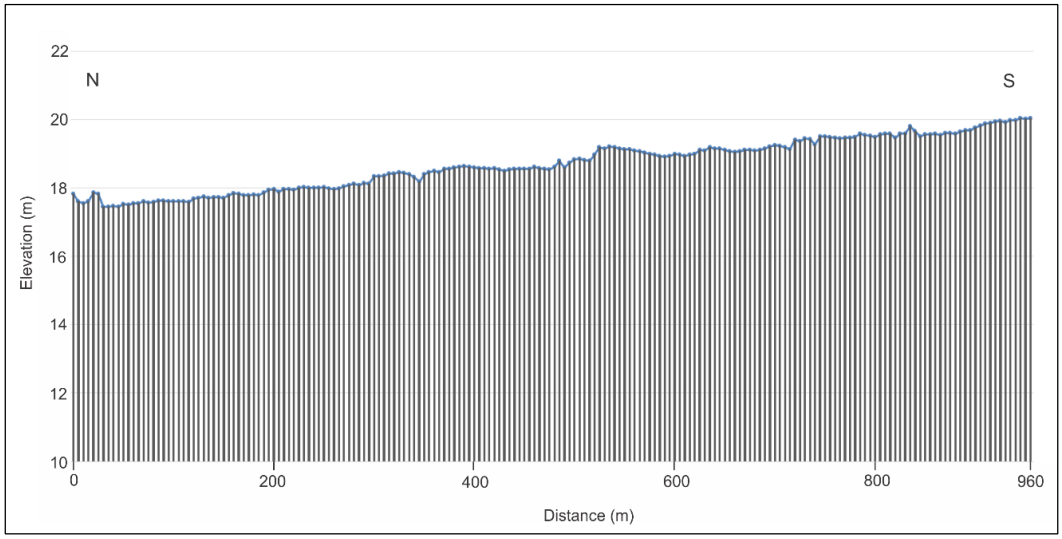

Figure 2.9. Elevation of N-S line in the center of the salt.

2.3 2-D Seismic Data

2.3.1 Seismic Data Acquisition

A 2-D seismic survey was conducted in the central part of the Pierce Junction salt dome in 2011, for the purpose of imaging the top of the salt on the same line of total station survey (Figure 2.8). 120 vertical receivers were deployed with 5-meter interval with the total length of 595 m. After shooting along the line, the receiver line has moved 360 m to the end so as to get t total length of 955 m. AGL's MiniVibe seismic vibrator truck was used as the source. Sweep type was selected as linear sweep from 10 to 120 MHz. Shots were fired between two receiver stations with 5 m interval. Distance between source and receiver lines was remained at 5 m as much as possible. Figure 2.10 represents the receiver line and shot station configuration of seismic survey at the Pierce Junction area.

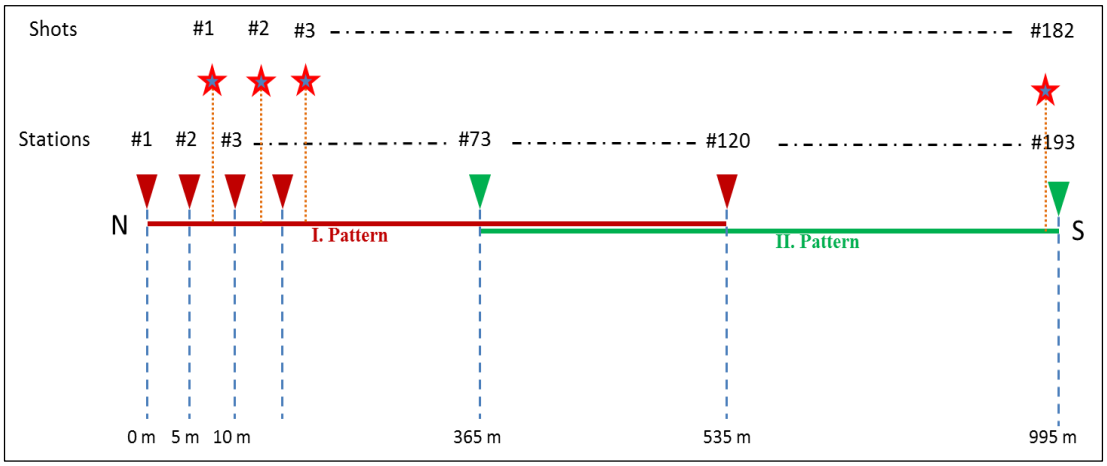

Figure 2.10. Shot and receiver configuration of 2-D seismic survey. Red and green triangles represents the stations of the first pattern, and the stations of the second pattern, respectively. Red stars show shot locations.

2.3.2 Seismic Data Processing

Two-D seismic data from the Pierce Junction salt dome area were processed using Paradigm's Echos seismic processing software. Processing flow of seismic data is shown in Figure 2.11.

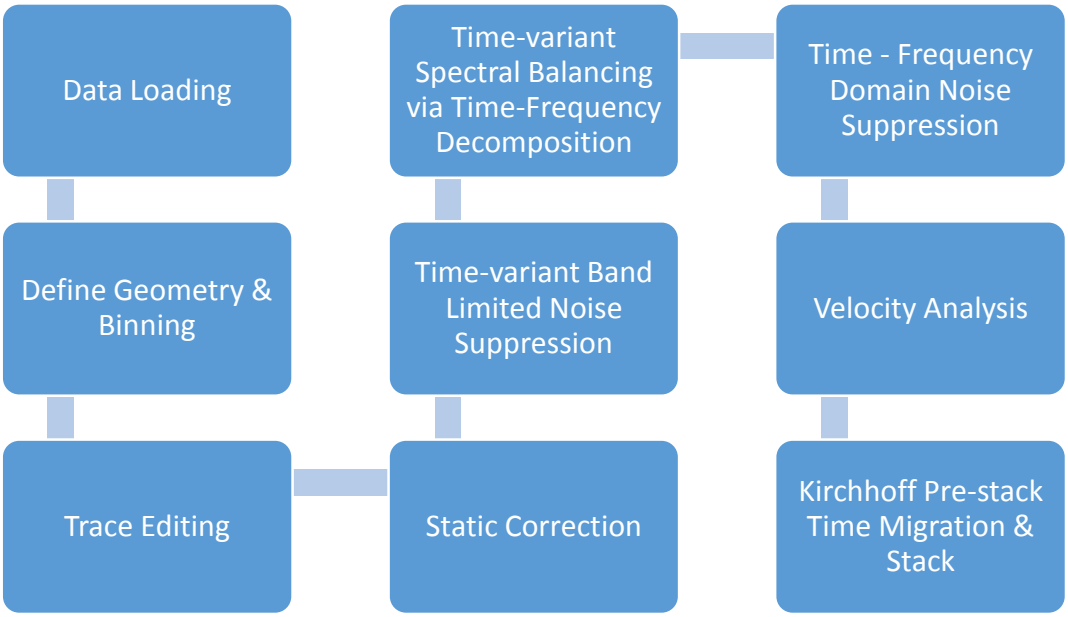

Figure 2.11. Processing work flow of Pierce Junction 2-D seismic data.

The collected data first preprocessed using geometry loading, trace editing, and static correction. A series of noise suppression and filtering methods were also applied in order to eliminate low frequency noise originated from producing wells and random sources.

First, time-variant band-limited noise suppression (SUPPRES module) with 3-20 Hz frequency band is applied to suppress organized type of noise such as ground roll and air blast. In this method, noise and signal components in seismic trace are decomposed using 3-20 Hz Butterworth filter. The noise component of the trace is scaled down through

comparison between noise and signal components to have its envelope to match the specified signal envelope level. The final result was obtained by summation of original signal and scaled noise components (Oppenheim and Schafer, 1989; Robinson and Treitel, 1980; Taner et al., 1979)

Next, time-variant spectral balancing via Time-Frequency decomposition (TUNEUP module) was applied to the data. This method provides replacement of each input trace with the trace that has broader frequency band where the envelopes of the input and output traces are matched. Wavelet transforms using Gabor-Morlet wavelets yield the spectral extension of the trace (Goupillaud et al., 1984; Morlet et al., 1982; Partyka et al., 1999). The power spectrum of a shot gather before and after time-variant spectral balancing is shown in Figure 2.12.

Finally, time-frequency domain noise suppression (TFCLEAN module) was used to eliminate the noise bursts in gathers. This application uses Fast Fourier Transforms to transform the input gather into time-frequency domain, split input gather into its amplitude and phase component, and decompose it to different sub-bands. A noise threshold, calculated automatically by median of frequency sub-bands, was used to scale the noises whose spectral amplitude value exceeds the threshold within the sub-band. Subsequently, unaltered phase information was combined with both scaled and unscaled amplitude information and transformed to filtered time-space domain by inverse Fourier Transform. As a result of sample by sample noise suppression on various frequency

components, nicely balanced spectra was obtained (Goupillaud et al., 1983; Morlet et al., 1982; Partyka et al., 1999; Taner et al., 1979).

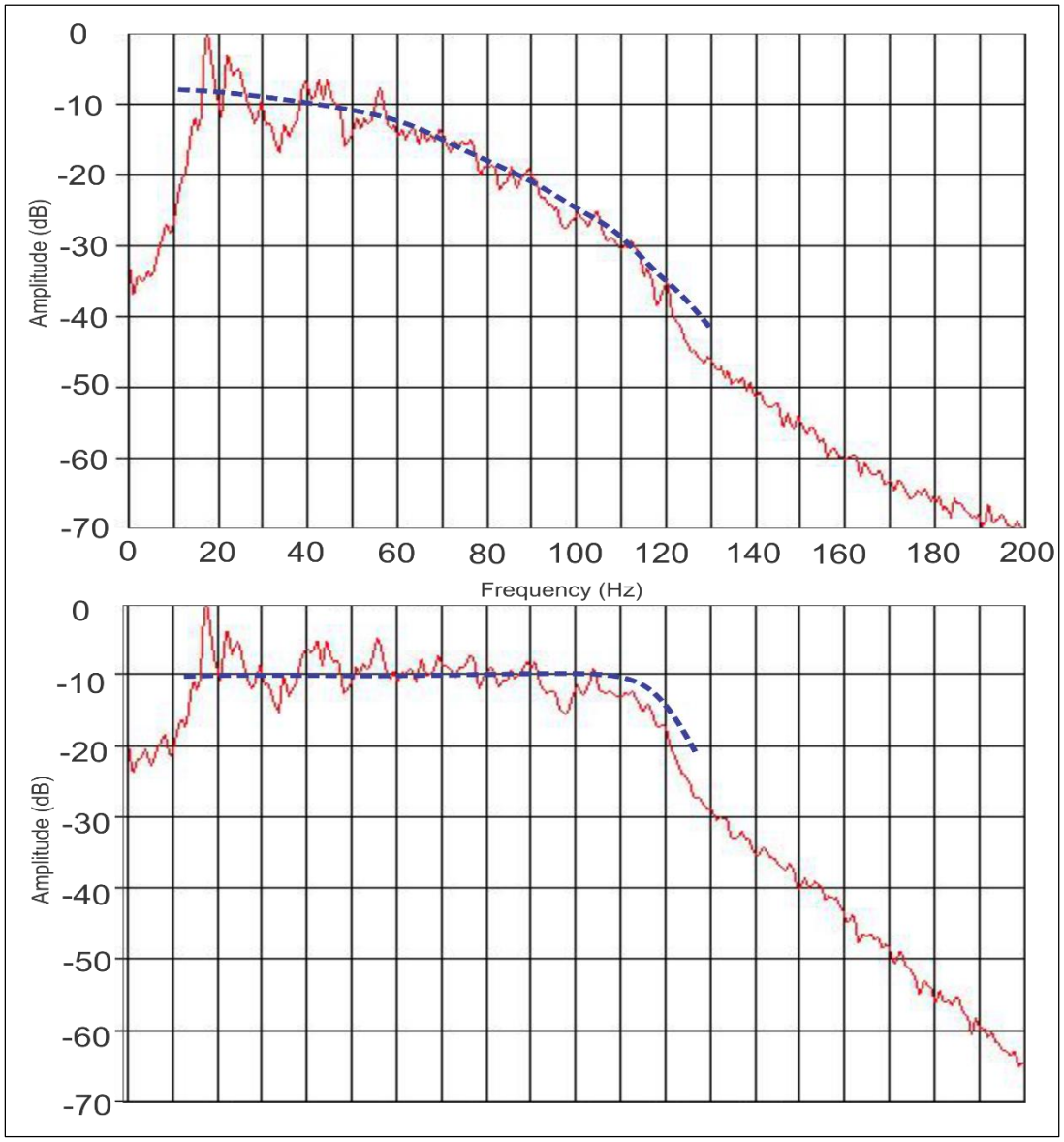

Figure 2.12. Average power spectrum of shot gather No.51 before and after time-variant spectral balancing. Above, before time-variant spectral balancing, the amplitude decreases with increasing frequencies. Below, after time-variant spectral balancing, the amplitude stays same high amplitude value with increasing frequencies. Blue dash-line represents the amplitude trend with increasing frequencies.

In addition to those noise suppression methods mentioned earlier, surface-consistent amplitude balancing, predictive deconvolution, ensemble equalization, F-K filtering, low frequency array filtering, and surface-consistent deconvolution techniques were also applied. However, as reasonable results could not be observed on shot gathers these techniques were not used in the final processing flow.

Comparison of raw and noise suppressed shot gathers of the 1st and 55th shots are shown in Figure 2.13 and Figure 2.14, respectively. Strong ground roll, air blast, and low frequency surface consistent noise in raw shot gather were suppressed by the methods mentioned above. These noise suppression methods increased the resolution and enhanced the possible reflections.

Root-mean-square (RMS) velocity function was determined through a detailed velocity analysis and used in Kirchhoff pre-stack time migration (Figure 2.15). Final Kirchhoff pre-stack time migrated and stacked sections are shown in Figure 2.16.

2.3.3 Seismic Interpretation

Final stack of the data shows a reflector having stacking velocities about 2000 m/s, which is reasonable to be a “salt reflector”. This reflection was observed at 290 ms that corresponds to about 290 m depth with 2000 m/s stacking velocity. Another reflector comparatively weaker than “salt reflector”, having around 1950 m/s velocity was observed at 210 ms that corresponds 205 m depth. That reflector was interpreted as “cap

rock reflector" (Figure 2.17). Reflector depths obtained from seismic data match the cap rock and salt depth information from previous studies in the area.

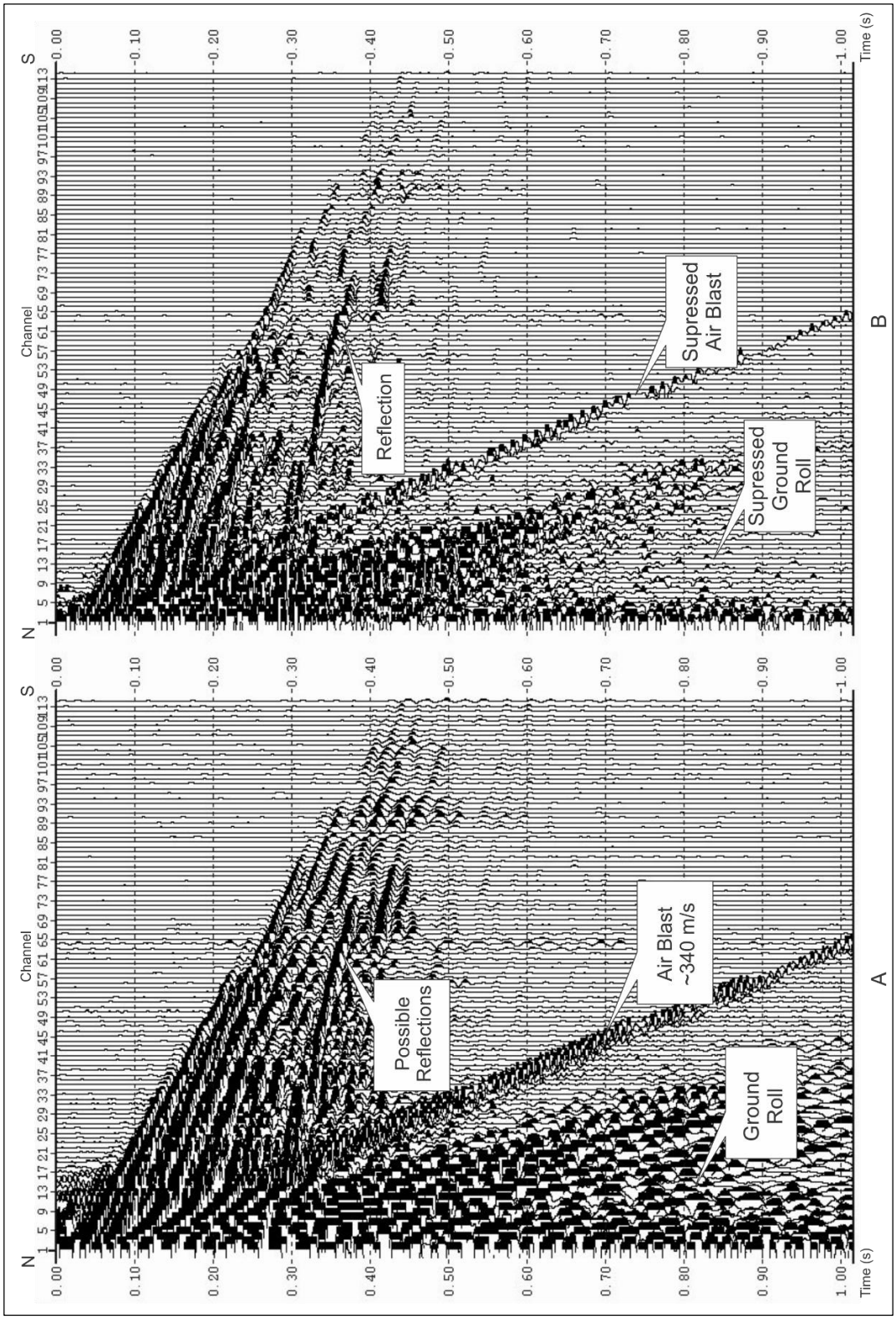

Figure 2.13. Comparison of raw (A) and processed (B) shot gathers of the 1st shot.

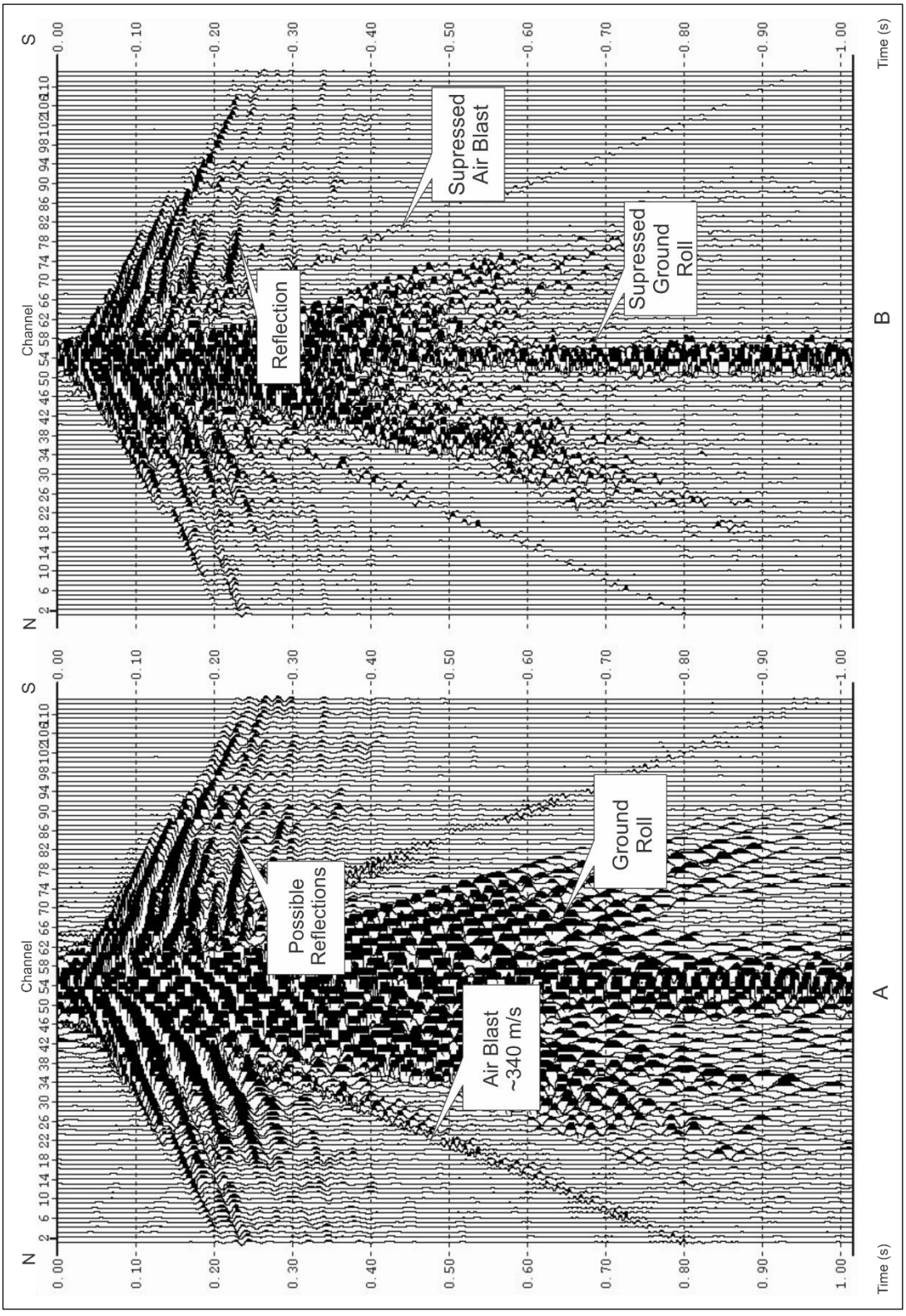

Figure 2.14. Comparison of raw (A) and processed (B) shot gathers of the 55st shot.

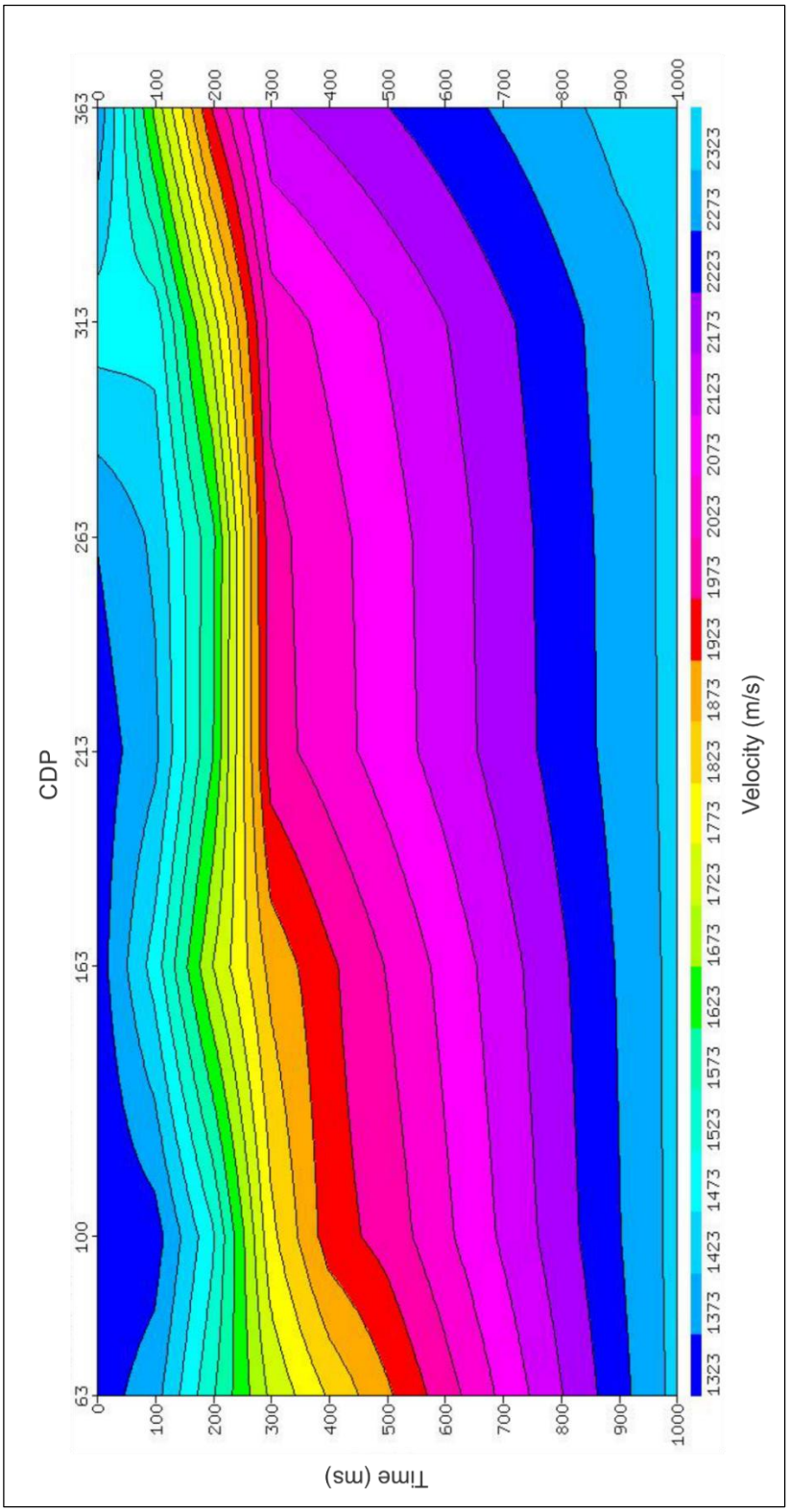

Figure 2.15. RMS velocity model used in pre-stack Kirchhoff time migration.

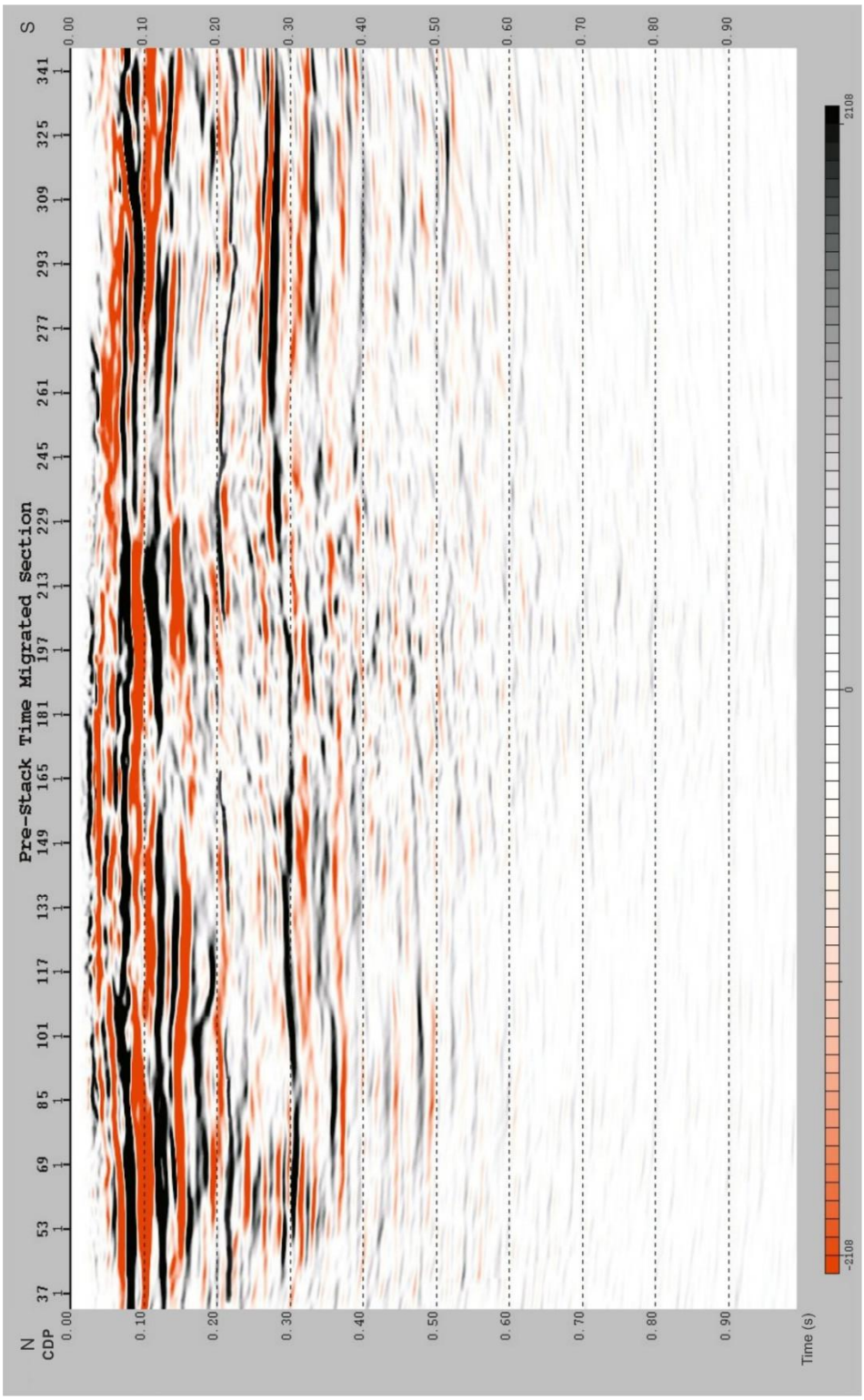

Figure 2.16. Final pre-stack Kirchhoff time migrated image. The color scale indicates the amplitude.

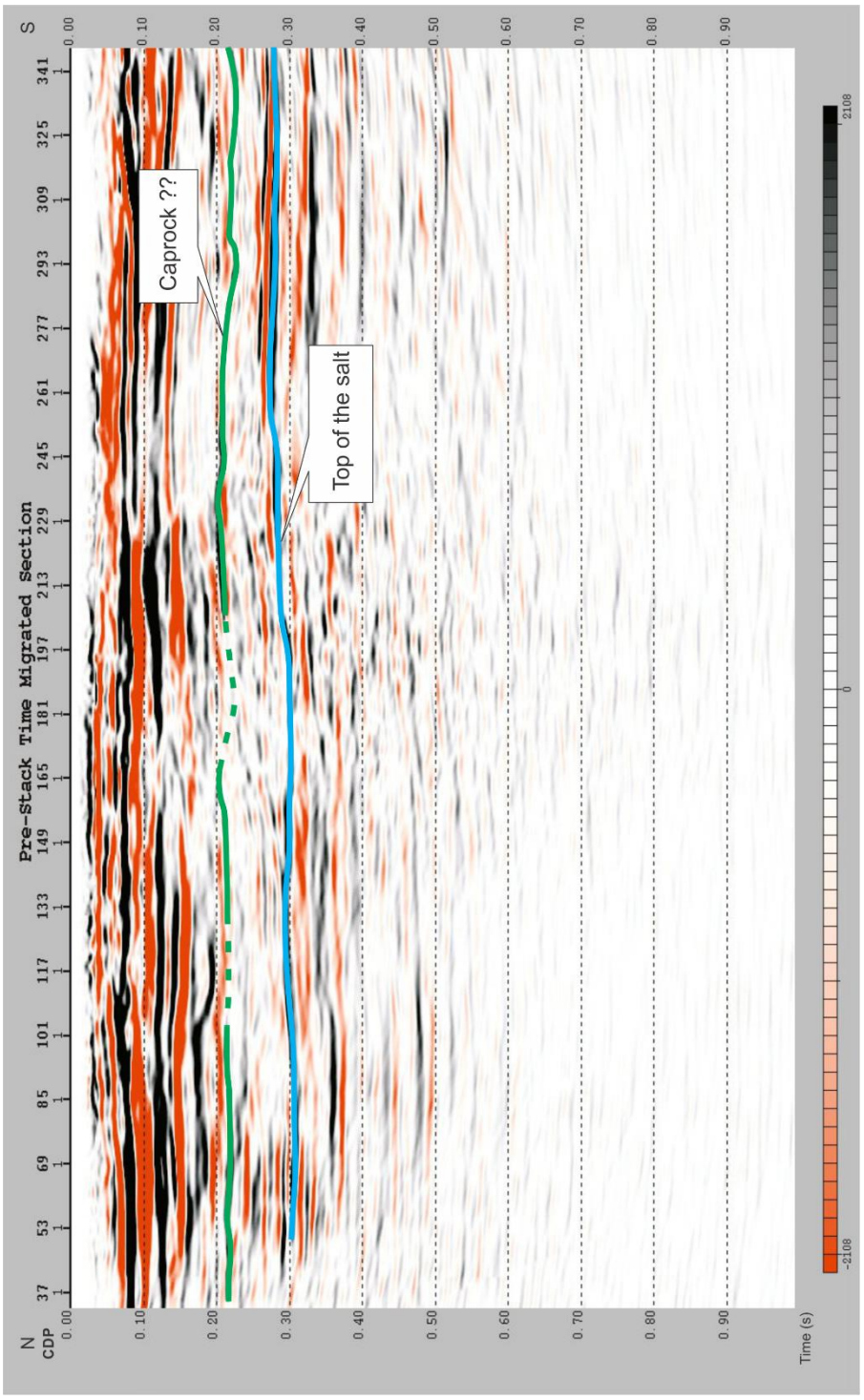

Figure 2.17. Interpreted pre-stack Kirchhoff time migrated image. The reflection, which is highlighted with blue line, is interpreted as top of the salt, and the horizon, which is highlighted with green line and dash line, is interpreted as cap rock. The color scale indicates the amplitude.

2.4 Gravity Modeling

Gravity method is an effective geophysical technique to reveal the subsurface structure. This method allows the area of interest to be modelled using the gravitational field variations caused by differences in the distribution of densities, and therefore distribution of rock types (Sheriff, 2002).

2.4.1 Gravity Data Acquisition

A 2-D gravity survey was carried out over the Pierce Junction salt dome in 2013 so as to gather more information about the study area. The objective of the survey was to model the gravity data and obtain a north-south cross-section of the salt dome, in addition to the east-west cross-section drawn by Glass (1953). However, due to permission issues and geographical limitations, the survey was carried out along the Almeda road. Hence, the data were collected along southwest-northeast trending (18^{o}) profile. The total length of the profile was 7600 m with 200 m station interval (Figure 2.18). AGL's Scintrex CG-5 Autograv gravimeter, Garmin GPS, distance measurement tools, and safety equipment were used during the data acquisition. The graph of the raw gravity data is shown in Figure 2.19.

Figure 2.18. Location of the gravity survey. Blue polygon represents the estimated top of the salt boundary (Huang, 2012).

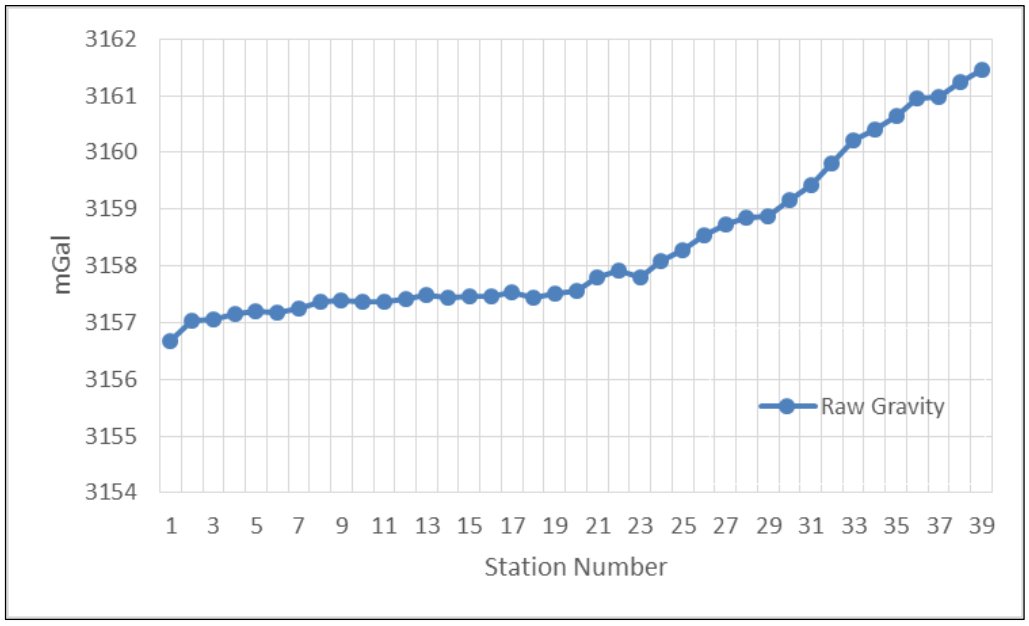

Figure 2.19. The graph of the raw gravity data of SW-NE line.

2.4.2 Gravity Data Processing

Density differences in the subsurface lithology causes small gravity variations. These small anomalies can be observed after removing the temporal and spatial effects from the data (Seigel, 1995 Boyd, 2003; Otoum, 2011). Drift and tide corrections were applied to eliminate the time varying effects caused by instrumental drift and tidal effects. Spatial corrections consist of latitude, free-air, Bouguer, and terrain corrections. Elliptical shape and rotation of the Earth cause variations in the gravity field based on the location of the measurement (Nettleton, 1976). In order to avoid this effect latitude correction is made employing the Moritz (1992) equation (Eq. 2.1).

$$\boldsymbol{G_n = 9780327\left(1.0 + 0.0053024\, sin^2(\theta) - 0.0000058\, sin^2(2\theta)\right)}$$

(Eq. 2.1)

where**;**

G_n = gravity normal in mGal after latitude correction,

Θ = latitude of the measurement location in decimal degrees.

Gravity measurements are also affected by the elevation of the measurement location (Nettleton, 1976). As the data were collected at different distances from the center of the Earth than that of the datum, free-air correction is required, (Sheriff, 2002). Free-air correction is defined by the following equations (Eq. 2.2 and 2.3).

$$\boldsymbol{G_f = G_o - G_n + \Delta G_f} \quad \text{(Eq. 2.2)}$$

$$\boldsymbol{\Delta G_f = \pm 0.3086 h} \quad \text{(Eq. 2.3)}$$

where;

G_f = free-air corrected gravity reading in mGal,

G_o = raw observed measurement in mGal,

ΔG_f = free-air correction in mGal,

h = elevation in meters.

If the location of the measurement is above the sea level free-air correction will be positive; otherwise, free-air correction will be negative.

Attraction of the rock between the station and the elevation of the datum causes another effect on the gravity data. Bouguer correction is applied to eliminate that kind of effect by using the density of the intervening rock and the elevation (Sheriff, 2011). The Bouguer correction is defined by the following equation (Eq. 2.4).

$$\boldsymbol{G_B = 0.04192 \rho h} \quad \text{(Eq. 2.4)}$$

where;

G_B = Bouguer correction in mGal;

ρ = bulk density of the overburden in grams per cubic centimeter,

h = elevation in meters.

The equations for latitude, free-air, and Bouguer corrections were implemented using Microsoft Excel and calculated for known parameters. Subsequently, results obtained from free-air and Bouguer corrections were used as inputs for the modelling step. The elevation values of the gravity stations used in free-air and Bouguer corrections were extracted from GPS data. For each station elevation was measured at least three times and the average of these measurements was used as the input parameter.

2.4.3 Forward Modeling and Interpretation

Bouguer anomaly data were modelled using GEOSOFT Oasis Montaj software. Typical gravity anomalies of salt domes vary due to depth of the structures. A shallow salt dome of Gulf Coast should produce gravity difference between 0-2 mGal (Prieto, 2000). As expected, the Pierce Junction salt dome produces about 1 mGal difference with its surrounding material. In general, anomaly would be increased in amplitude and sharpness (frequency). But it is also possible to observe smaller anomalies due to positive anomaly superimposition that is caused by the faulting activity around the salt and cap rock.

The typical US Gulf Coast sediment densities were used in the modelling stage (Prieto, 2000) (Table 2.1). The data were modelled for 4000 m depth which is about half-length of the data profile. On the other hand, depths of the surrounding sediments, top of the salt, and the overlying cap rock which are denoted by well logs around the salt dome on east-west cross-section were used as control points for modelling.

Table 2.1. Layers and densities that are used in gravity modeling.

Layer	Density (g/cm^3)
Salt	2.20
Caprock	2.60
Miocene	2.25
Frio	2.35
Vicksburg	2.43
Yegua	2.50

The gravity profile is located in the western part of the salt dome. The expected diameter of the top of the salt is about 1.2 km but as the profile does not cross over the center of the salt dome, it is modelled as 800 m. Also, the thickness of the cap rock varies and becomes thinner on the sides of the salt dome (Figure 2.20). Besides the anomaly that is interpreted as salt dome, there are two gravity variations on the north and south ends of the profile. Those variations can be caused by faulting activity, dramatic changes in sedimentary thickness, salt dome rooting, and tilting in N-S direction etc.

As a result, modelled gravity data shows that the extension of the salt dome in N-S direction is in the expected boundary. However, this gravity profile is not enough to interpret the shape and size of the salt dome.

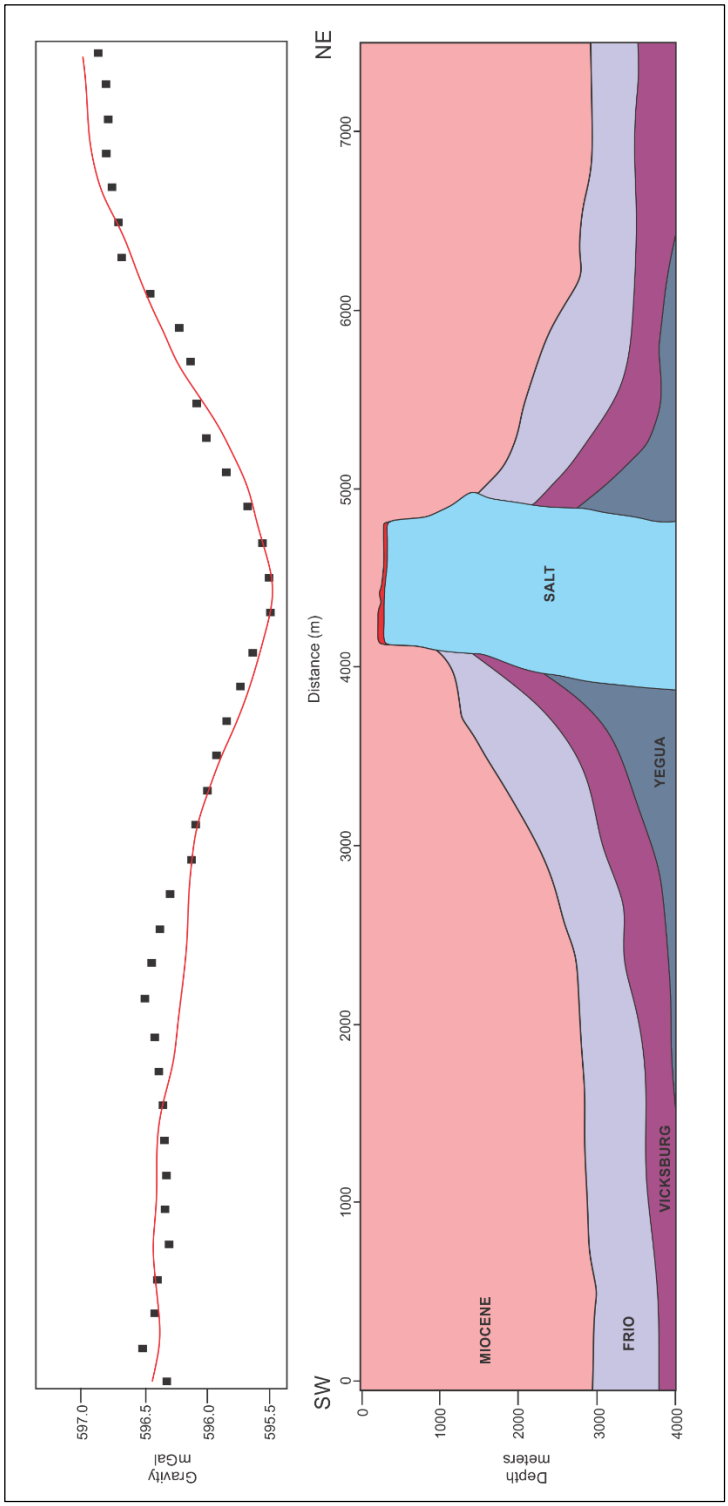

Figure 2.20. Gravity model of SW-NE profile. Black dots and red line represent the observed and calculated gravity, respectively. Vertical exaggeration of model is 0.5.

CHAPTER THREE: ACQUISITION MODELING FOR THE PIERCE JUNCTION SALT DOME

3.1 Velocity Models

Two-D and 3-D velocity models were built using GEDCO (Geophysical Exploration and Development Co.) OMNI 3D Survey Design software.

First, 2-D velocity model of east-west cross-section of the salt dome was created. Extent of the model was set to 16 km in order to provide sufficient space in survey design analyses. Geological cross-sections from well logs, other examples, 2-D seismic data, and gravity data were used to obtain the 2-D velocity model. According to previous studies, the Pierce Junction area consists of four main sedimentary layers along with the salt dome and overlying cap rock (Glass, 1953). These sedimentary layer are Miocene, Frio, Vicksburg, and Yegua (Figure 2.3).

Average P-wave interval velocities of Vicksburg, Frio, and Yegua layers were adapted from previous studies of Ewing et al. (1983), Parra and Collier (1997), and Bain (2010). The interval velocity of the cap rock layer and the shallowest part of the near surface layer were calculated as 2200 m/s and 1800 m/s using RMS velocities of the original 2-D seismic data. Also, velocities within the Miocene layer were separated into six constant velocity sub-layers to create a velocity gradient within the layer. Interval velocity gradient within the Miocene layer were adapted from Lash (1980) that shows P-wave velocity gradient within the Miocene layer in Gulf Coast sediments (Figure 3.1). The P-wave velocity of the salt was assigned as 4500 m/s which is the average velocity used in many seismic

modeling studies (Jiao et al, 2012; Oezsen, 2004; Willis et al., 2006). Final 2-D interval velocity and RMS velocity models are shown in Figure 3.2 and 3.3, respectively.

S-wave velocities were calculated using V_p/V_s= 2.37 which is a common ratio for the Gulf Coast sediments as recommended by Castagna et al. (1985). Properties of each layer within the model are given in Table 3.1.

Table 3.1. Properties of layers in 2-D model.

Layer	P-wave Interval Velocity (V_p) m/s	S-wave Interval Velocity (V_s) m/s	V_p/V_s
Miocene	1800 - 2500	600-1000	3.0-2.5
Frio	3000	1265.8	2.37
Vicksburg	3300	1319	2.37
Yegua	3600	1519	2.37
Salt	4500	2.250	2
Caprock	2200	1100	2

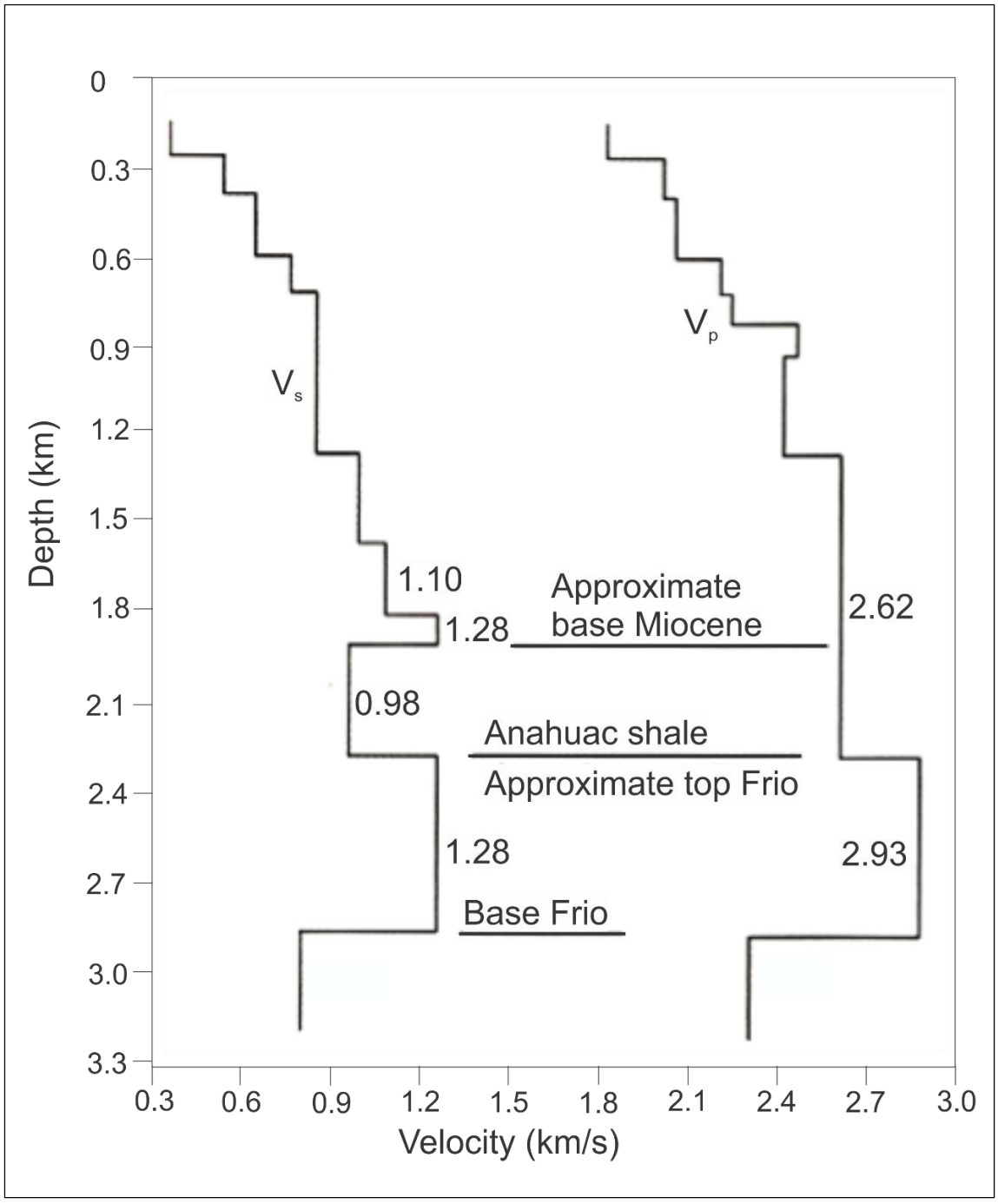

Figure 3.1. P-wave and S-wave velocities within the Miocene layer for Gulf Coast sediments (modified after Lash, 1980).

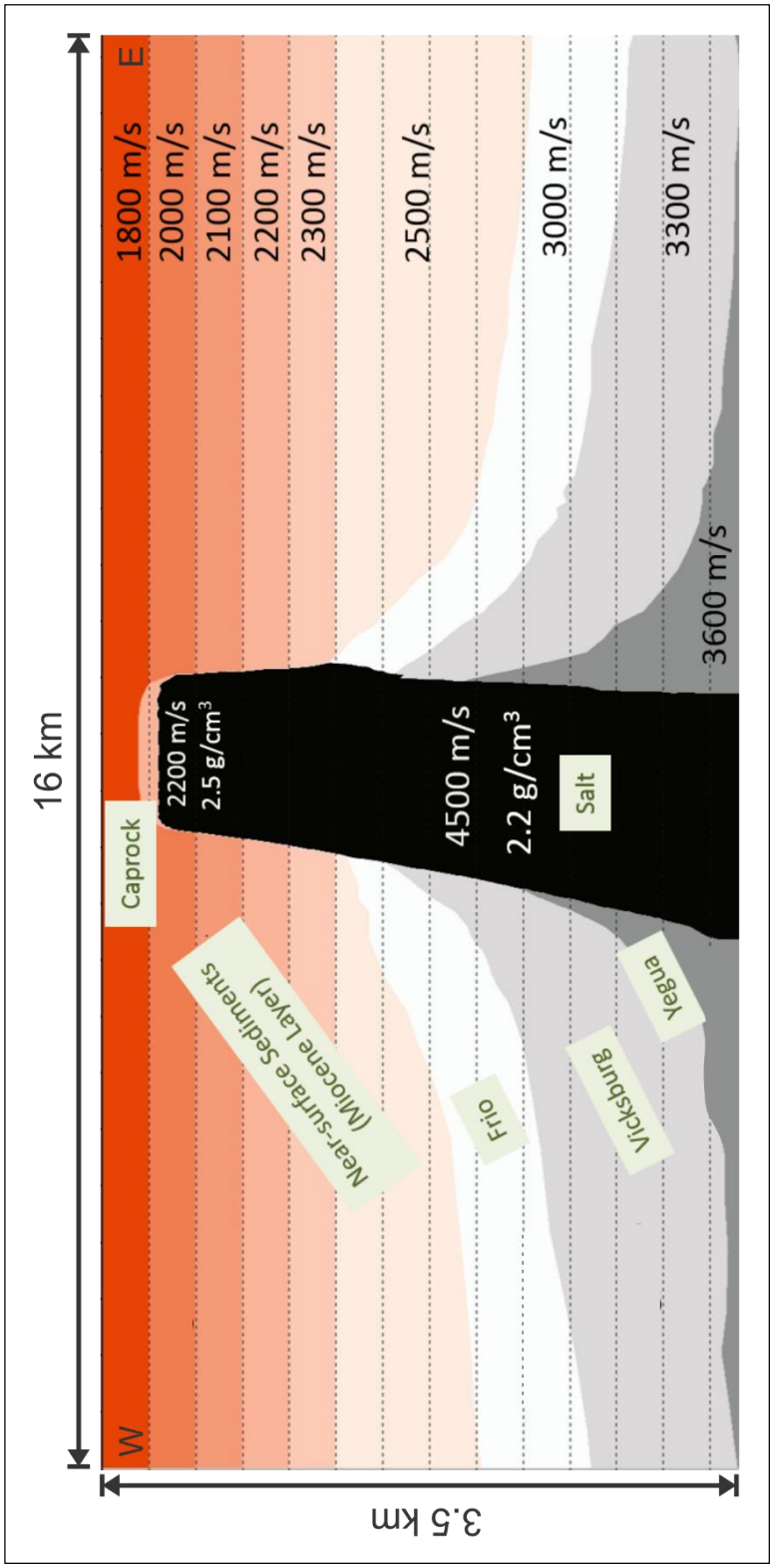

Figure 3.2. Final 2-D interval velocity model of Pierce Junction Salt Dome.

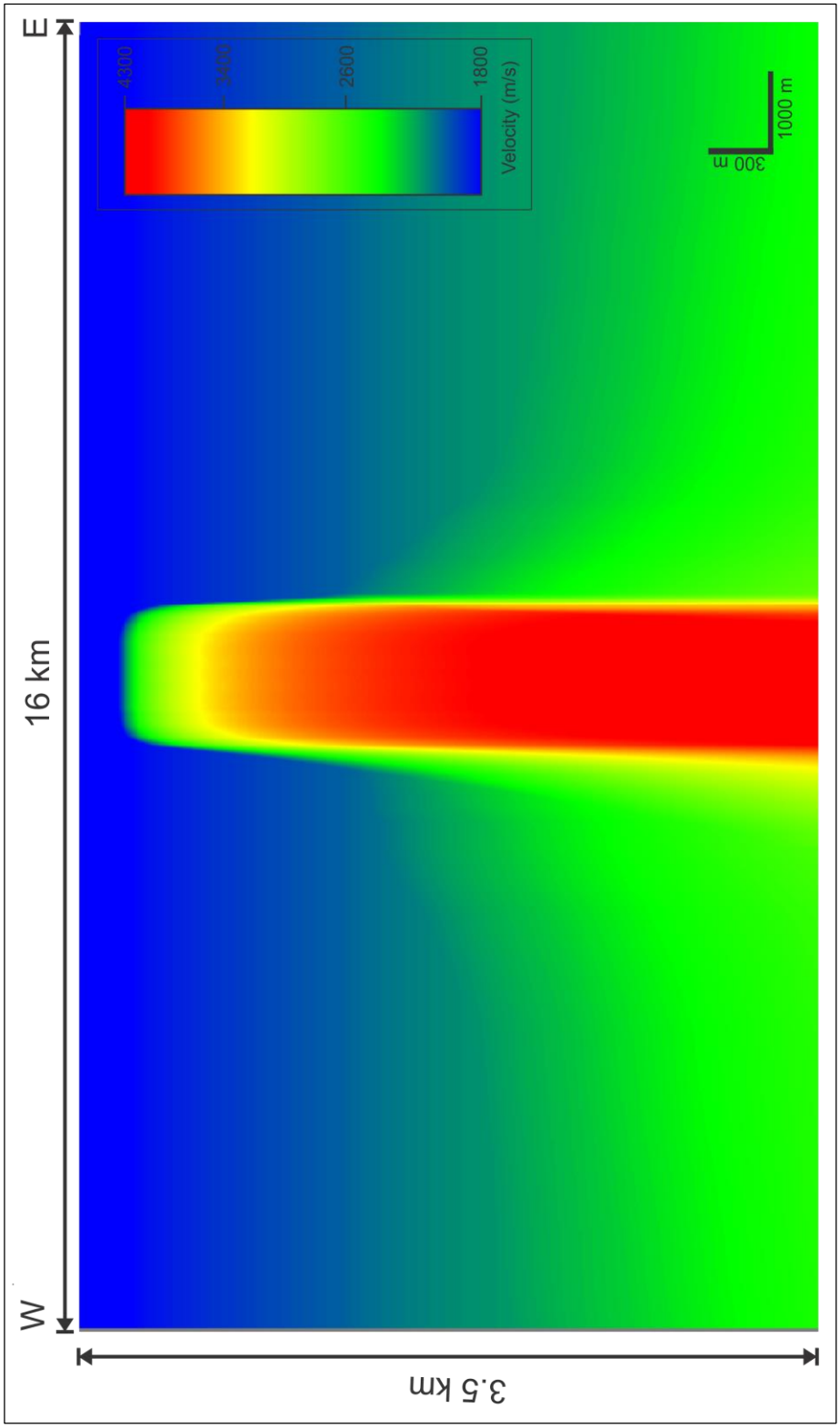

Figure 3.3. Final 2-D RMS velocity model of Pierce Junction Salt Dome.

Every set of geological and geophysical data from the study area contributed valuable information for building an accurate 3-D velocity model. In this study, a circular piercement salt dome shape was built using the dimensions of the dome in east-west cross-section. Coordinate transformation was applied to the eastern half of the 2-D model, 360° rotated from the center with 1° interval, to obtain 3-D horizons of sedimentary layers (Figure 3.4). On the other hand, unlike the horizontal Miocene layers in 2-D velocity model, the Miocene layer was separated into three layers which are dipping with different angles (5°, 10°, and 15°) so as to understand the effect of the dipping layers with different angles to the acquisition and imaging. Consequently, a volume with dimensions of 16x16x3.5 km that represents the salt dome and surrounding area was created for 3-D survey design analyses and modeling purposes. In-line/cross-line representation and the 3-D chair diagram of the model imaged by Paradigm 3-D Canvas software are shown in Figure 3.5 and 3.6, respectively.

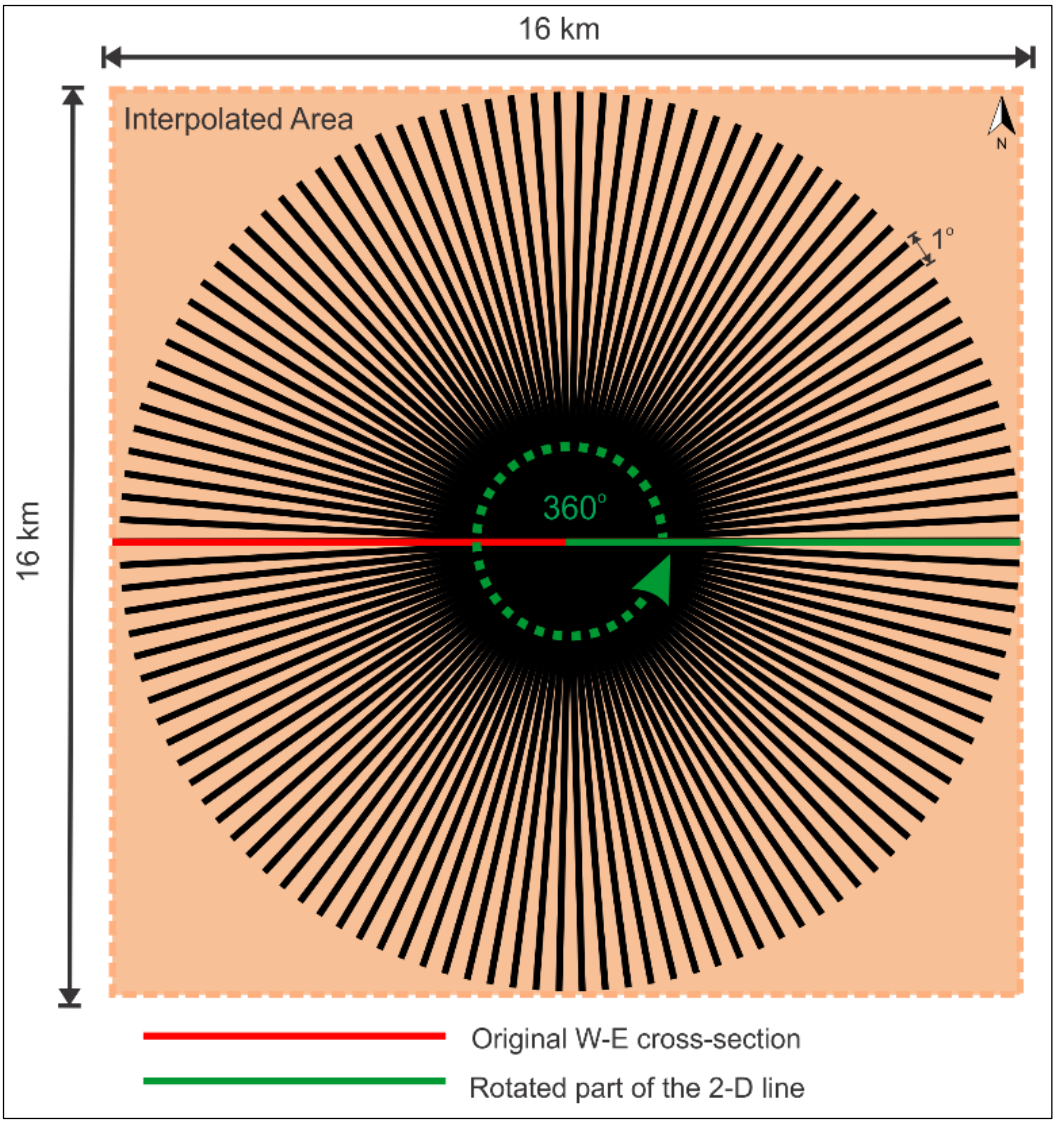

Figure 3.4. The method that used to obtain 3-D horizons by rotating the original 2-D W-E Cross-section

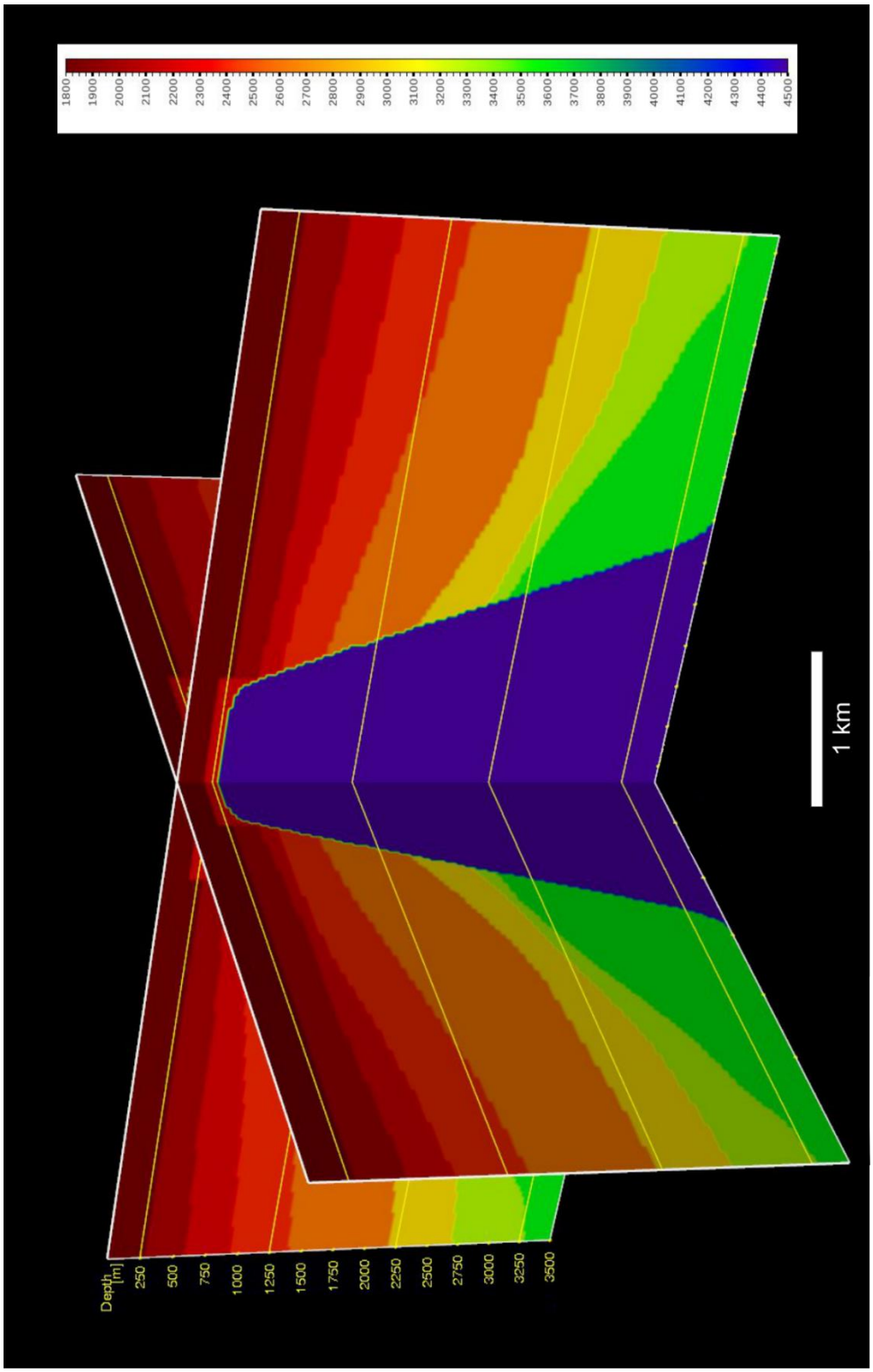

Figure 3.5. In-line / Cross-line representation of 3-D velocity model of Pierce Junction Salt Dome area.

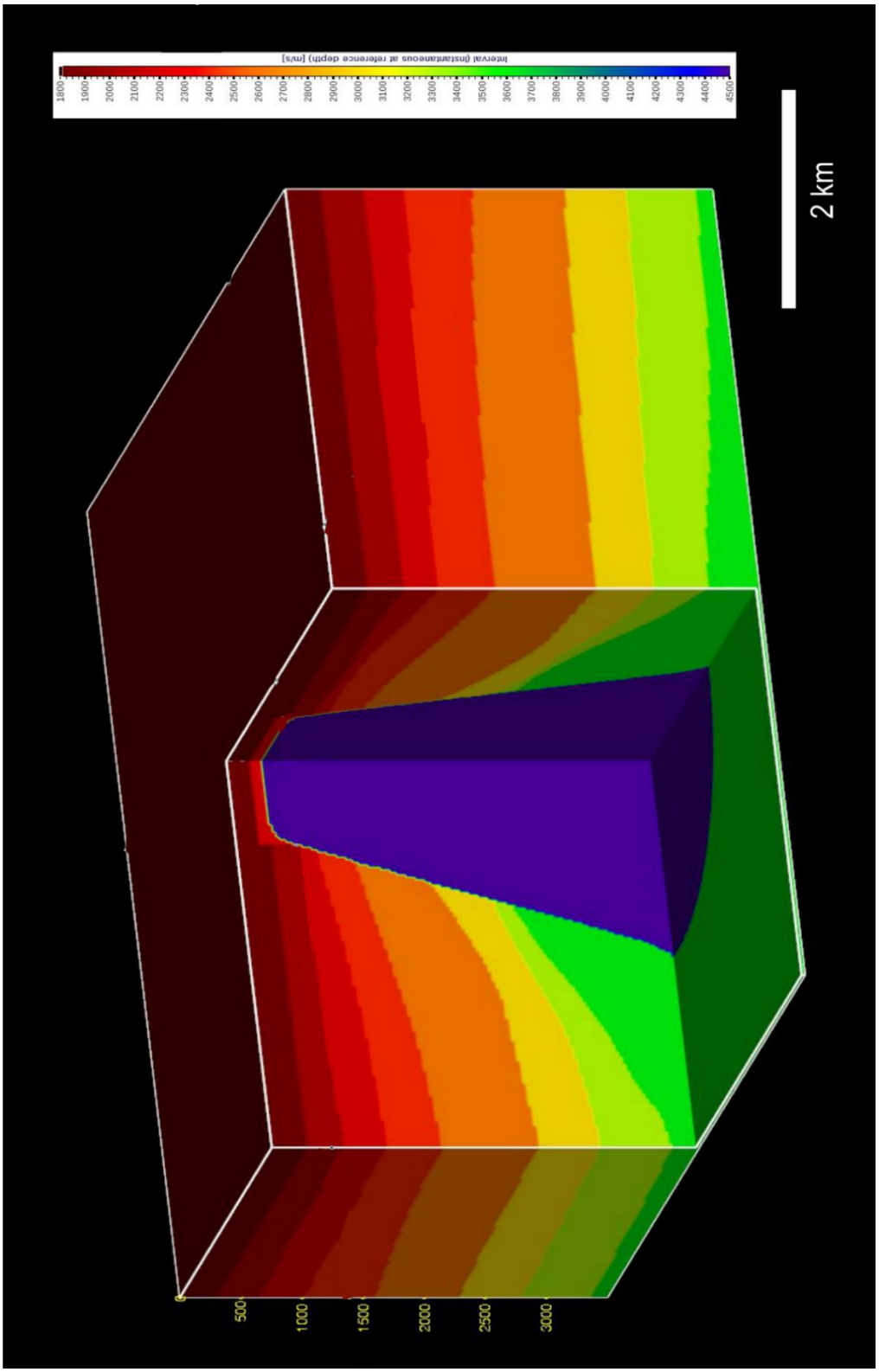

Figure 3.6. Chair diagram of 3-D velocity model of Pierce Junction Salt Dome area.

3.2 2-D Seismic Survey Design via Modeling and RTM Imaging

3.2.1 Fundamentals of 2-D Seismic Survey Design

Over the last century, 2-D seismic data acquisition has been one of the most effective geophysical methods that allows us to delineate the subsurface geology. Two-D seismic survey has kept its popularity through years even though it is being replaced with three-dimensional (3-D) seismic survey. Two-D surveys have been commonly implemented as a cost effective method to provide information for 3-D survey design projects. The most important criterion in 2-D seismic survey design is optimizing the cost and time while imaging the targets as detailed as possible.

3.2.1.1 Description of Important Elements of Subsurface

Definition of the horizons in the survey area provides important information for determining the survey parameters, such as offset range, source frequency, sample rate, subsurface coverage, and resolution.

Horizon definition can be given by four important layers: (1) near-surface layer, (2) shallow horizon, (3) target layer, and (4) deep horizon (Stone, 1994) (Figure3.7). Existing well logs, seismic data, and check shot information can be used to approximate velocity and maximum dip determination. Each layer has different importance while considering the survey parameters. Modeling of those layers using depth, average velocity, and time information usually assure that the designed survey will meet the imaging requirements.

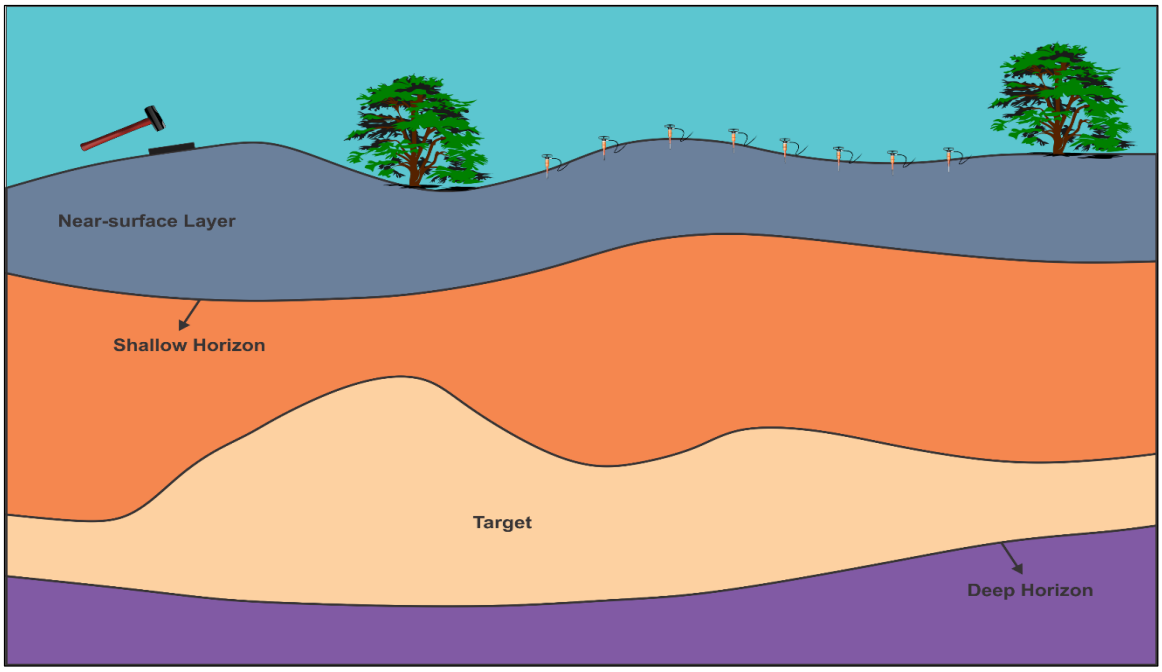

Figure 3.7. Key horizons for defining the survey parameters: surface, shallow, target, and deep horizons (modified after Stone, 1994).

3.2.1.1.1 Near-surface layer

Ground roll determination and offset calculation are made using near-surface layer velocities. Weathered layers mostly affected by erosion and exposure show very low velocity. Small portion of the seismic data can be tested by comparing ground roll modeling. Also, static time shifts can be controlled with a reflection survey in the areas where the weathered layer is thick and variable (Stone, 1994).

3.2.1.1.2 Shallow layer

The velocity information of the layers shallower than the target layer is usually required for processing and interpretation purposes. Imaging the shallower horizons is possible if

the near offset, distance to the nearest receiver from the source, is less than the depth of the shallow horizon (Figure 3.2). Depth of the horizon can be calculated by the following basic time-distance equation (Eq. 3.1).

$$\boldsymbol{Z_{sh} = 0.5 \times t \times V_{sh}} \quad \text{(Eq. 3.1)}$$

where;

t = two-way travel time to the shallow horizon,

V_{sh} = average-velocity to the layer,

Z_{sh} = depth to the shallow layer.

Nearest usable offset can be determined by noise tests in field. The goal of these noise tests is keeping the near offset as small as noise conditions allow for imaging the shallower depths. Near offset parameter is determined by the following inequality (Eq. 3.2).

$$\boldsymbol{H_{near} < Z_{sh}} \quad \text{(Eq. 3.2)}$$

3.2.1.1.3 Target layer

The requirements of the survey design are determined according to the main layer of interest. If the information about shallower layer is redundant, same near offset calculations can be used for target layer. Additionally, expected thickness and reflectivity information of the layer should be used to estimate the frequency range required to image the target. In theory, quarter wavelength of the source signal should be equal to

the thickness of the target layer in order to image the top and the bottom of the layer (Liner, 2004). For real cases, however, possible maximum frequency is used to obtain the best image.

3.2.1.1.4 Deep Horizon

The deepest horizon desired to be imaged should be considered while deciding the survey parameters. In most cases, the seismic survey is not only designed to image the target layer, but it is also designed to image deeper layers that will be used in interpretation, just as shallow layers. Record length, source power, instrumental filters, and the maximum offset are considered by taking the depth of the deep horizon into account.

The rule of thumb is that the maximum offset should be at least equal to the deepest target. The spread size can be a little greater for dipping layers. The rule for the maximum offset is given by Eq. 3.3.

$$\boldsymbol{H_{max} \geq Z_{deep}} \qquad \text{(Eq. 3.3)}$$

3.2.1.2. Group Interval (Spatial Sampling)

The group interval can be described as the horizontal distance between the centers of adjacent geophone groups (Sheriff, 2002) (Figure 3.8). Aliasing is the most important factor that determines the maximum group interval. Spatial aliasing can be seen in seismic data when the group spacing is coarse. In contrast to adequately selected group intervals, individual points do not merge into a continuous event. Hence, spatial aliasing decreases

the quality of the seismic image (Liner, 2004). Group interval can be smaller depending on the survey budget but it should not exceed the spatial aliasing limit. Maximum group interval condition is given by the following equation (Eq. 3.4).

$$\mathbf{G_m} < \frac{\mathbf{V_{int}}}{\mathbf{2 \times f_{max} \times \sin \theta}} \quad \text{(Eq. 3.4)}$$

where;

G_m = maximum group interval,

V_{int} = interval velocity,

f_{max} = maximum frequency expected,

θ = maximum dip of the target horizon on degrees.

The Fresnel zone is another factor that can limit the maximum group interval. A Fresnel zone is the portion of a reflector making an actual image of the individual events (Sheriff, 2002; Stone, 1994). Maximum group interval determined the Fresnel zone is defined by Eq. 3.5.

$$\boldsymbol{G_f} < \frac{\boldsymbol{V_{rms} \times (t_z)^{\frac{1}{2}}}}{\mathbf{4 \times (f_{max})^{\frac{1}{2}} \times sin\, \theta}} \quad \text{(Eq. 3.5)}$$

where;

t_z = two-way record time of the target horizon,

V_{rms}: RMS velocity,

f_{max}: maximum frequency expected,

θ: maximum dip of the target horizon in degrees.

The purpose of both aliasing and Fresnel zone formulas is to make the group interval as large as possible to decrease the survey cost while meeting the resolution expectations.

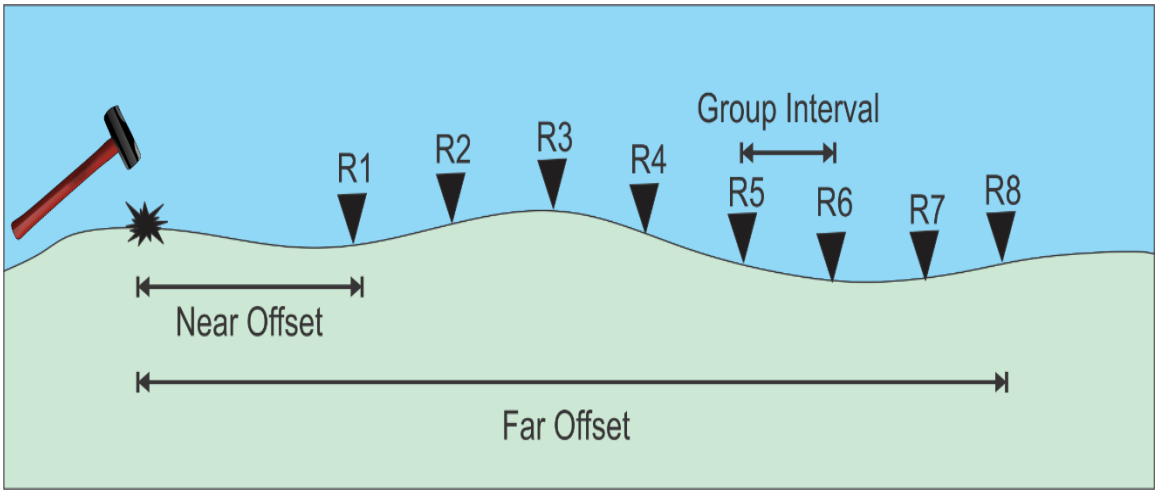

Figure 3.8 Representation of near offset, far offset, and group interval.

3.2.1.3 Time Sample Rate

The wave field initiated by the shot and recorded by the receiver should be digitally sampled in time and space domain adequately. The maximum sampling frequency is determined by the Nyquist frequency. Frequencies above the Nyquist frequency threshold are aliased and reconstructed wave field will be recorded with low frequencies which do not represent the original data. This effect is called temporal aliasing or simply aliasing (Liner, 2004). Nyquist frequency (f_{nyq}) is defined by Eq. 3.6.

$$f_{nyq} = \frac{1}{2\,dt} \qquad \text{(Eq. 3.6)}$$

Where; dt is the sample rate.

One half of the Nyquist frequency is the limit for the highest actual frequency, f_{max}, for reconstruction of a uniform wave field of the original signal. This rule provides the condition expressed in Eq. 3.7 for dt.

$$\boldsymbol{dt \leq \frac{1}{2}\left[\frac{1}{2f_{max}}\right] = \frac{1}{4f_{max}}} \qquad \text{(Eq. 3.7)}$$

In most of seismic surveys, the time sample rate is selected as 1 ms since the sampling rate does not affect to acquisition cost. On the other hand, processing cost and data size are inversely proportional to sampling rate.

3.2.1.4 Recording Time

Recording time (listen time) of the survey should be calculated appropriately to reach survey objectives and/or adjust the survey cost. A rule for maximum recording time, t_{max}, is defined by Eq. 3.8 (Liner, 2004).

$$\boldsymbol{t_{max} \geq \frac{1.4}{V_{avg}}\sqrt{x_{max}^2 + 4z_{max}^2}} \qquad \text{(Eq. 3.8)}$$

where;

V_{avg} = average velocity from the acquisition surface to the deepest reflector,

x_{max} = maximum offset,

z_{max} = depth of the deepest horizon.

Employing this equation ensures the listen time to be long enough to record both reflections and diffractions coming from the deepest horizon. As represented in the equation, maximum recording time is calculated 40% longer to provide plentiful time for diffractions and possible dipping reflections (Liner, 2004).

In the case of steep dips or turning waves are expected, the recording time should be chosen longer than the calculated maximum recording time. Even though extra time will increase the survey cost, it is better to make sure that all possible seismic data are collected.

3.2.1.5 Signal-to-noise Improvement, Vertical stack, and Fold Coverage

Any kind of event or vibration except primary reflections and diffractions are considered as noise in the seismic data. The classification of the noise types encountered in seismic data is shown in Figure 3.9.

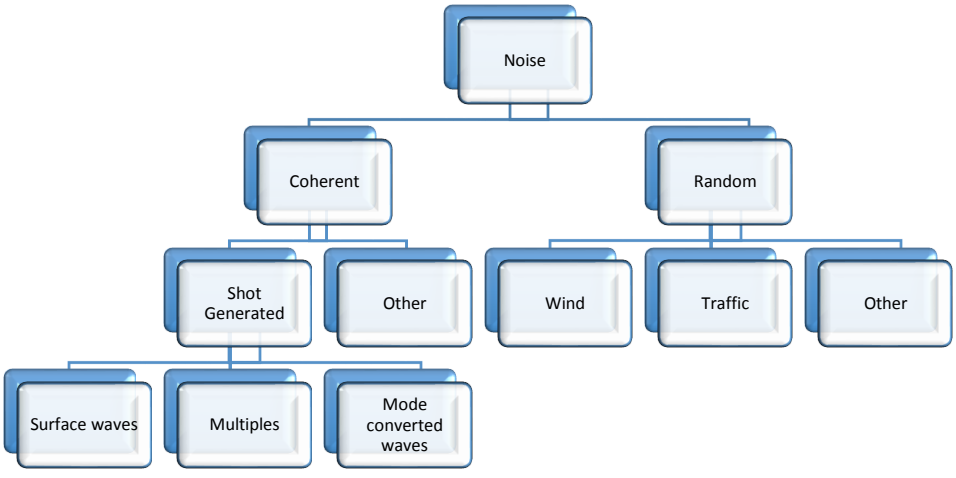

Figure 3.9. The classification of the noise types encountered in seismic data (modified after Liner, 2004).

Signal-to-noise ratio is the term that is used to explain the signal strength relative to noise strength. Unless the noise is used for specific analysis, higher signal-to-noise ratio is always desired in seismic data. However, in practice, it is difficult to determine and isolate the signal from the noise (Liner, 2004; Sheriff, 2002).

Vertical stacking and common-midpoint (CMP) stacking are the two main methods that can be applied in acquisition to increase the signal-to-noise ratio. Vertical stacking is a signal-to-noise enhancement method that combines the subsequent shot profiles generated at the same shot location. Number of vertical stack directly affects the acquisition time. Therefore, number of vertical stack is one of the fundamental factors that determines the survey duration. Industry standard states that fold of vertical stack should be between one and eight (Stone, 1994).

Furthermore, common midpoint stacking can be considered as both a recording and a processing method. Traces assumed to be coming from a certain position on the Earth's surface are stacked to generate a single trace at that position to increase the signal-to-noise ratio. The number of those traces, which are added to give a single trace in a certain position, is called stacking fold or fold-of-coverage (Liner, 2004; Sheriff, 2002; Cordsen et al., 2000). Number of recording channels, groups, and shot intervals are the main factors that determine the CMP fold. The fold for a 2D line is defined by the following equation (Eq. 3.9).

$$F_{2D} = \frac{N_c \times dx_g}{2 \times dx_s} \quad \text{(Eq. 3.9)}$$

where;

F_{2D} = fold for a 2D line,

N_c = number of recording channels,

dx_g = group interval,

dx_s = shot interval.

The effect of those stacking procedures can be defined with signal-to-noise improvement factor, I_{sn} (Eq. 3.10).

$$I_{sn} = \sqrt{F_v \times F_{cmp} \times N_g} \quad \text{(Eq. 3.10)}$$

where;

$F_{v:}$ = fold of vertical stack,

F_{cmp} = fold of CMP stack,

$N_{g:}$ number of geophones per group.

The final signal-to-noise ratio can be calculated employing the following equation (Eq. 3.11).

$$R_{snf} = R_{snr} \times I_{sn} \quad \text{(Eq. 3.11)}$$

where;

R_{snf} = final signal-to-noise ratio,

R_{snr} = raw signal-to-noise ratio,

I_{sn} = signal-to-noise improvement factor.

3.2.2 Analyses of the Actual 2-D Survey

In this part of study, the 2-D seismic survey carried out within the salt boundary was analyzed in terms of fold, illumination, resolution, and offset distribution on 2-D velocity model. Parameters of the survey is given by Table 3.2.

Table 3.2 Acquisition parameters of actual 2-D seismic survey.

Number of Receiver Stations	193	**Number of Shots**	192
Number of Receivers	120	**Receiver Interval**	5 m
Shot Interval	5 m	**Shot line length**	945 m
Receiver line length	955 m	**Sampling rate**	1 ms
Recording length	4 s		

The maximum fold of the survey is 120; however, the fold values are not uniformly distributed along the survey line, since receiver line was rolled once from the 73rd station unlike the conventional 2-D seismic acquisition (Figure 3.10). Trace count - offset histogram of the survey is shown in Figure 3.11.

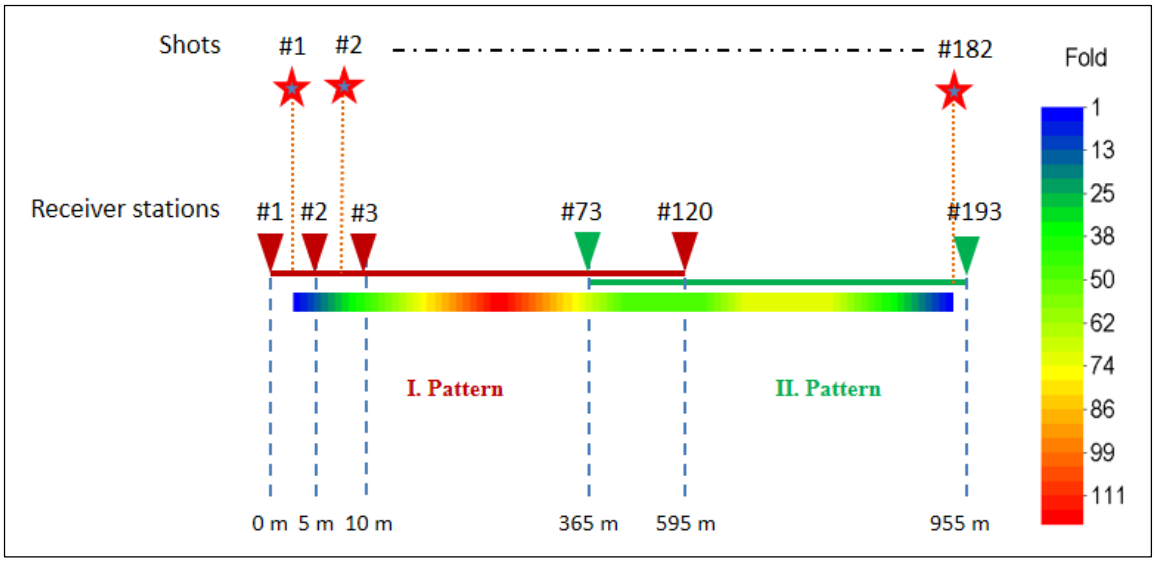

Figure 3.10 Survey geometry and fold distribution of the actual 2-D survey.

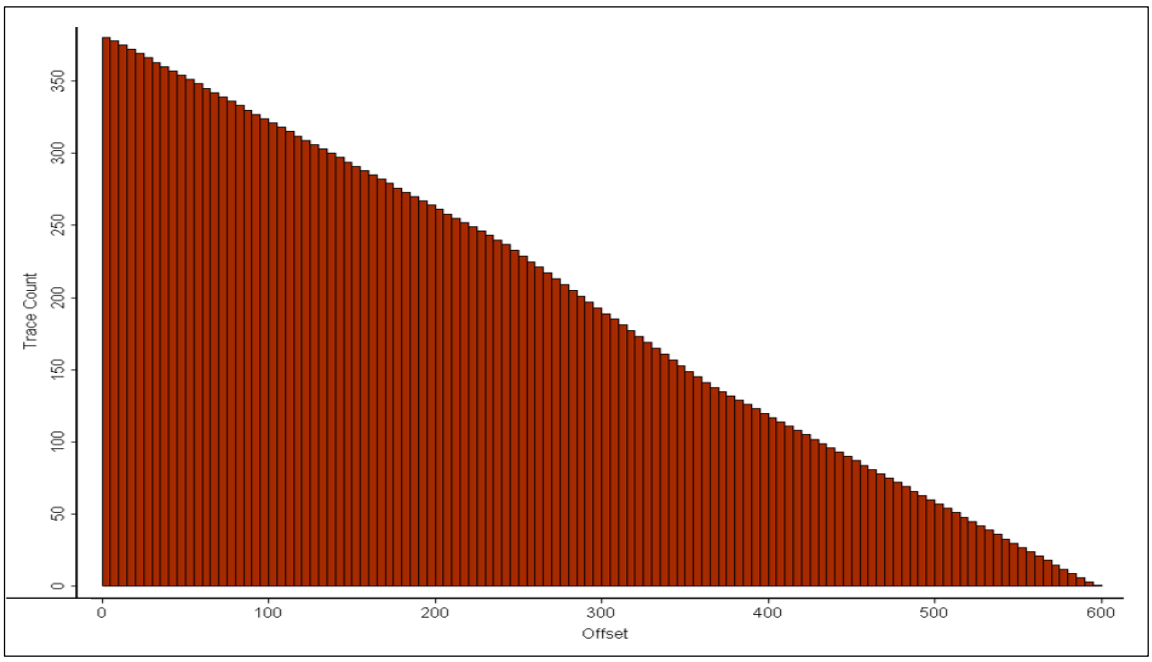

Figure 3.11 Trace count – Offset histogram of actual 2-D seismic survey. The chart shows the number of traces that fall each range of offset values.

Source frequency and group interval parameters were used in the survey to determine the vertical and horizontal resolutions. Possible vertical and horizontal resolutions of the

seismic image before and after migration are depicted in Figure 3.12 and Figure 3.13, respectively. Note that 120 Hz maximum frequency and 2.5 m CDP interval were used to determine these resolutions.

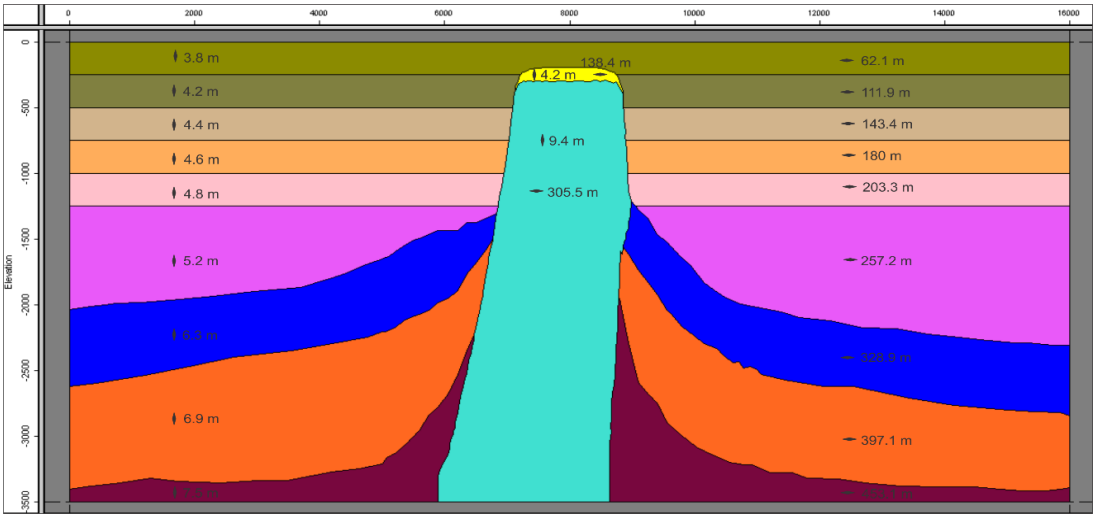

Figure 3.12 Vertical and lateral resolutions of actual 2-D seismic survey in certain depths before migration. Vertical and horizontal diamond shapes represent the vertical and lateral resolution, respectively.

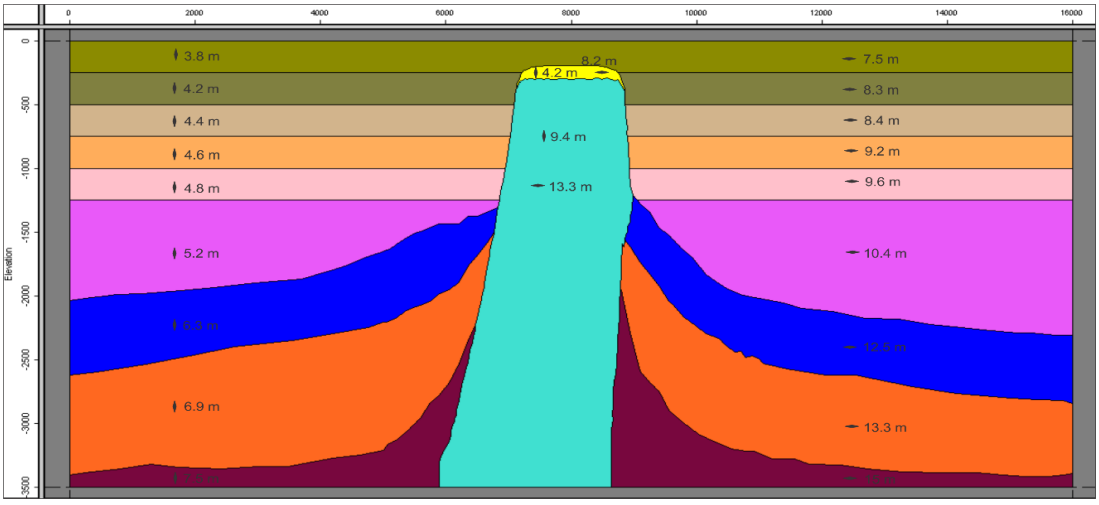

Figure 3.13 Vertical and lateral resolutions of actual 2-D seismic survey in certain depths after migration. Vertical and horizontal diamond shapes represent the vertical and lateral resolution, respectively.

Although the data had been collected close to the edge of the salt dome, the edge of the salt could not be imaged. Illumination analysis showed that this survey geometry can only provide images from the top of the salt and overlying cap rock layers since the reflections from edges of the salt dome are not recorded by the receivers (Figure 3.14 and Figure 3.15). As a result, a new 2-D seismic survey with larger offsets and better fold distribution should be carried out in order to image the salt and surrounding sediments.

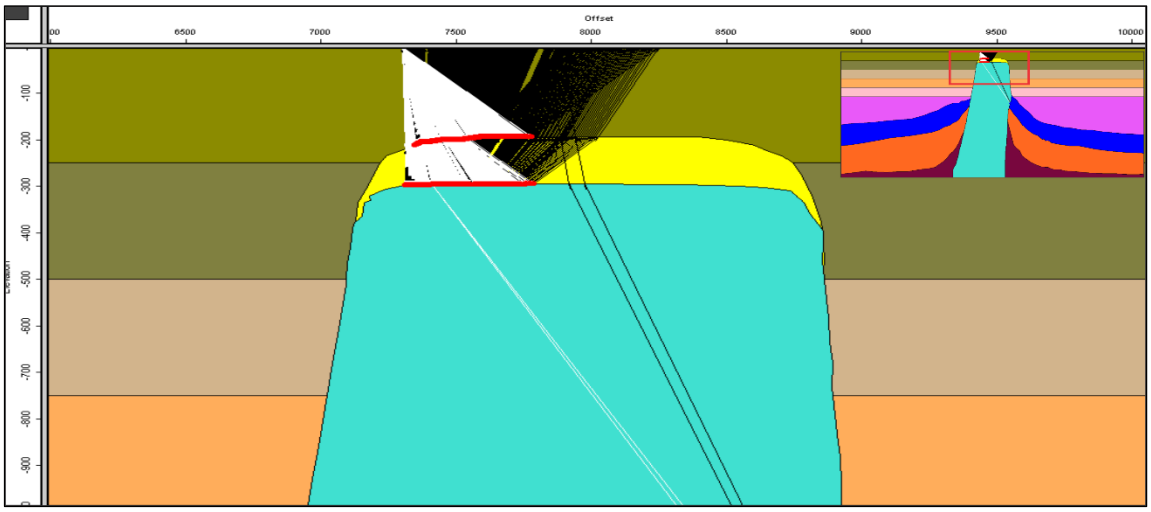

Figure 3.14. Illumination of the first shot in actual 2-D seismic survey.

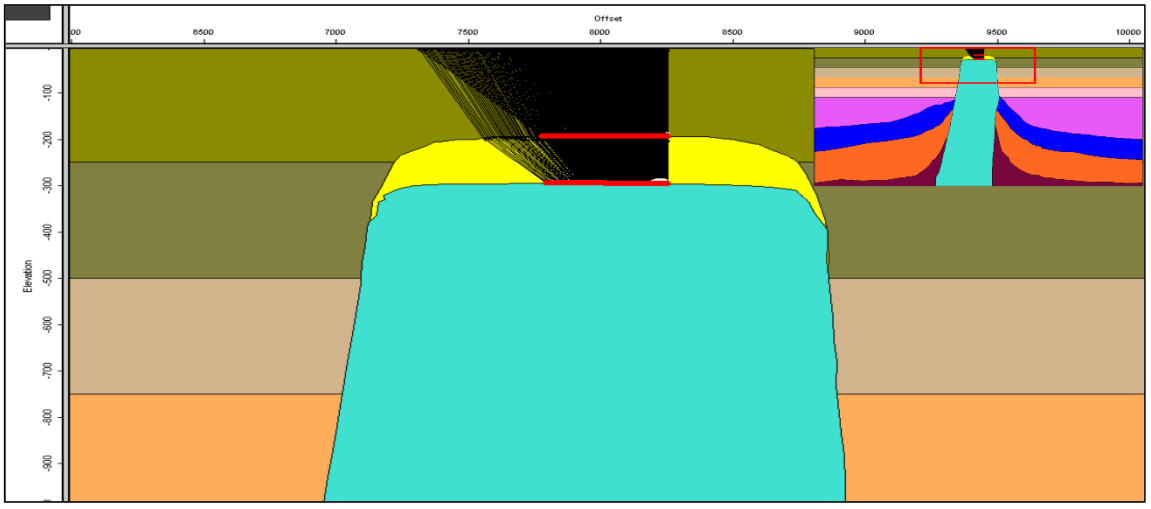

Figure 3.15. Illumination of the last shot in actual 2-D seismic survey.

3.2.3 2-D Seismic Survey Design using RTM Cases

Acquisition parameters calculated using general survey design equations are usually adequate to image the flat layers and slightly dipping surfaces. However, determining those parameters for complex structures, such as folds, faults, domes, and reefs is more difficult due to the complicated wave field behavior in these areas. Seismic data acquisition simulations over a model of the study area can provide crucial information for determining the survey parameters. If the model is constructed close enough to the real structure, it is possible to obtain very realistic synthetic seismic data by seismic modeling. Therefore, seismic modeling is one of the most economical ways to establish and test the optimum acquisition parameters for getting the best image over the complex geological structures.

In this part of the study, series of analyses were performed by seismic modeling to propose a conventional 2-D seismic survey with same limited acquisition equipment to image the salt structure and surrounding sediments. Pre-stack modeling (shot gathers) was done with finite difference method using full (two-way) acoustic wave equation. Reverse Time Migration (RTM) algorithm was used in pre-stack imaging part of the study since the velocity models consist complex and highly dipping structures. Unlike the other migration techniques, RTM uses the two-way acoustic wave equation without any approximations and assumptions (Baysal et al., 1983). Therefore, RTM makes imaging of the complex structures possible without any error and dip limitations. In this study, both pre-stack modeling and imaging were done using Paradigm's Echos software.

3.2.3.1 Maximum offset determination

The goal of the maximum offset determination process is to keep the maximum offset range as small as possible while remaining the events from important reflectors, which are necessary in migration, within recorded data. In order to determine the optimum offset range, different ranges were tested through pre-stack modeling and RTM imaging starting with the initial survey parameters. These initial survey parameters were chosen without considering the survey cost and time. First, maximum group interval was calculated from basic equations (Eq. 3.4 and 3.5) for spatial aliasing and Fresnel zone. Based on the calculations, the maximum group interval should be less than 13.3 m for 120 Hz maximum frequency, 70° maximum dip, and 3000 m/s average interval velocity of the model. So, maximum group interval was chosen as 10 m. Shots were generated for every two receiver stations with 20 m interval. Finally, 1600 receivers and 800 shots were used along 16 km spread for the initial pre-stack modeling. Shot and receiver configuration of the initial model is shown in Figure 3.16. Initial record length of the survey was chosen as 8 s.

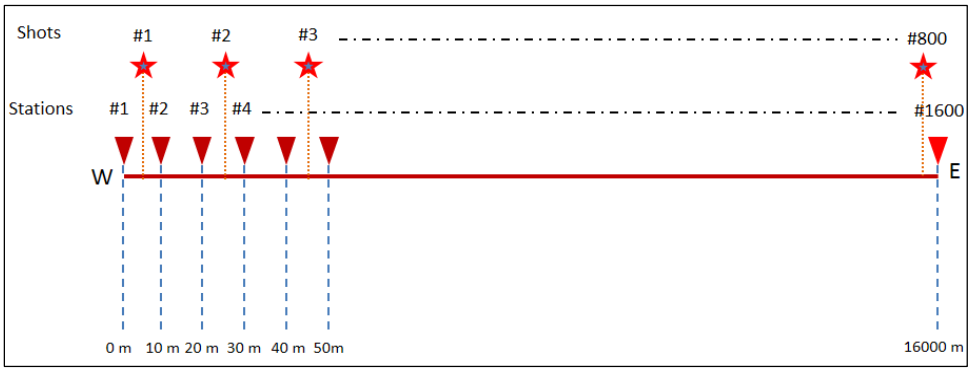

Figure 3.16. Initial shot and receiver configuration for pre-stack modeling.

The seismic source signal to create shot gathers was analyzed before generating the synthetic data. The autocorrelation of a linear vibroseis sweep results with a Klauder wavelet. Sweep length, sweep taper, and start and end frequencies of the sweep determine the shape of the source wavelet. To test the effect of sweep tapers on the source wavelet, three sweep signals were generated with same sweep length (12 s) and frequency (linear sweep from 10 Hz to 120 Hz) (Figure 3.17). According to sweep taper analyses, autocorrelation of sweep with 0.1 s taper showed narrower wavelet closer to a spike with better amplitude range. However, ringing artifacts can be seen on the power spectrum of the signal (Figure 3.18). Therefore, sweep taper can be chosen between 0.1 s and 1 s to have a desired source signal without the ringing artifacts. Also, the Butterworth source wavelet was compared with the Klauder. The Butterworth wavelet did not show a ringing artifact in the power spectrum and had fewer side lobes than the Klauder wavelet (Figure 3.19). Before deciding the source wavelet used in pre-stack modeling, example shot gathers were created with both the Klauder and Butterworth wavelets (Figure 3.20). Based on the examined shot gathers, the Butterworth source wavelets revealed better images compared to the Klauder wavelets, since the side lobes of the Klauder wavelets caused ringing effect on shot gathers, which is not desirable in data processing. Also, effects of the Klauder source wavelets can be seen in every part of the image since it is a long wavelet. Therefore, Butterworth wavelet was preferred as the source wavelet in pre-stack modeling.

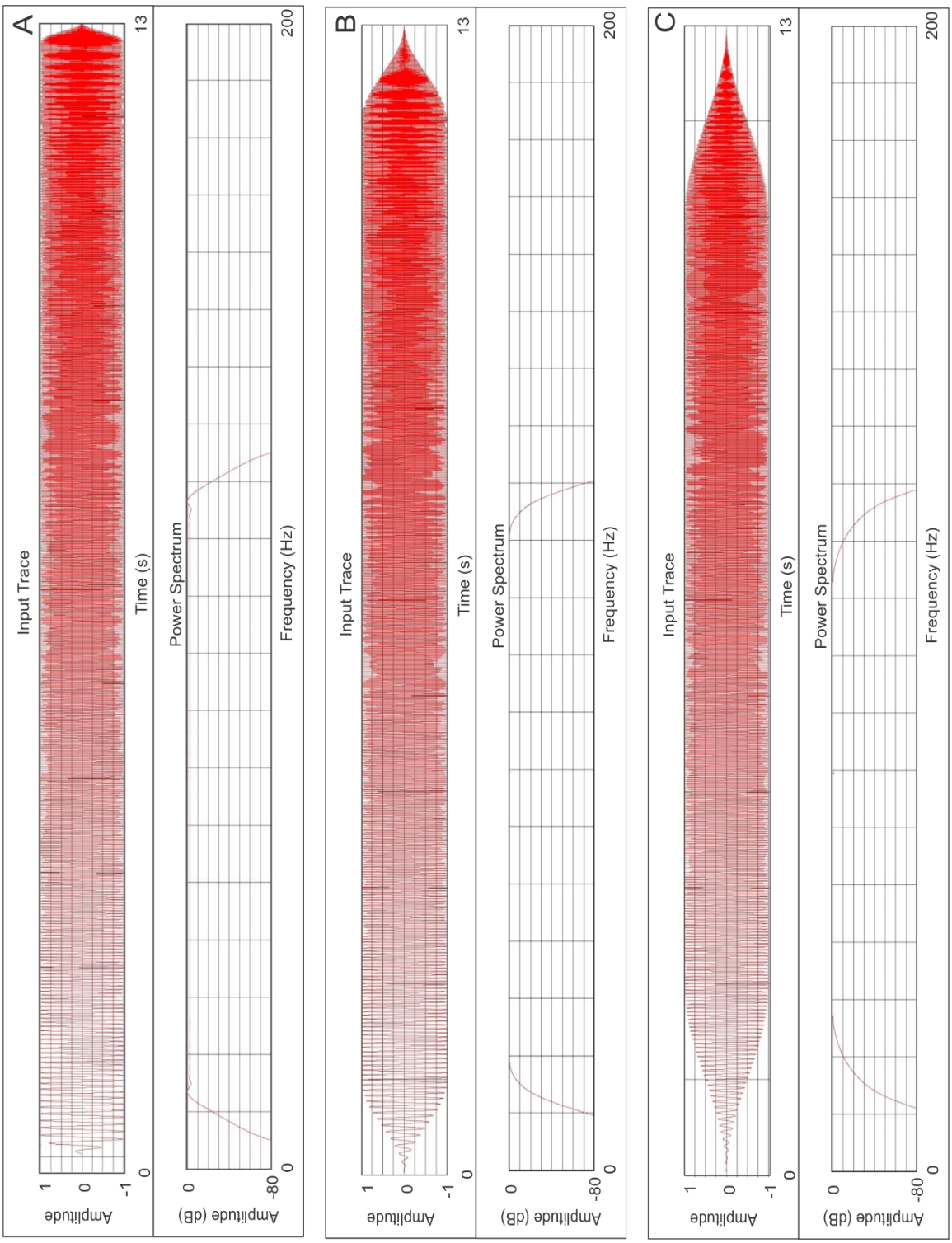

Figure 3.17 Vibroseis sweeps with different taper lengths: A) Taper length: 0.1 s, B) Taper length: 1 s, and C) Taper length: 2 s.

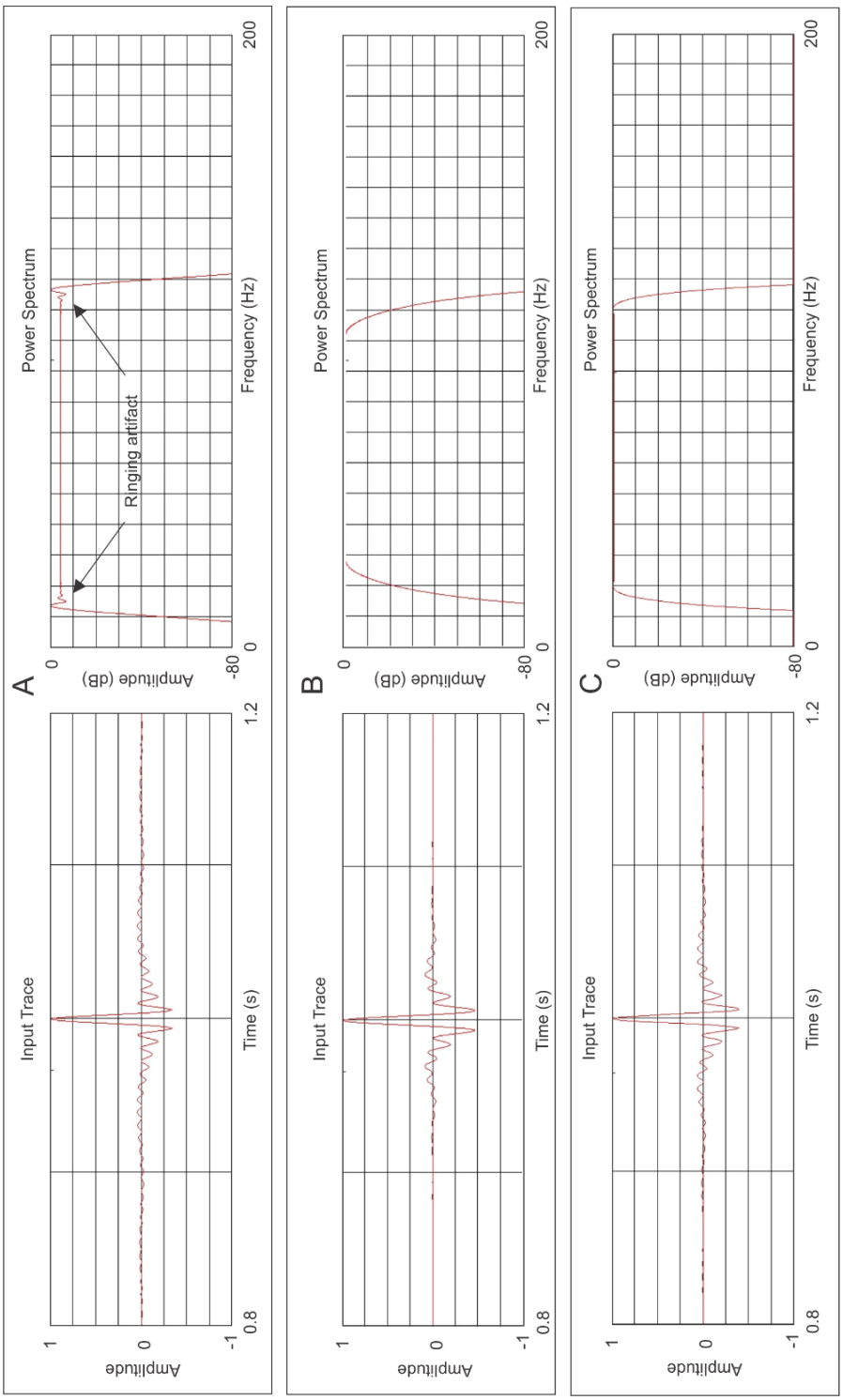

Figure 3.18 Klauder wavelets obtained by auto correlation of vibroseis sweeps with different taper lengths and their power spectrums: A) Taper length: 0.1 s, B) Taper length: 1 s, and C) Taper length: 2 s.

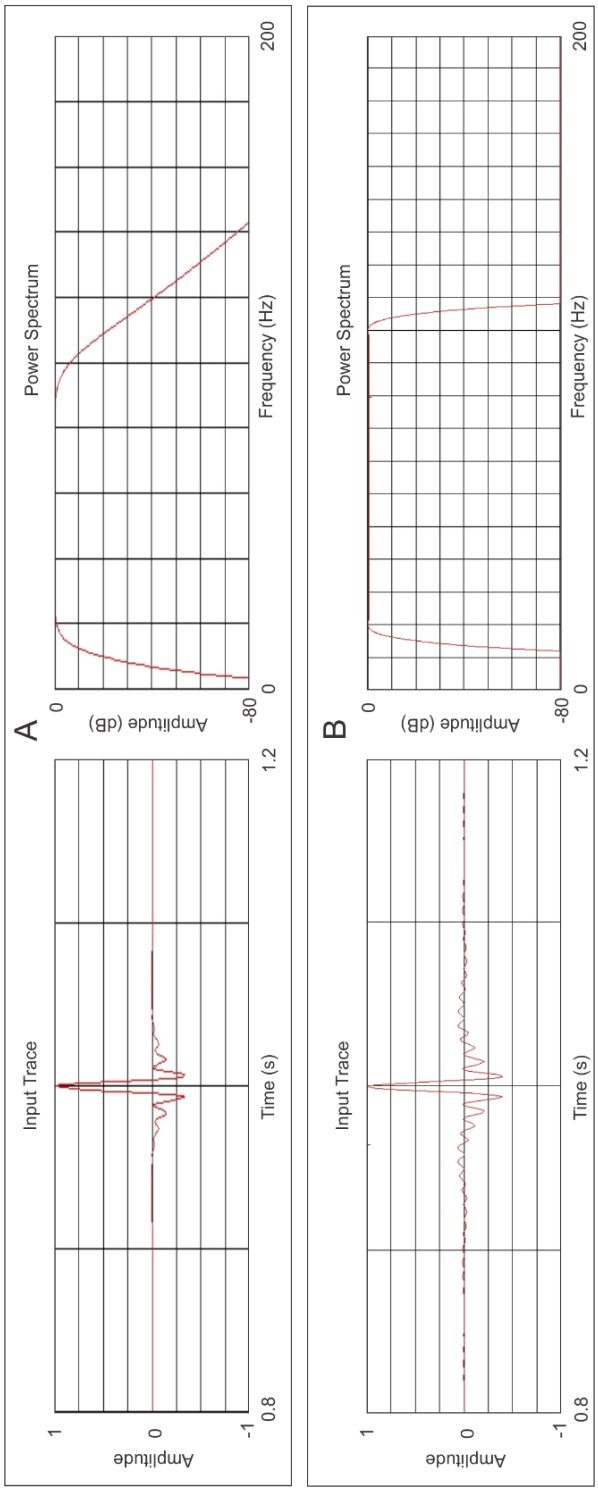

Figure 3.19 Comparison of the Butterworth and Klauder wavelets: A) Input trace and power spectrum of the Butterworth wavelet, and B) Input trace and power spectrum of the Klauder wavelet.

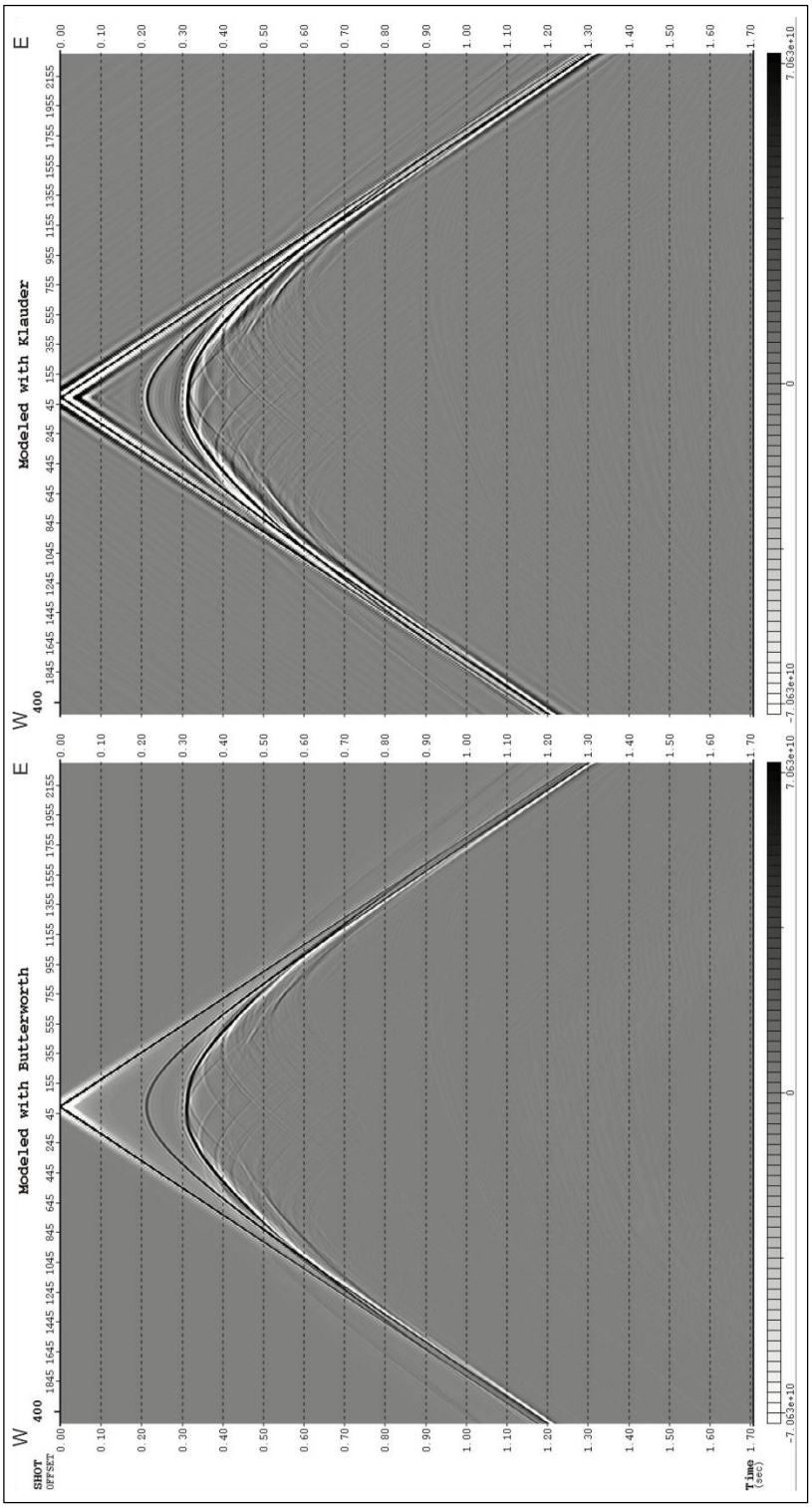

Figure 3.20 Comparison of the Butterworth and Klauder wavelets in modeled shot gathers. Color bar indicates the amplitude.

After source signal decision, raw shot gathers were modeled using initial survey parameters. Reverse Time Migration was applied to raw shot gathers to obtain the images from every shot. In addition to RTM images, illumination analysis with ray tracing was done to demonstrate the contribution of every shot. RTM images of the first, middle, and last shots and illumination of those shots are shown in Figure 3.21-3.23, respectively. As seen on these figures, it is obvious that all shots provide important information from different events to the final RTM image. Especially, shots far from the salt structure allow us to record the reflections and diffractions generated from dipping layers and edge of the salt dome. The shots located closer to the salt dome contribute to the final image by illuminating the near surface reflections coming from the top of the salt, cap rock and shallow layers.

In the final RTM image obtained from raw shots, the effects of the first breaks appeared as low frequency noise, especially on shallow parts of the data (Figure 3.24). This low frequency noise makes the shallow events unclear to interpret. Thus, first breaks were eliminated from each shot to increase the quality of the data (Figure 3.25). Comparison of RTM images before and after first break elimination is shown in Figure 3.26. It is obvious that elimination of the first breaks made the top of the salt, cap rock and shallow horizontal layers more interpretable.

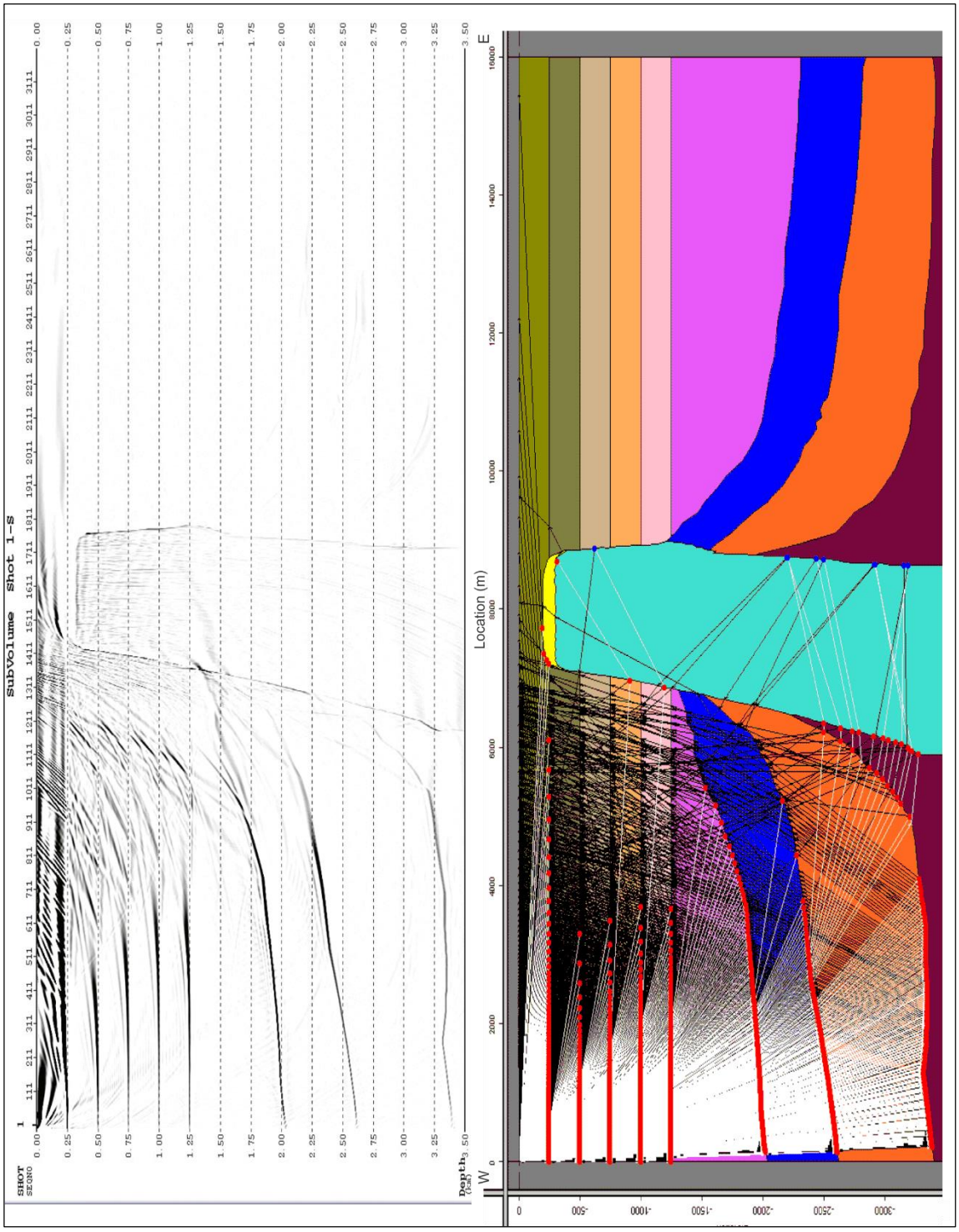

Figure 3.21. Sub-volume of first shot after RTM (above) and illumination of first shot for initial survey parameters (below).

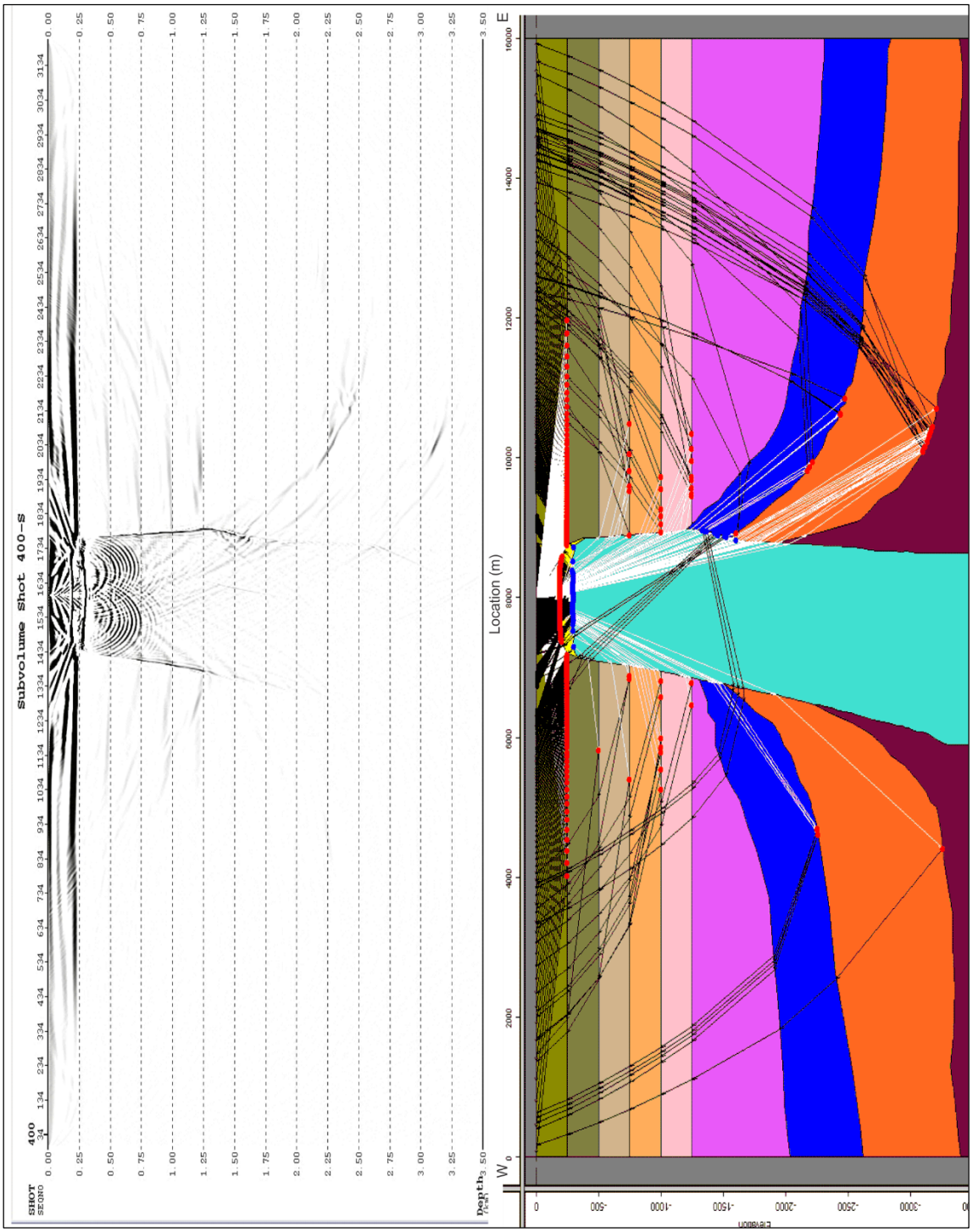

Figure 3.22. Sub-volume of the middle shot after RTM (above) and illumination of middle shot for initial survey parameters (below).

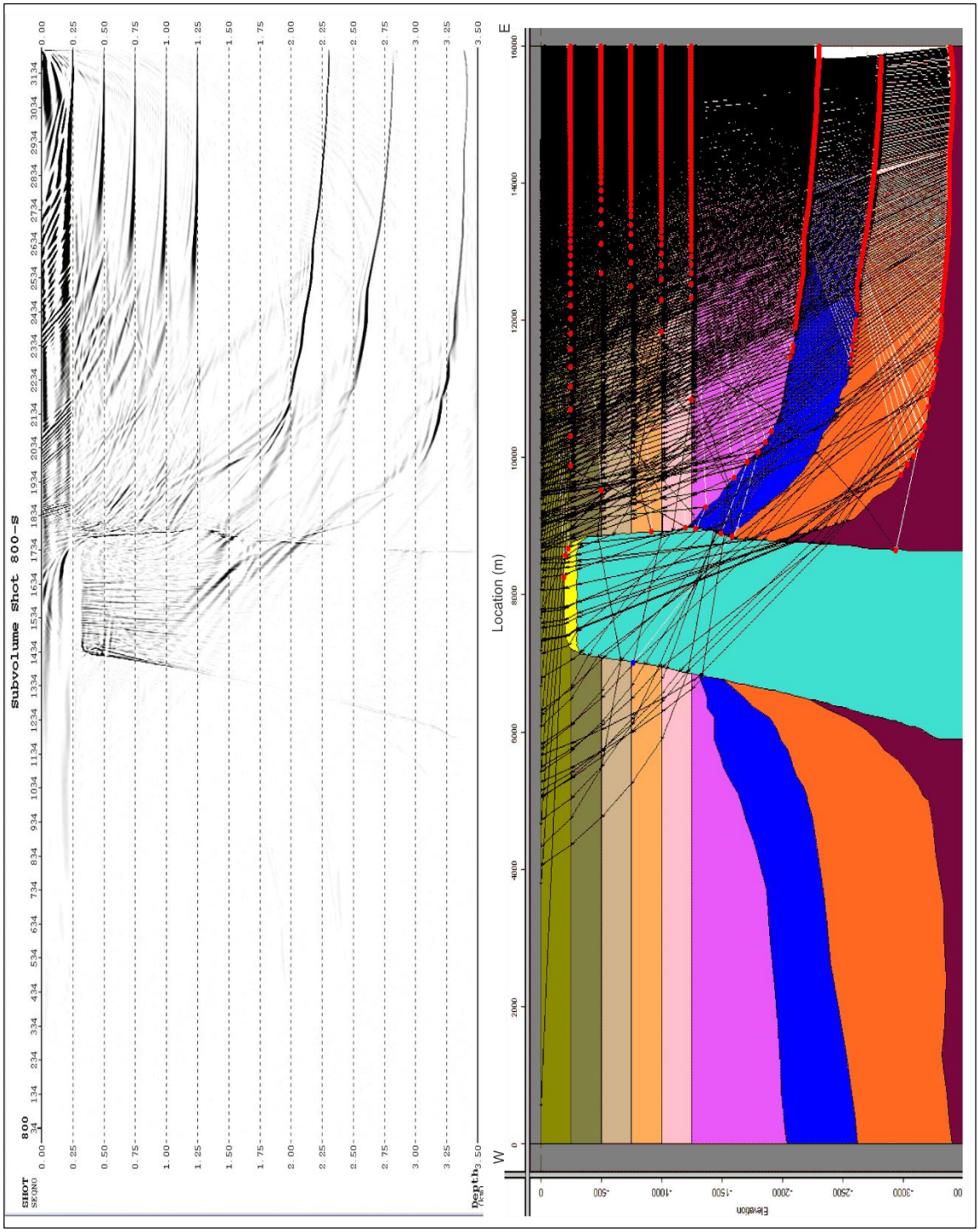

Figure 3.23. Sub-volume of the last shot after RTM (above) and illumination of last shot for initial survey parameters (below).

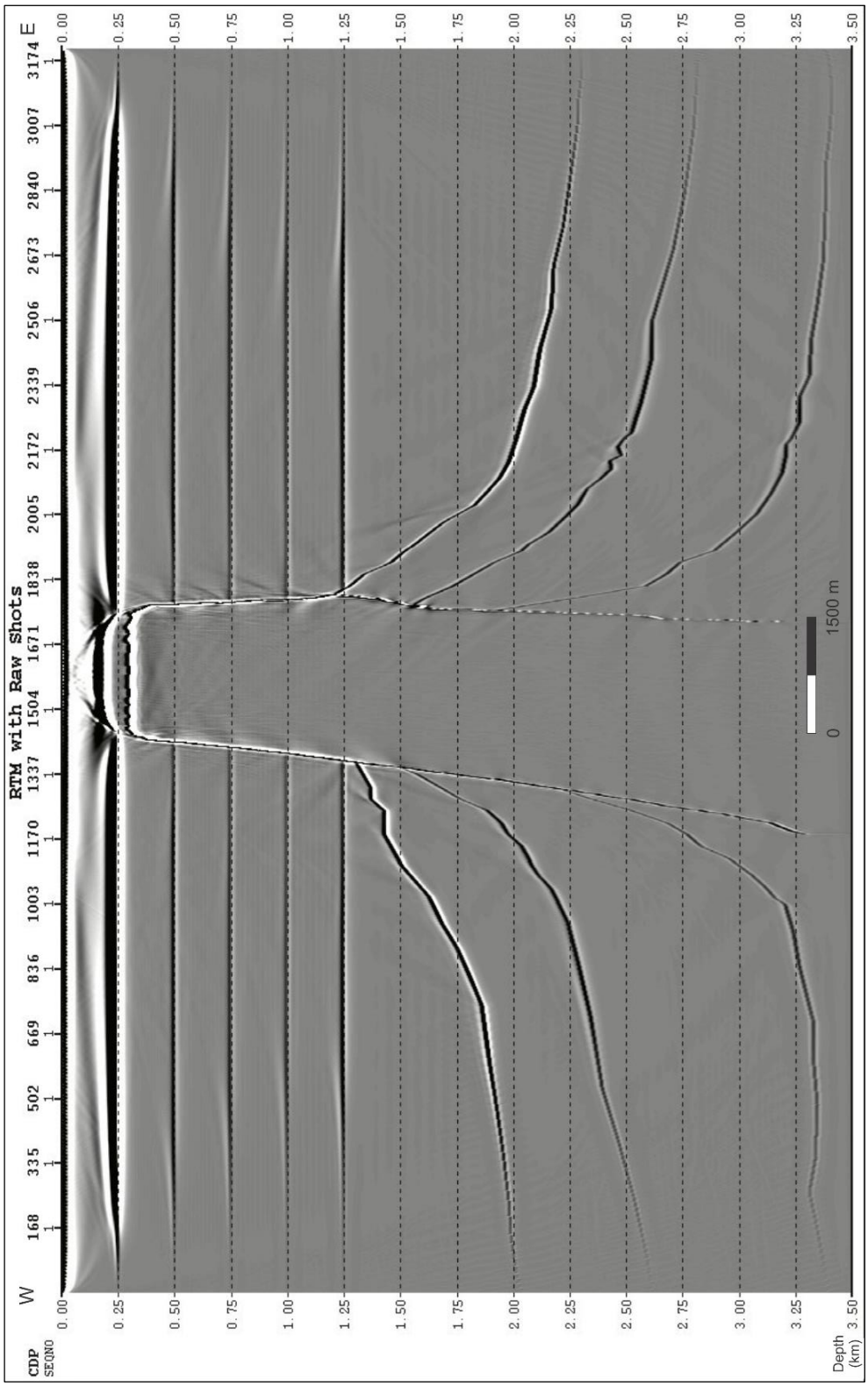

Figure 3.24. Final RTM image obtained from raw shot gathers

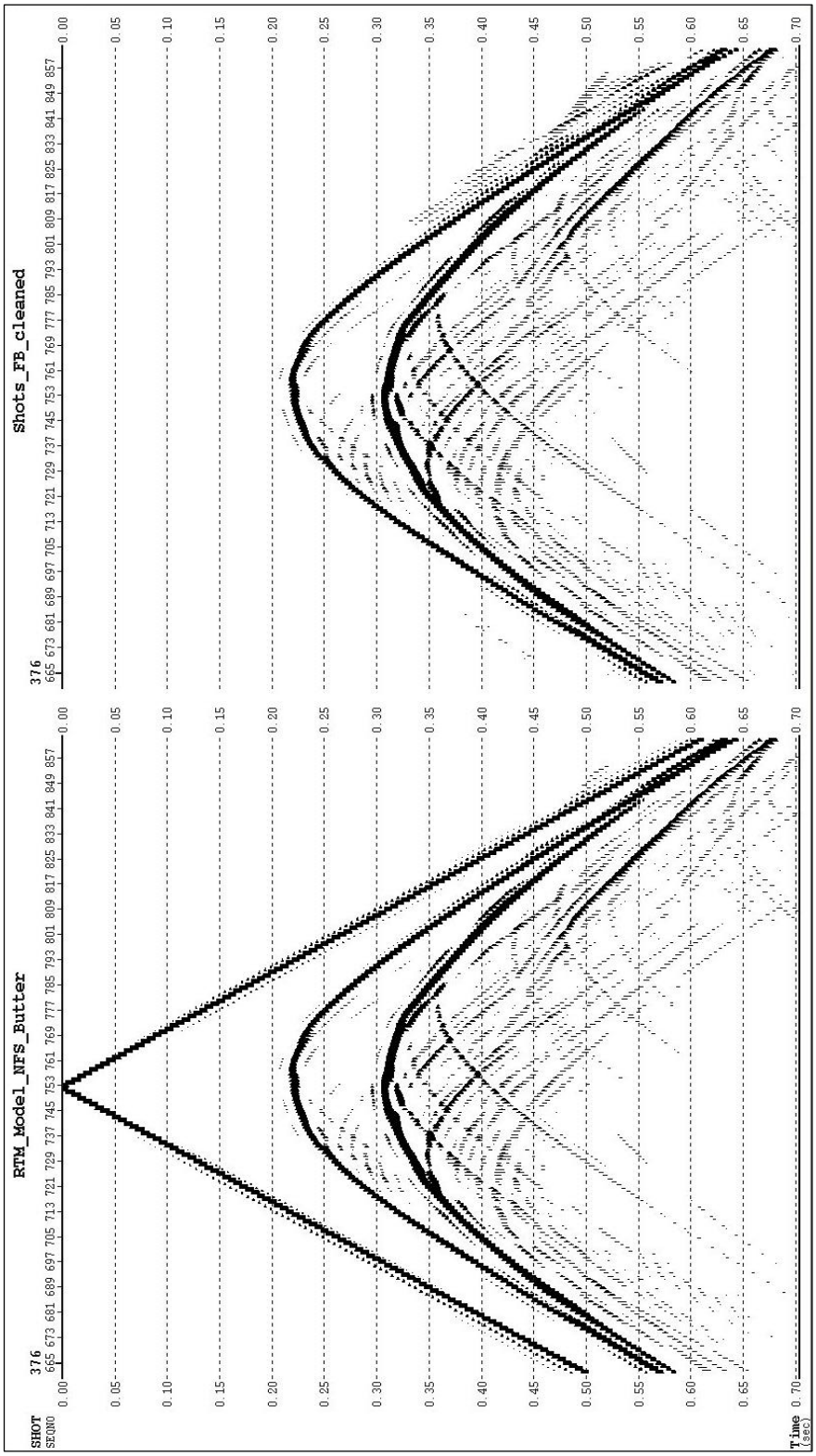

Figure 3.25. Raw and first break elimination applied shot gathers (Shot number 376).

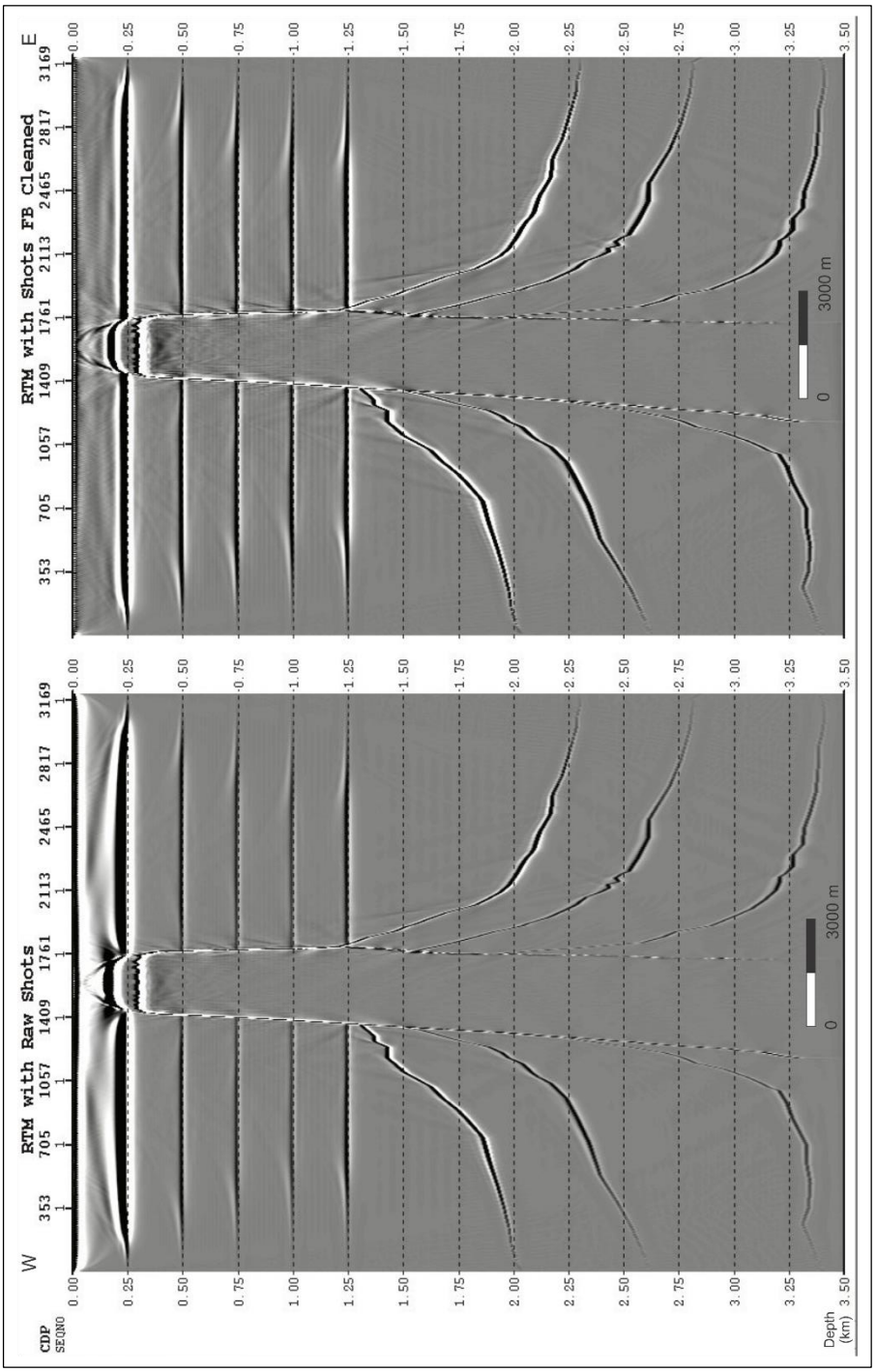

Figure 3.26. Comparison of final RTM images obtained from raw (left) and first break eliminated (right) shot gathers.

The offset range contribution is important to update the initial survey parameters and limit the maximum offset of the survey. To understand the contribution of different offsets, the images from 0 - 6000 m, 6000 - 11,000 m, and 11,000 – 16,000 m offsets were analyzed (Figure 3.27-3.29). According to comparison of the offset ranges, albeit all offset ranges assist the image for a better quality, best contribution to the RTM images is from 0 – 6000 m offset range (Figure 3.30). Also, images from 6000 – 11,000 m and 11,000 – 16, 000 m offset ranges showed that these offset ranges generated low frequency noise at shallow depths where horizontal or slightly dipping layers are existed. Therefore, updating the initial survey parameters for 6000 m offset range was possible. However, the offset range is still too large for intended acquisition equipment.

In order to limit the maximum offset of the survey, same offset contribution analyses were made for 0 – 6000 m, 0 - 3000 m, and 0 – 1500 m offset ranges. All the three RTM images from different offset ranges did not show much difference in terms of image quality (Figure 3.31-3.32). This comparison allowed us to limit the maximum offset range to 1500 m, which is a reasonable parameter for the limited acquisition equipment. Note that the 0 – 1500 m offset range equals to 3000 m receiver line, since the shot is fired in the middle of the receiver line in conventional split-spread seismic surveys. Finally, the initial maximum offset was reduced from 16,000 m to 3000 m by analyzing the contribution of offset ranges in RTM images. Moreover, number of receivers were reduced from 1600 to 300 by updating the offset range. Figure 3.33 illustrates the conventional seismic survey layout with the updated maximum offset parameter.

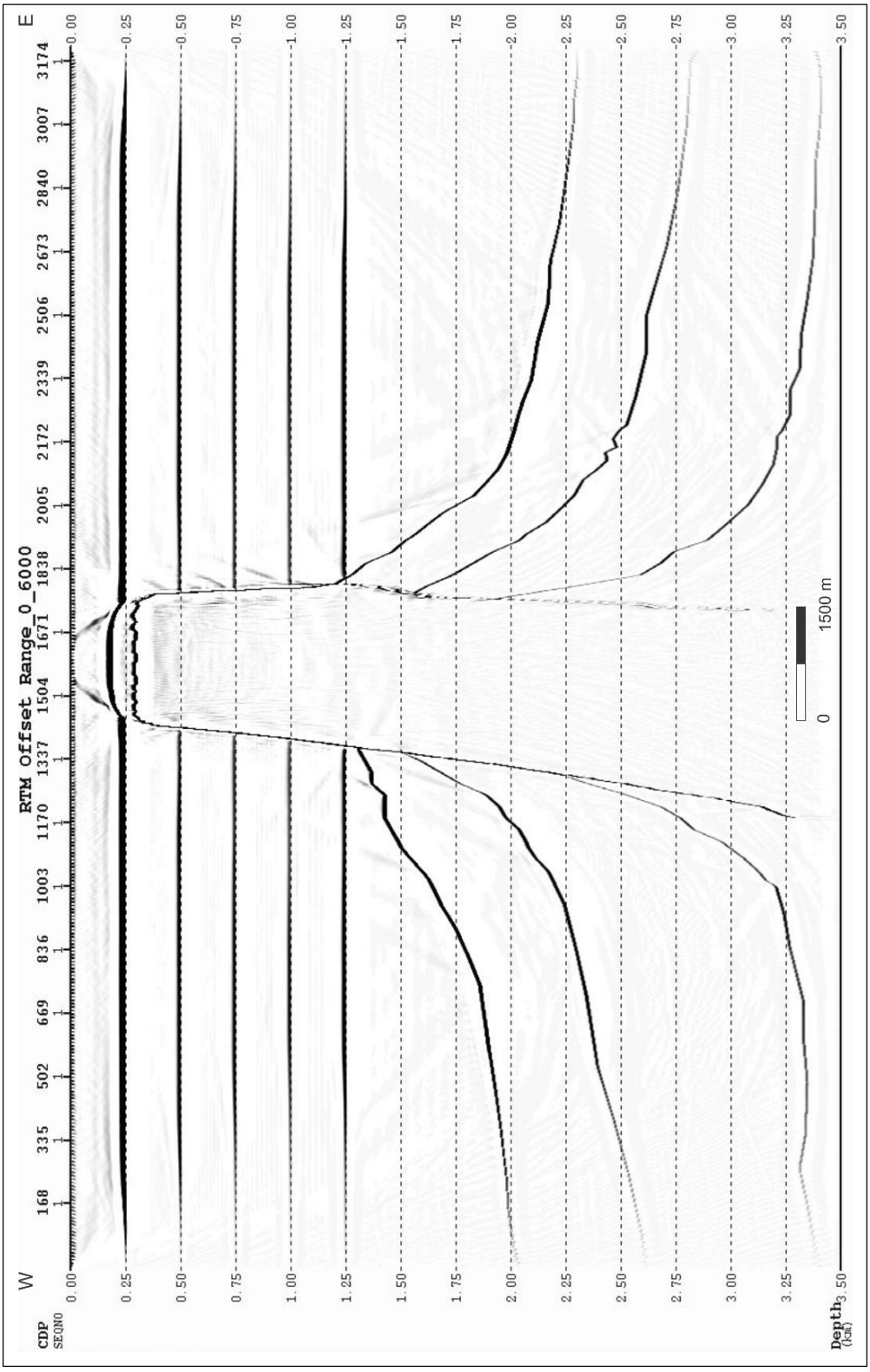

Figure 3.27. RTM image obtained using 0 – 6000 m offset range.

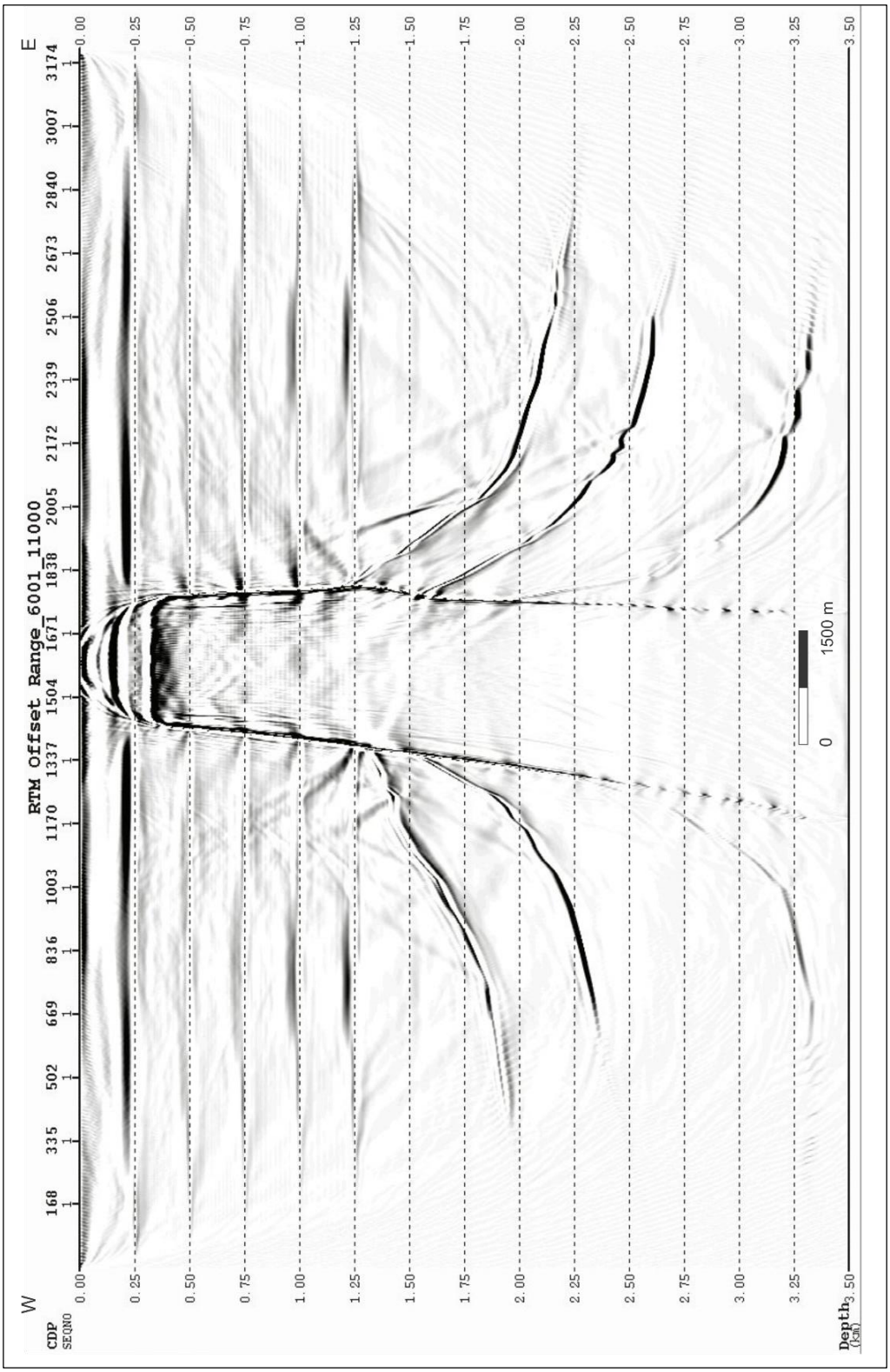

Figure 3.28. RTM image obtained using 6000 – 11000 m offset range.

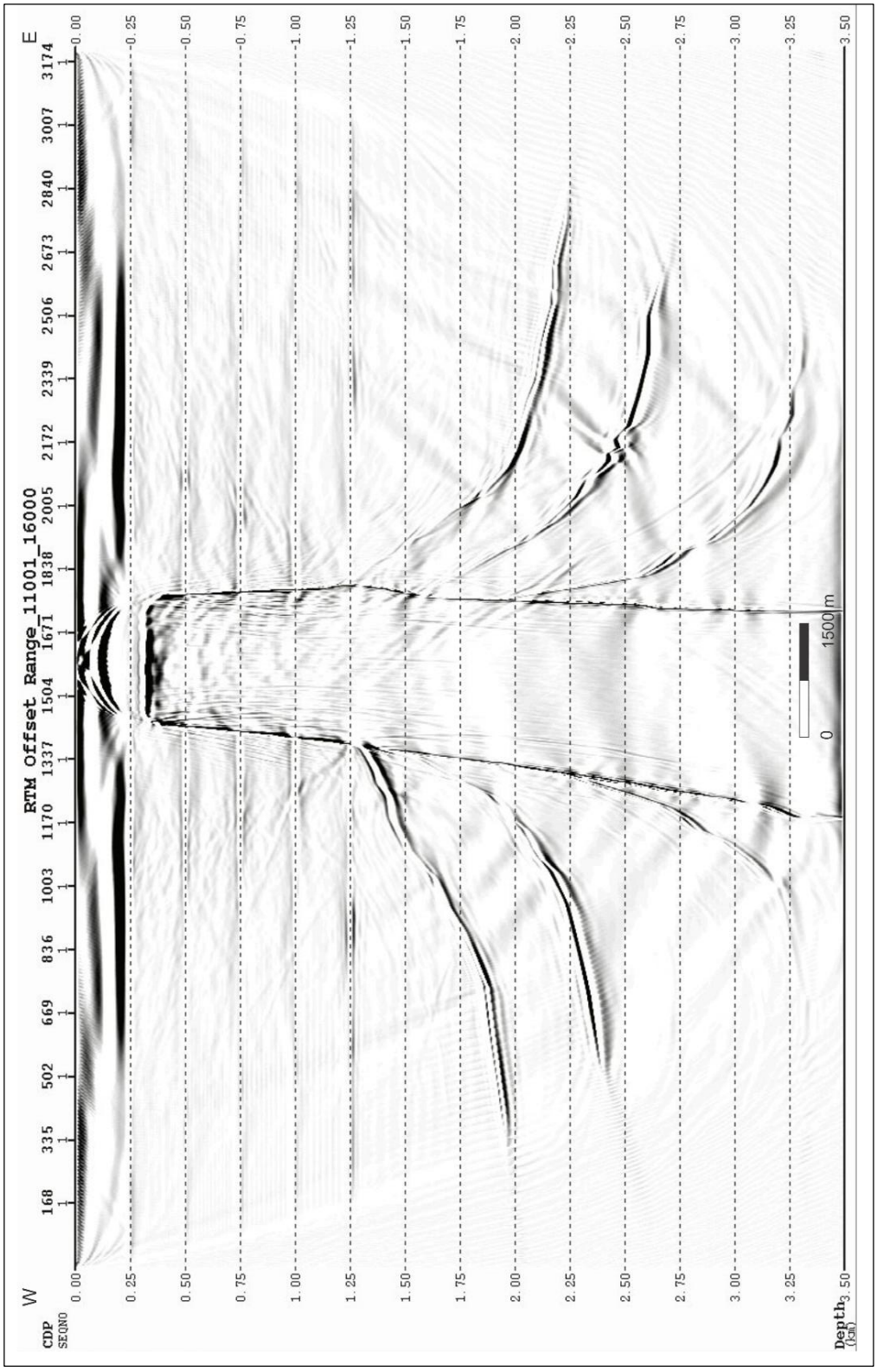

Figure 3.29. RTM image obtained using 11000 – 16000 m offset range.

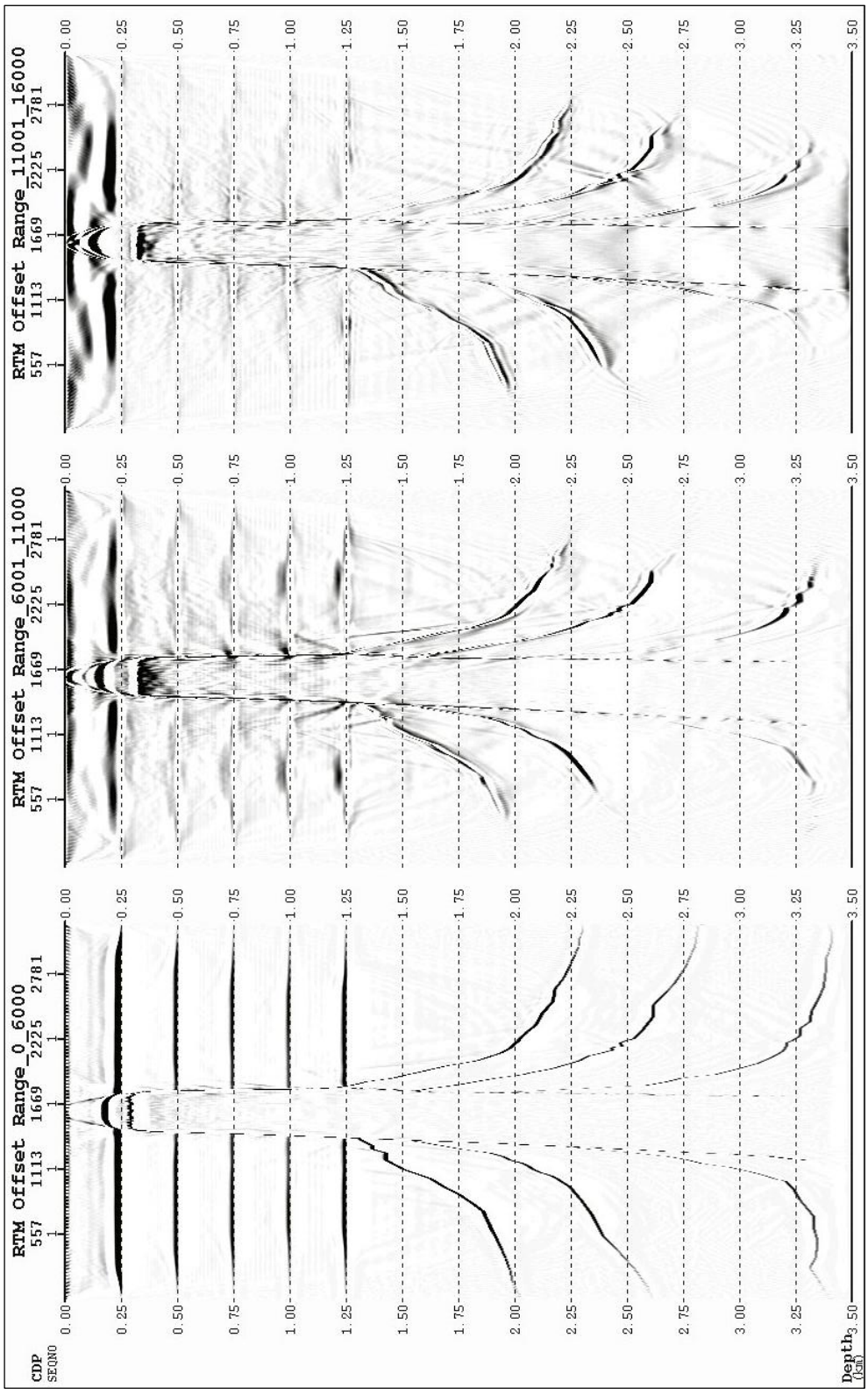

Figure 3.30. Comparison of RTM images obtained using different offset ranges.

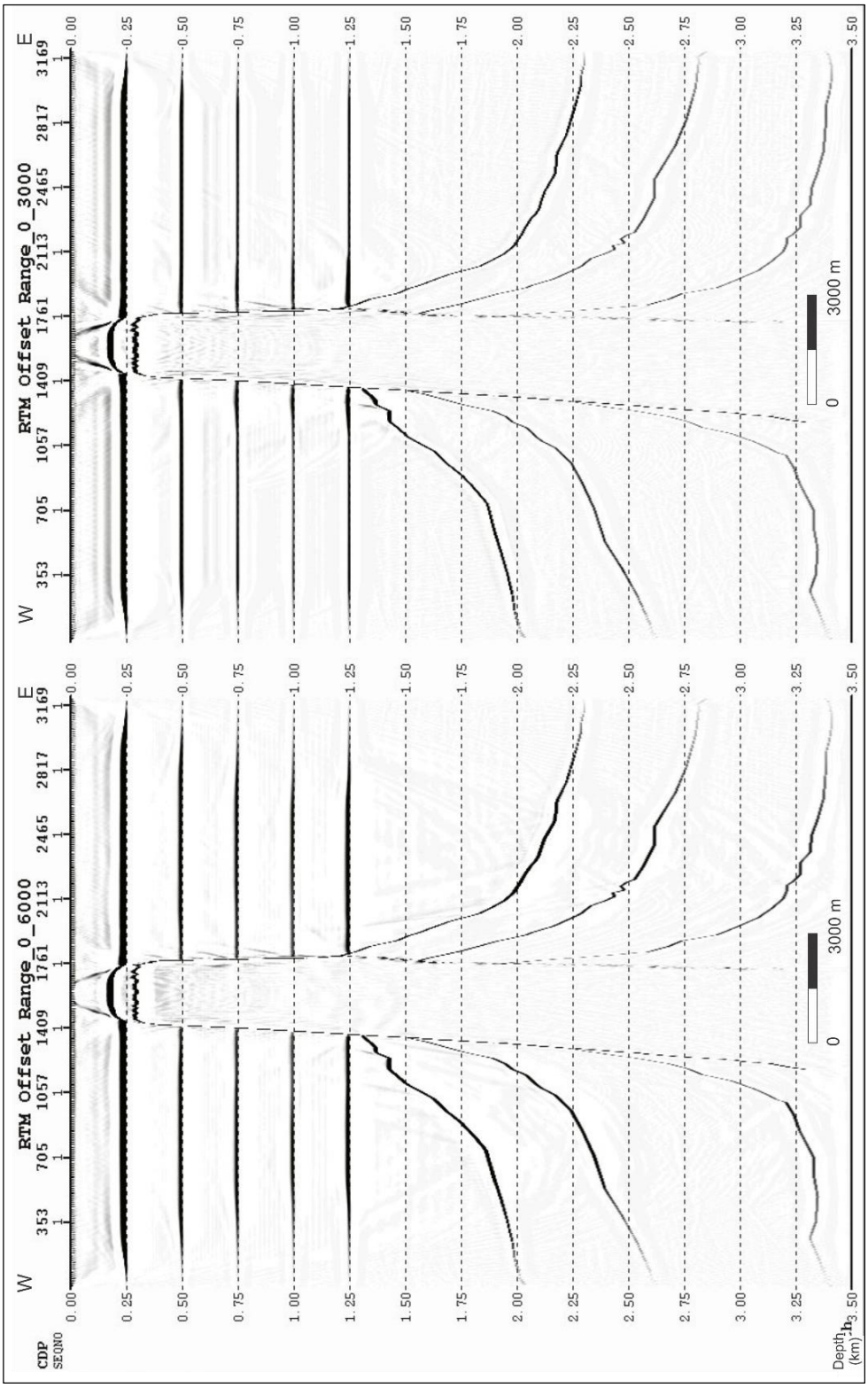

Figure 3.31. Comparison of RTM images obtained using 0-6000 m and 0-3000 m offset ranges.

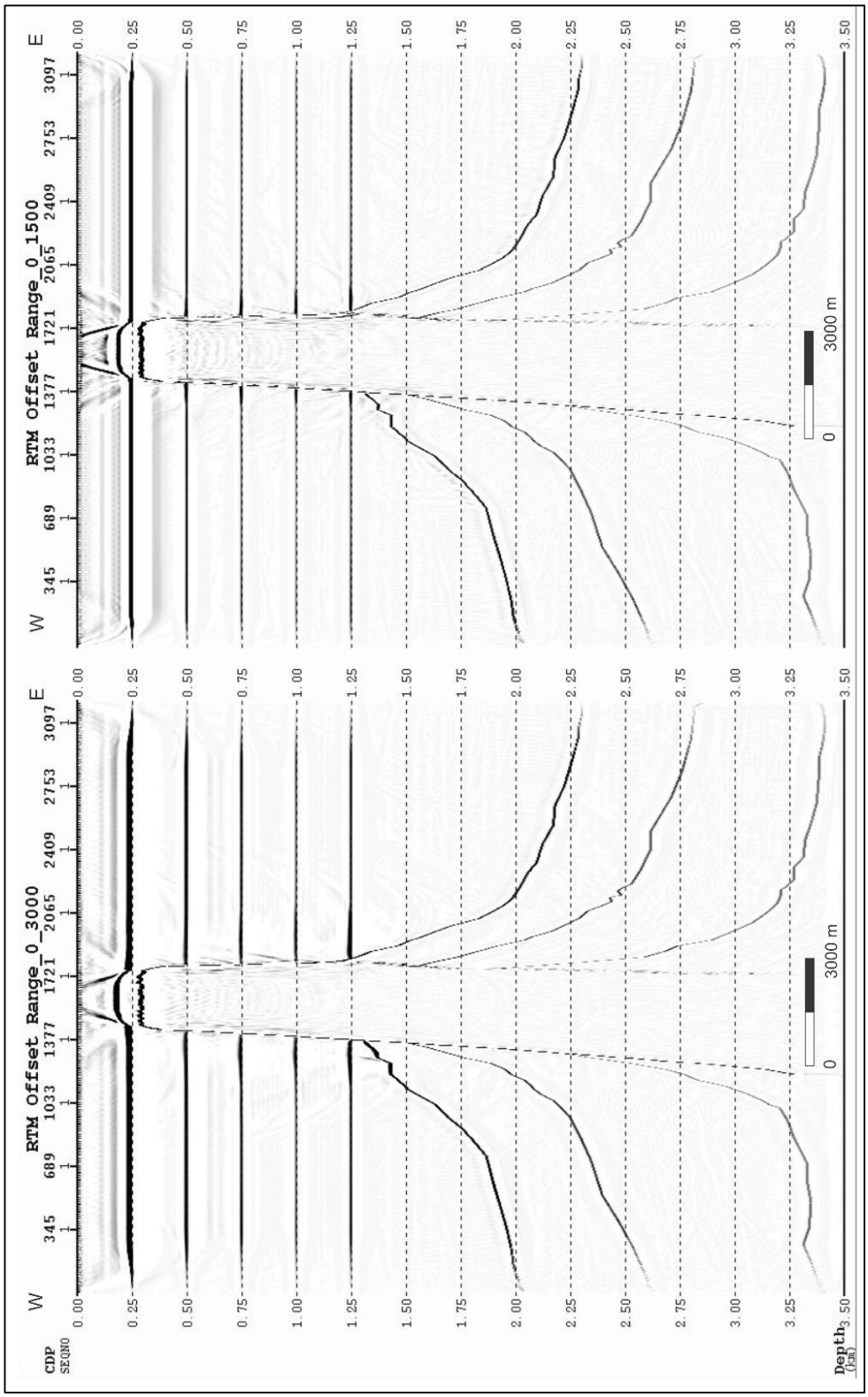

Figure 3.32. Comparison of RTM images obtained using 0-3000 m and 0-1500 m offset ranges.

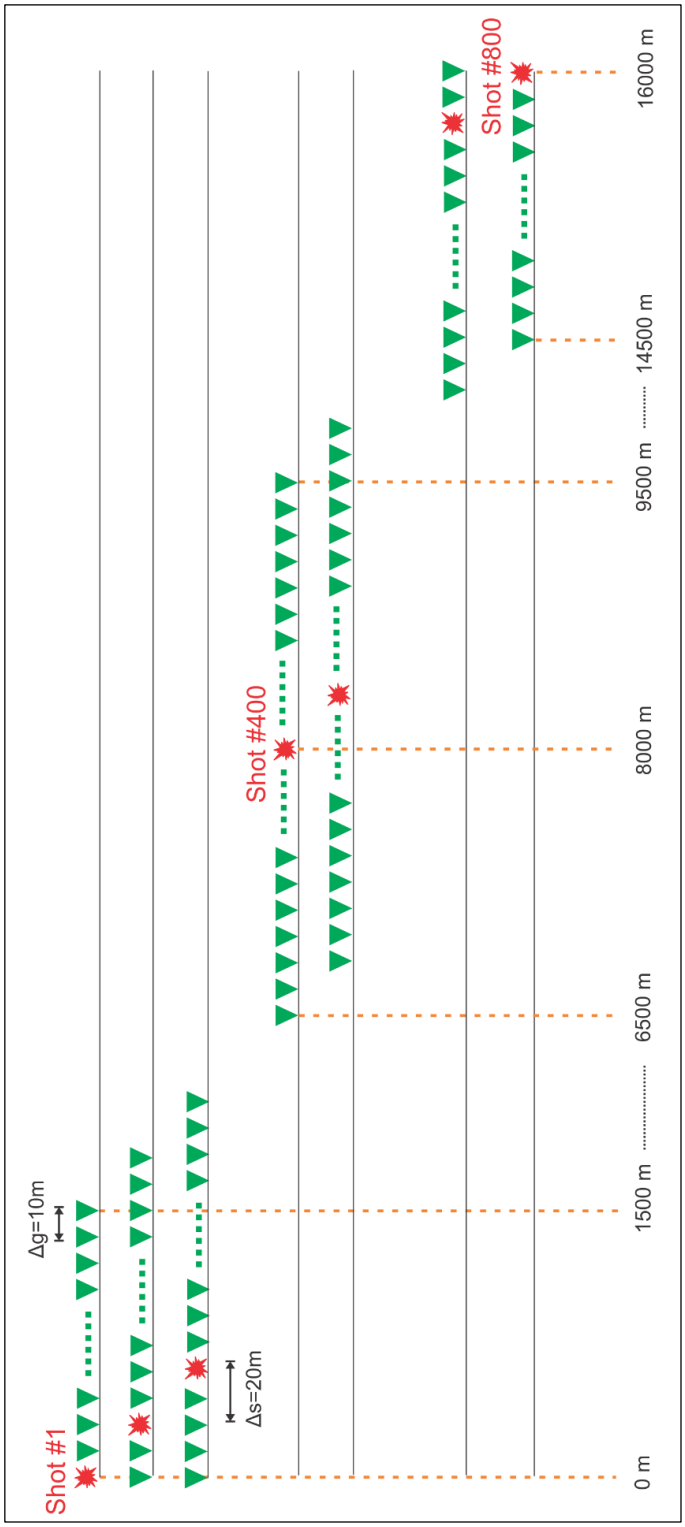

Figure 3.33. Survey layout after updating the maximum offset range. Green triangles and red stars represent the receivers and shots, respectively.

3.2.3.2 Group interval determination

As mentioned earlier, number of receivers was reduced to 300 by the maximum offset minimization. The maximum group interval is another parameter that determines the number of receivers. In initial survey parameters, the maximum group interval was selected as 10 m due to the spatial aliasing limit. However, for such complex models it is possible to obtain larger group interval by testing the survey with seismic imaging in terms of resolution. Data were modeled with 10 m and 20 m group intervals to see the difference between two parameters. According to RTM images in Figure 3.34, although the image obtained using 20 m group interval shows some aliasing in certain areas, it still meets our expectations for imaging the salt dome and surrounding sediments. Therefore, it was decided to update the group interval as 20 m. By this way, number of receivers will be reduced by half and the required limit of equipment will be met. So, imaging tests for larger group intervals were not required, since the number of receivers was affordable.

3.2.3.3 Shot interval determination

Interval between the shot stations is important to determine the fold of the survey. Smaller shot intervals provide better signal-to-noise ratio. The best way to determine the shot interval is doing field tests at the beginning of the survey. In case of skipping field tests and having no information about the survey environment, shot interval can be decided by seismic modeling and imaging tests.

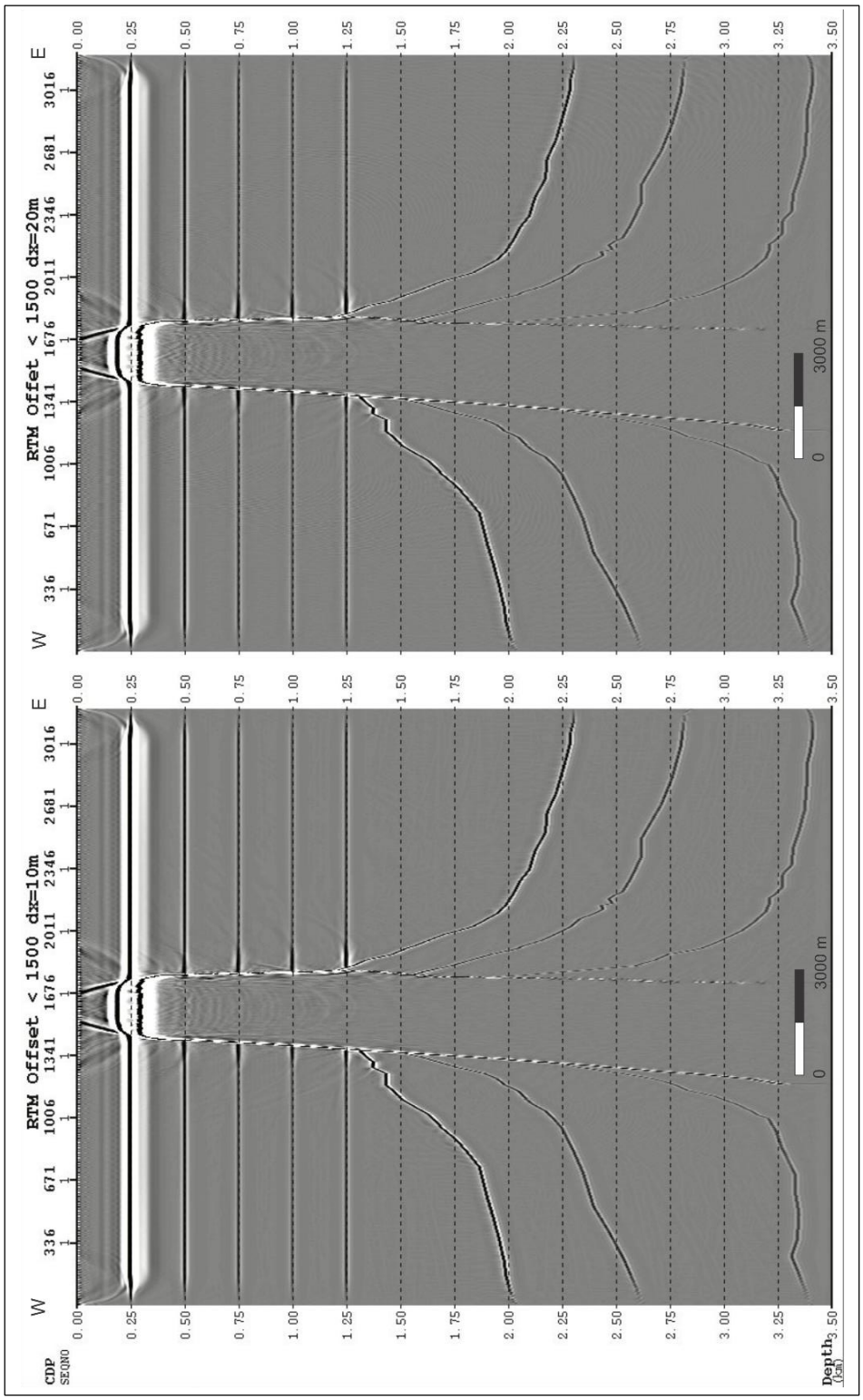

Figure 3.34. Comparison of RTM images that are modeled with 10 m (left) and 20 m (right) group intervals.

Also, it is possible to increase the number of vertical stacks to obtain better signal-to-noise ratio without changing the shot interval, if the signal-to-noise ratio is lower than expected.

The shots were modeled with 40 m, 80 m, 160 m, and 320 m shot intervals to understand their effects to the data. As seen in Figure 3.35, the larger shot interval caused more noise in the image, especially on the shallower parts. However, none of the four RTM images showed much difference at the deeper parts of the data, which is the area of interest for this survey. Random noise which was not taken into account in this analysis, could change the image quality. Therefore, shot interval was used as 40 m to keep the fold as high as possible. According to updated parameters, the maximum fold of the survey was calculated as 37.5.

3.2.3.4 Record length determination

Record length is one of the parameters that directly affects the survey duration. Optimum record length should be long enough to record any diffraction patterns coming from the deepest event of interest in order to perform a successful migration. Shots were modeled with shorter record lengths in order to update the initial record length of the survey to the optimum record length. The goal of this process is determining the shortest recording time that allows us to image the target zones without losing important events. RTM images of modeled shots with 8 s, 4 s, 3 s, and 2 s record length were compared with each other. As seen on Figure 3.36, 8 s record length is unnecessarily long, since the image of the data that is modeled with 4 s record length meets the same imaging needs already.

On the other hand, the data below 2.25 km could not be imaged, since 2 s record length is very short to record the diffractions coming from deeper events required for migration. Images with 3 s and 4 s record lengths were examined in terms of data resolution. Figure 3.37 points out that the data modeled with 3 s record length is not capable to image the salt flanks and steeply dipping layers in deeper parts. However, there is not much difference in resolution between two images at depths above 2 km. Thus, 3 s record length is a suitable selection, if the area of interest is between 0 – 2 km depth. But, record length was determined as 4 s for this study in order to image the area down to 3.5 km.

3.2.3.5 Profile length determination

Analyzing the length of the profile by seismic imaging is a useful strategy for survey cost reduction. The shot spread length can be limited according to imaging needs of the survey. In this study, the goal of this survey is to image the salt dome and surrounding sediments clipped at the flanks of the salt. Therefore, imaging the sediment layers far from the salt dome is not required. Establishing the optimum shot spread length is possible by imaging the data with different shot ranges. 0 – 800, 101 – 700, 201 – 600, and 301 – 500 shot ranges were imaged with updated survey parameters in order to find out the shortest shot spread length that provides the imaging needs of the survey. Figure 3.38 and Figure 3.39 shows that shot spread lengths between 0 - 800 and 101 – 700 provided seismic images more than necessary. On the other hand, resolution of the image obtained using 301 – 500 shot range is very poor to illuminate the steep dipping events (Figure 3.40). Consequently, 201 -600 shot range equal to 8 km was chosen as the

optimum shot spread length. After determining the shot spread profile length of the survey was calculated as 11 km (Figure 3.41).

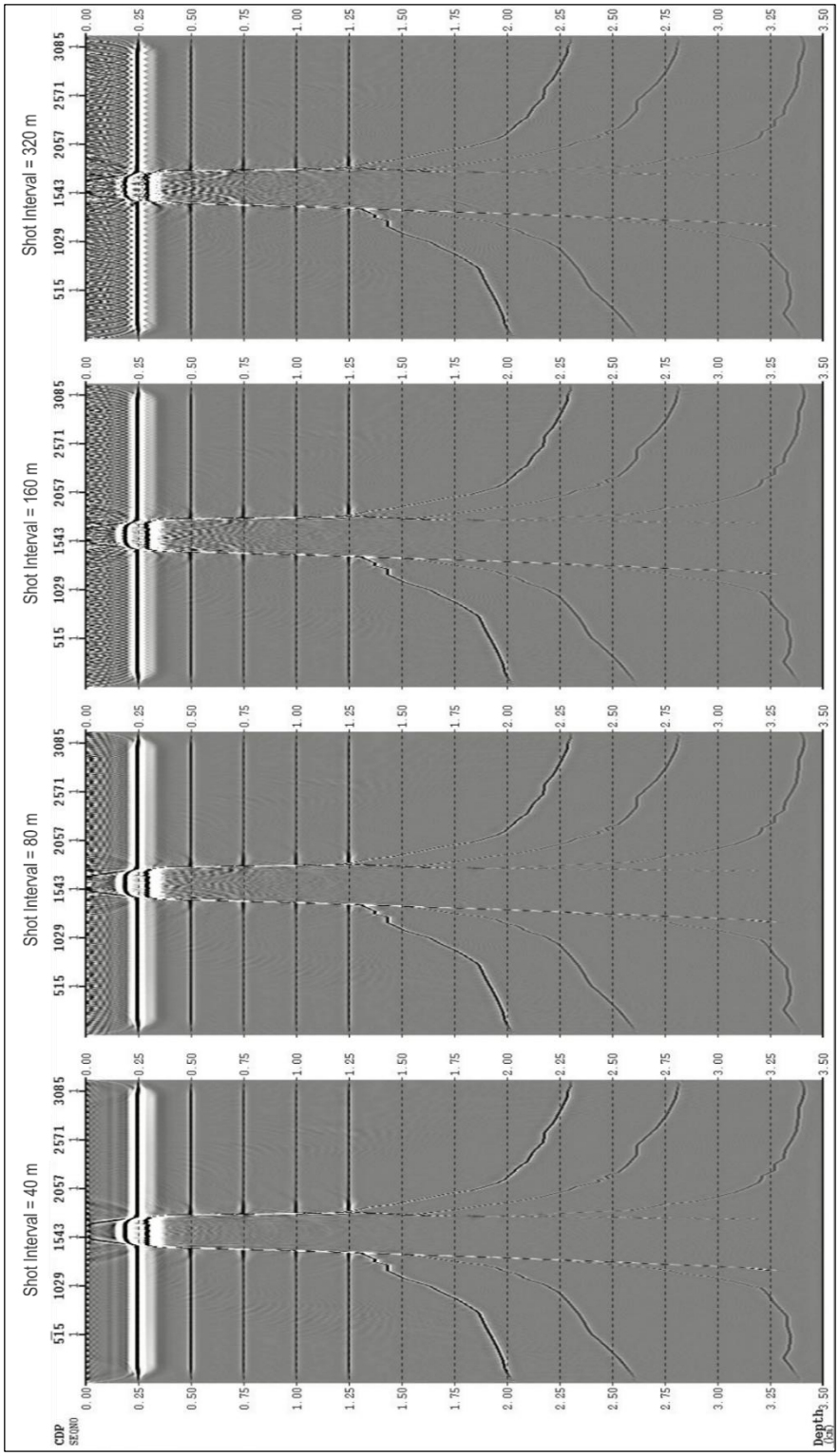

Figure 3.35. Comparison of RTM images that are modeled with 40 m, 80 m, 160 m and 320 m shot intervals.

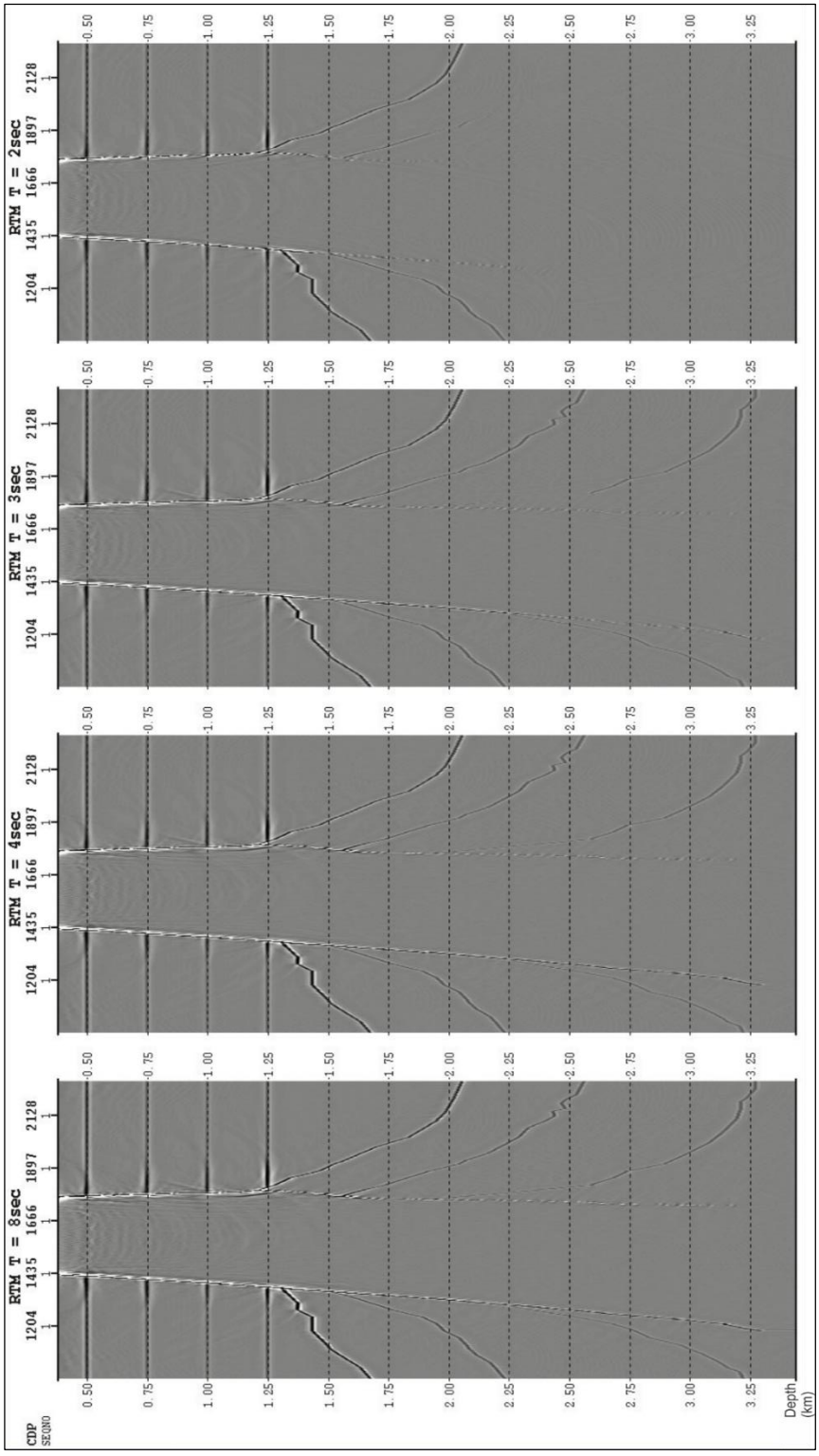

Figure 3.36. Comparison of RTM images that are modeled with 8 sec, 4 sec, 3 sec, and 2 sec record lengths.

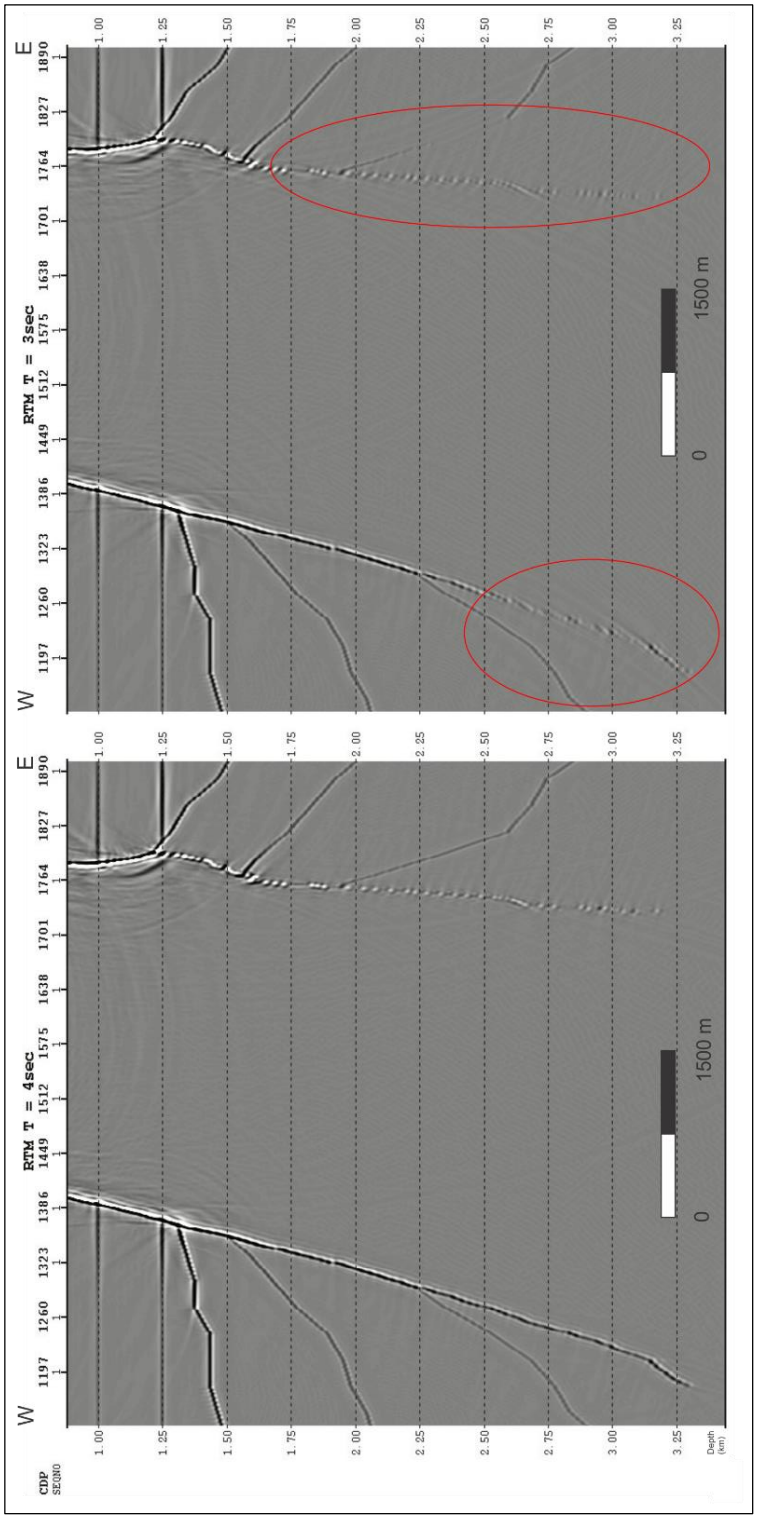

Figure 3.37. Comparison of RTM images that are modeled with 4 sec and 3 sec record lengths. Red circles highlights the poorly imaged areas.

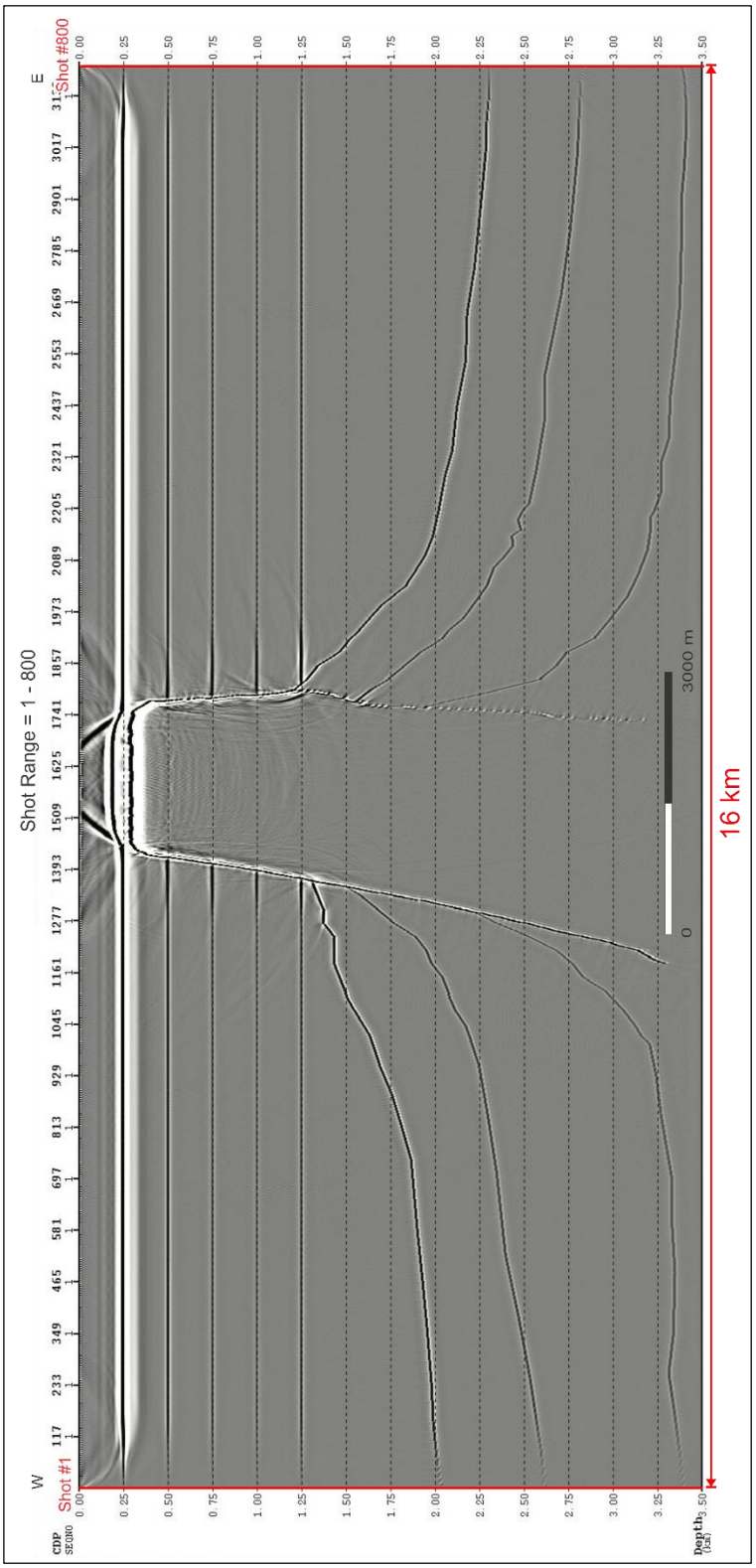

Figure 3.38. RTM image that is modeled with 1-800 shot range.

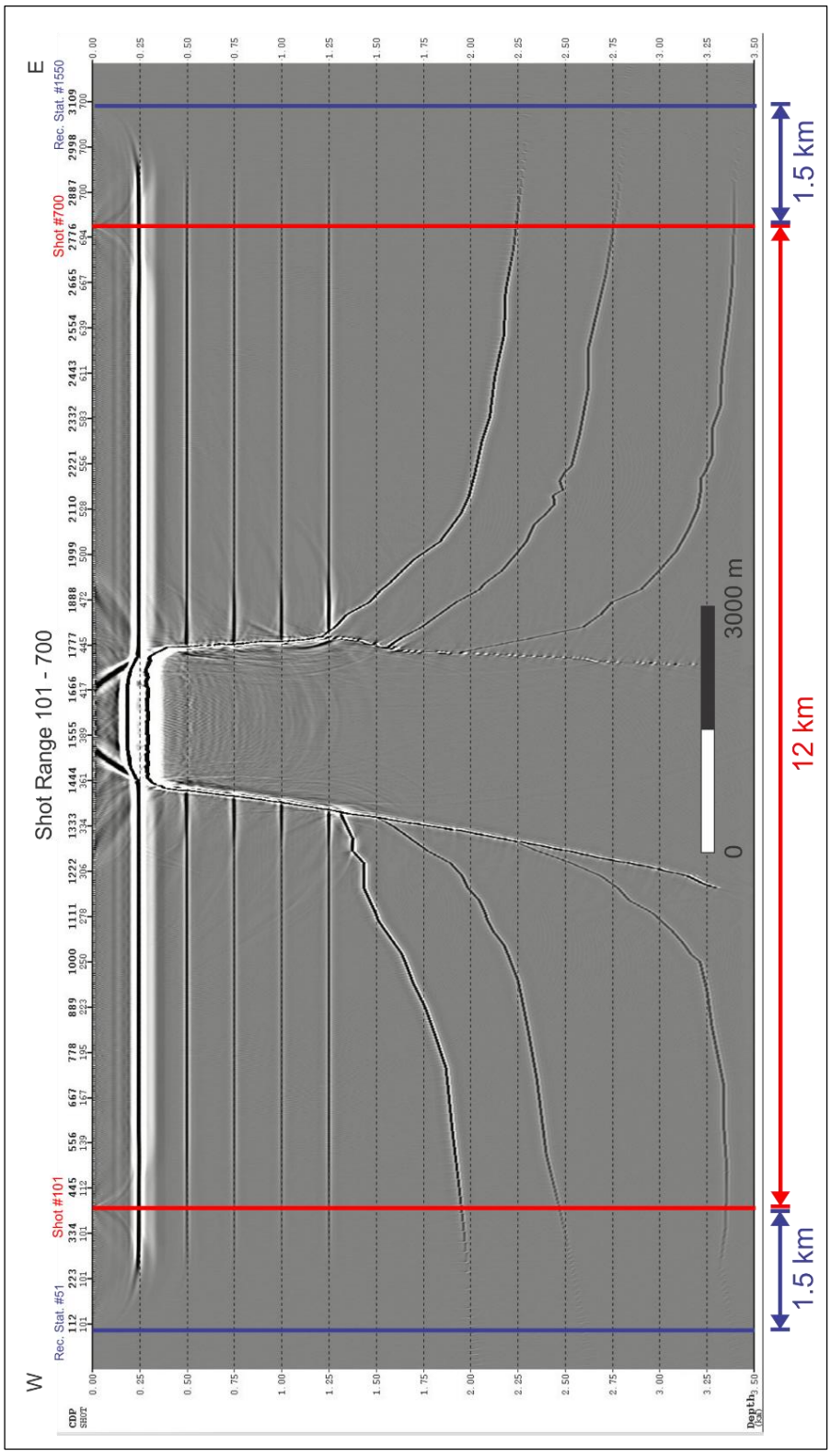

Figure 3.39. RTM image that is modeled with 101-700 shot range.

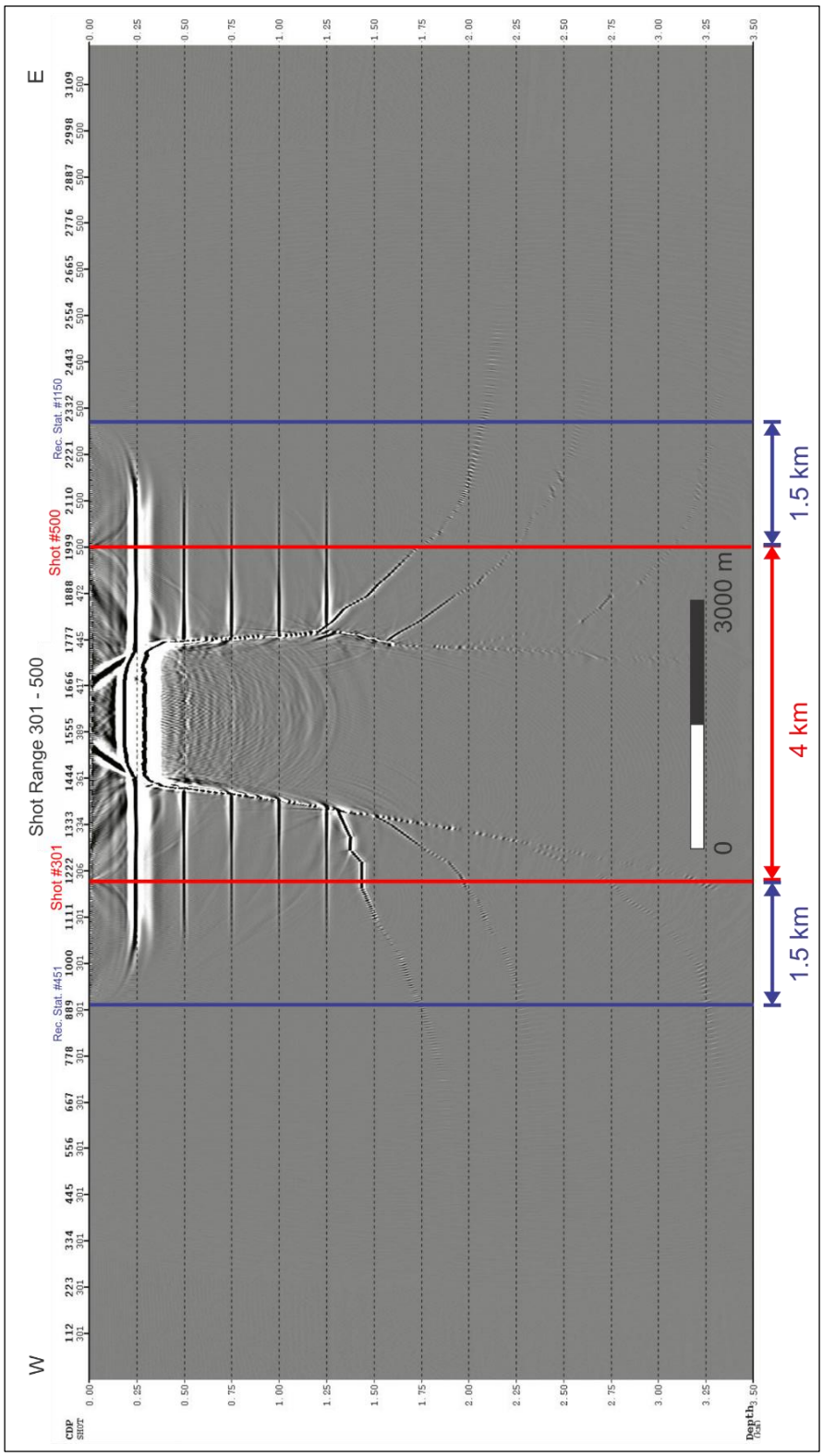

Figure 3.40. RTM image that is modeled with 301-500 shot range.

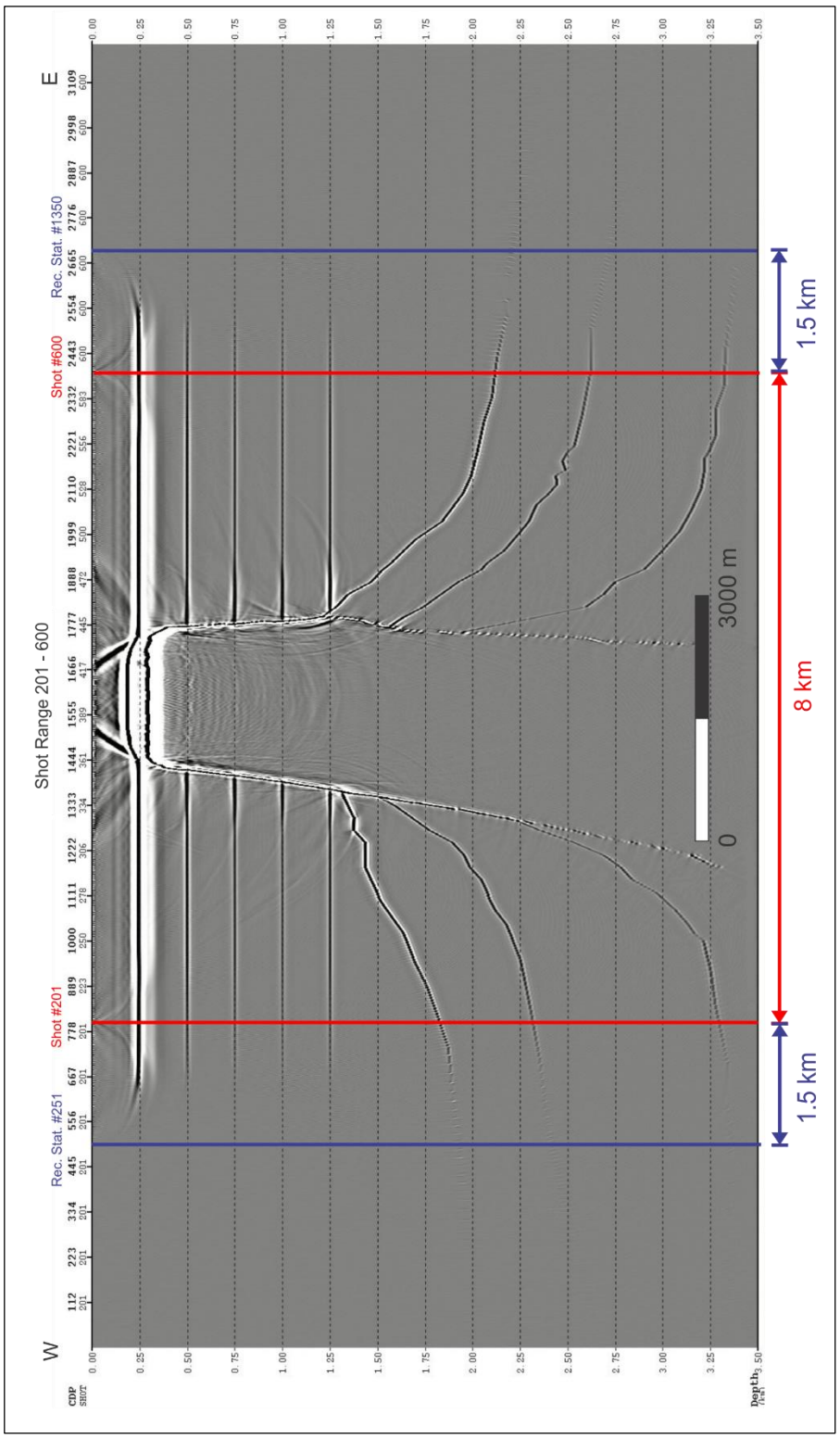

Figure 3.41. RTM image that is modeled with 201-600 shot range.

3.2.4 Analyses of the 2-D Survey with Optimum Parameters

The new survey designed with RTM imaging was analyzed in terms of fold, resolution, illumination, and offset distribution. Final parameters of the new survey is given by Table 3.3.

Table 3.3 Acquisition parameters of new 2-D seismic survey.

Number of Receiver Stations	550	**Number of Shots**	200
Number of Receivers	150	**Receiver Interval**	20 m
Shot Interval	40 m	**Shot line length**	8000 m
Receiver line length	11000 m	**Sampling rate**	1 ms
Recording length	4 s		

The maximum fold of the survey was calculated as 38. This fold value is very small when it is compared with the maximum fold of the actual survey. But, unlike the actual survey, the fold is consistent at that maximum value throughout the profile. For this reason, the data quality of new 2-D survey is expected to be better than the actual survey, since the fold is uniformly distributed. Survey geometry and fold distribution of the new survey is shown in Figure 3.42. As seen on trace count – offset histogram of the new survey, number of traces that fall into each offset bin is identical and higher than the actual survey as a result of rolling the receiver line with every shot along the profile (Figure 3.43).

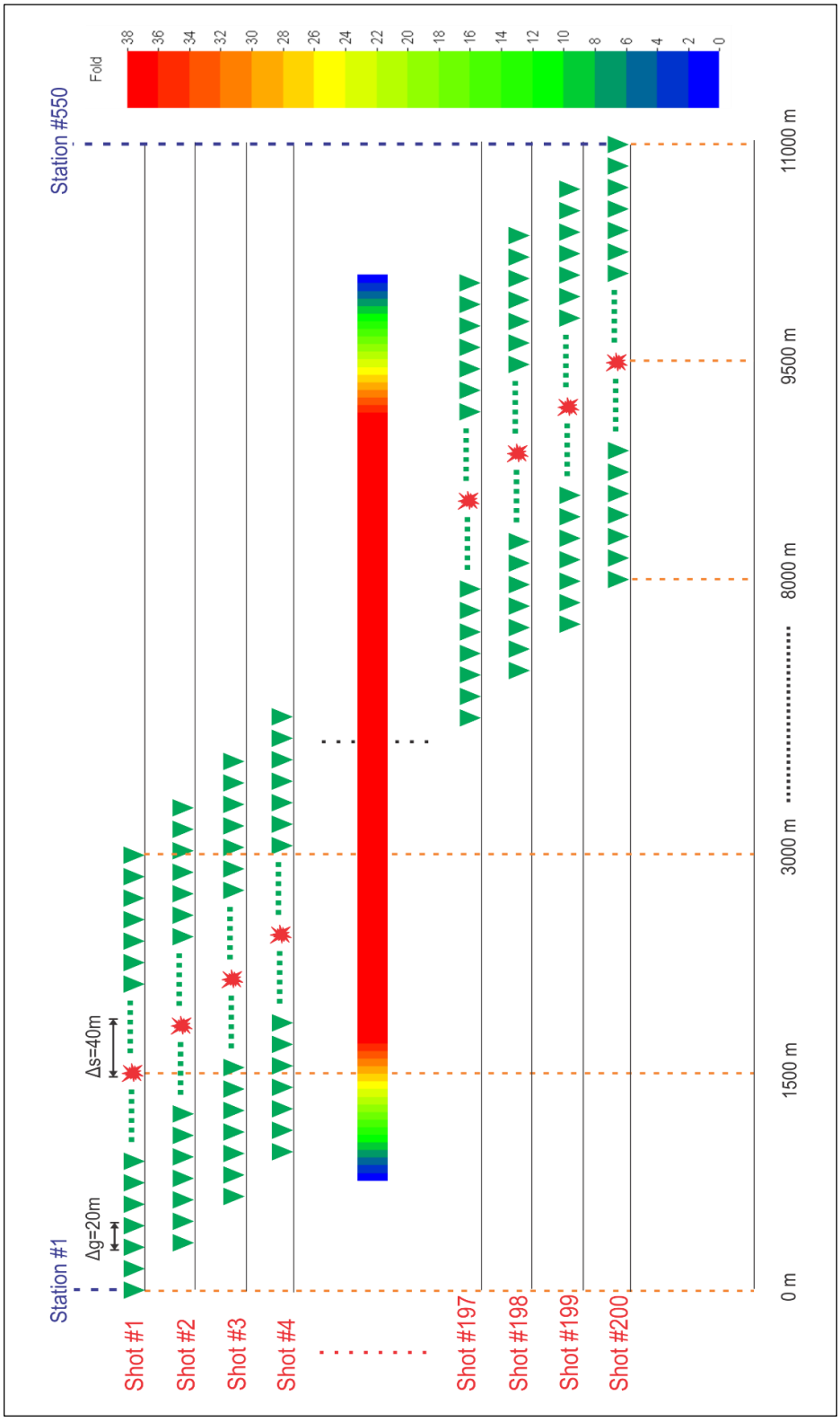

Figure 3.42 Survey geometry and fold distribution of the new 2-D survey.

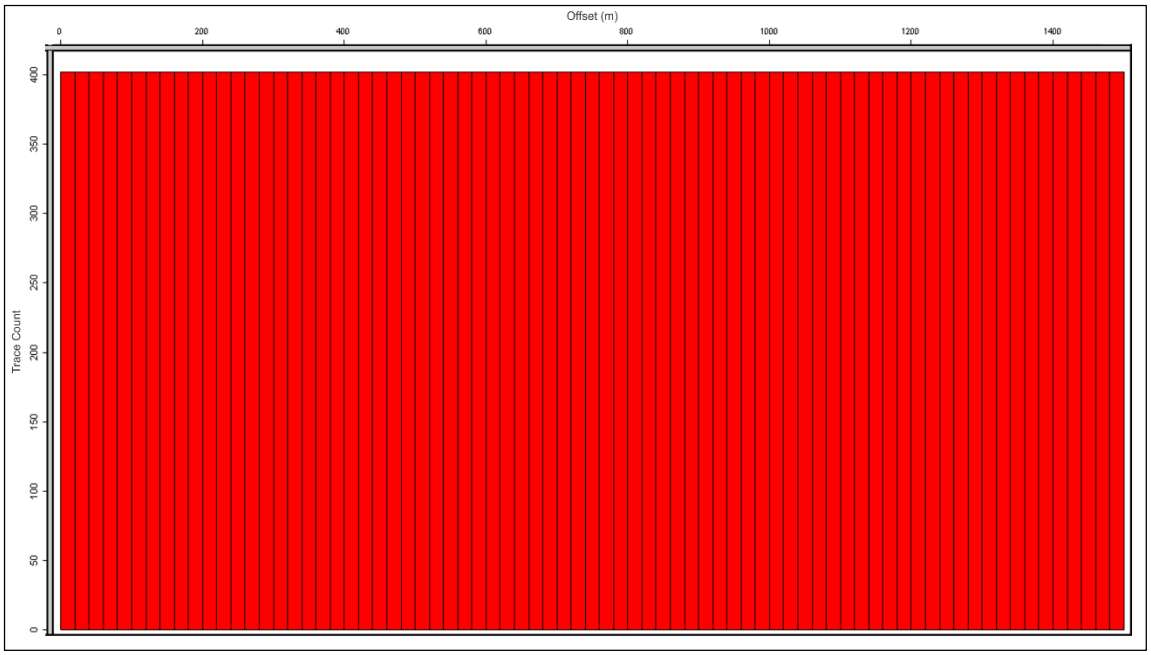

Figure 3.43 Trace count – Offset histogram of the new 2-D seismic survey. The chart shows the number of traces that fall each range of offset values.

3.3 3-D Seismic Survey Design via modeling and RTM imaging

3.3.1 Fundamentals of 3-D Seismic Survey Design

The basic concepts that are used for 2-D seismic surveys are used for 3-D seismic surveys as well. However, analyses of 3-D survey designs are more complicated, since the source and receiver arrays are not in-line like in 2-D surveys. Unlike the 2-D surveys, there are number of source and receiver lines in 3-D surveys. Also, the source and receiver lines in 3-D surveys are mostly distributed orthogonal to each other; therefore, the source and receiver lines must be defined in 3-D separately.

The source and receiver layouts may be designed in different patterns, such as circles, checkerboards, stars etc. Every geometry is analyzed in terms of different concepts to find

the best one that suits the survey objectives. Note that the survey design analyses are used to reach the survey objectives with optimum survey cost.

The surface coverage in 2-D designs is defined by common-depth-points (CDPs). On the other hand, the surface coverage of 3-D designs is described with square or rectangular areas called bins. Spatial resolution of data sampling is dependent to the bin size decided for the survey (Stone, 1994). The importance of the bin size selection will be highlighted in 3-D survey design concepts. Also, most of the concepts in 2-D design are altered with the bin concept since they are transferred in to three dimensions.

The definitions of basic concepts in 3-D survey design will be presented in an orthogonal geometry the most common geometry for onshore 3-D seismic surveys. In this geometry, the receiver and source lines are laid out at right or normal angles to each other as shown in Figure 3.44.

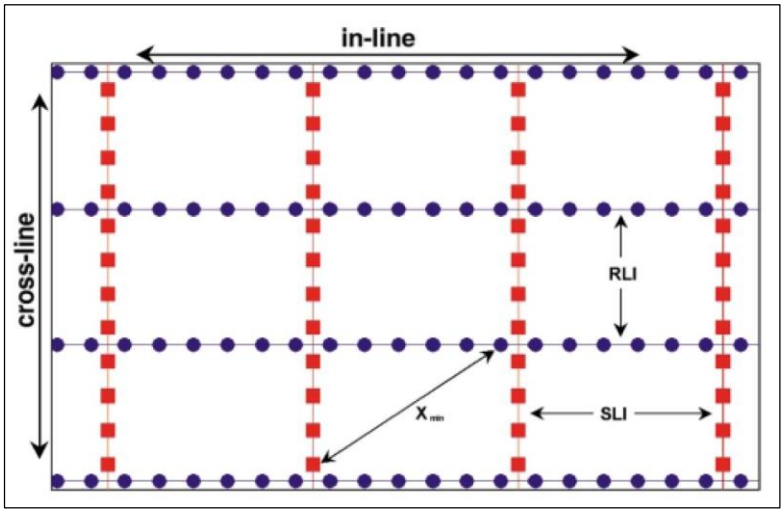

Figure 3.44 Elements of orthogonal geometry. Red squares and blue circles represent the source and receiver locations, respectively (modified after Cordsen et al., 2000).

3.3.1.1 Fold in 3-D

As mentioned before, fold is one of the parameters that affects the signal-to-noise ratio. Fold and signal-to-noise ratio relationship is expressed by Cordsen (2000) in Figure 3.45. In 3-D case, fold is defined by number of stacked traces in a bin, which are from different sources and receivers having the same midpoint reflection. Relationship between 2-D and 3-D fold is basically explained with frequency dependency by Krey (1987) using the following equation (Eq. 3.12).

$$\boldsymbol{F_{3D} = F_{2D} \times f \times c} \qquad \text{(Eq. 3.12)}$$

where;

f = expected frequency,

c = arbitrary constant.

A more complete approach of Krey for the relationship between 2-D and 3-D fold including CDP spacing, frequency, and average interval velocity is expressed Eq. 3.13.

$$\boldsymbol{F_{3D} = \frac{F_{2D} \times (bin_{3D})^2 \times f \times \pi \times 0.401}{CDP_{2D} \times V}} \qquad \text{(Eq. 3.13)}$$

where;

F_{2D} = fold in 2-D,

bin_{3D} = 3-D bin spacing,

f = frequency,

CDP_{2D} = 2-D CDP spacing, and V= velocity.

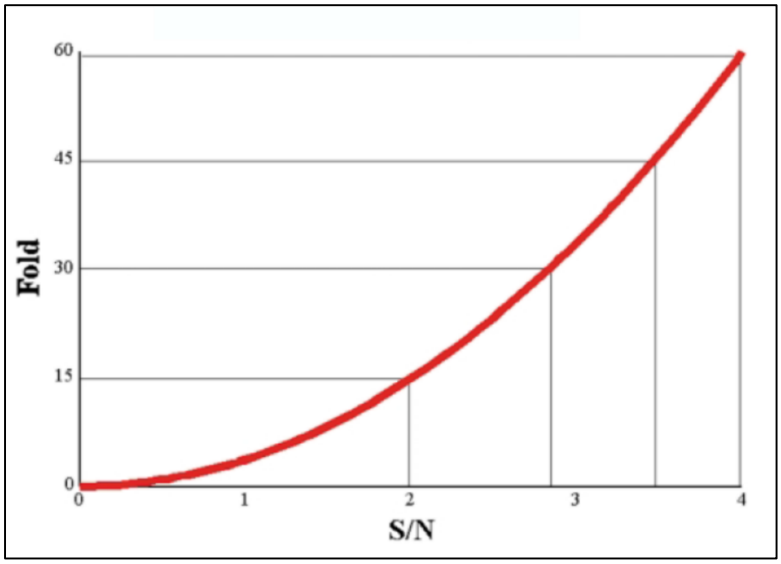

Figure 3.45. Fold versus signal-to-noise ratio (S/N), after Cordsen (2000).

Calculation of the average 3-D fold can be obtained using the equation given above. One who wants to calculate the fold in detail should examine the in-line and cross-line components of the fold. The total fold of the survey is calculated combining the in-line and cross-line folds. The full stacking fold is defined by the maximum in-line and cross-line offsets along with the receiver and source line intervals. The station spacing influences fold indirectly since it modifies the bin size, the source density, and the number of channels required. Also, required number of channels can be calculated if fold, bin size, source station, and line intervals are determined based on Eq. 3.14.

$$\boldsymbol{NC = F_{3D} \times dx_{SL} \times dx_S \times B^2} \qquad \text{(Eq. 3.14)}$$

where;

F_{3D} = fold in 3-D,

dx_{SL} = source line interval,

dx_S =source interval,

B = bin dimension for square bins (Cordsen et al, 2000).

3.3.1.2 Bin Size

For 3-D data, the bin concept is the main building block throughout the survey. The shape of the bin is usually selected as a rectangle or square (Stone, 1994). Rectangular bins are preferred when the required lateral resolution in one direction is different than the required resolution of the other direction (Cordsen et al., 2000). Otherwise, square bins are popular for obtaining adequate spatial sampling in both dimensions.

According to Cordsen et al. (2000), the S/N is directly proportional to the length of one side of the bin for square bins (Figure 3.46). The fold is a quadratic function of the length of one side of the bin.

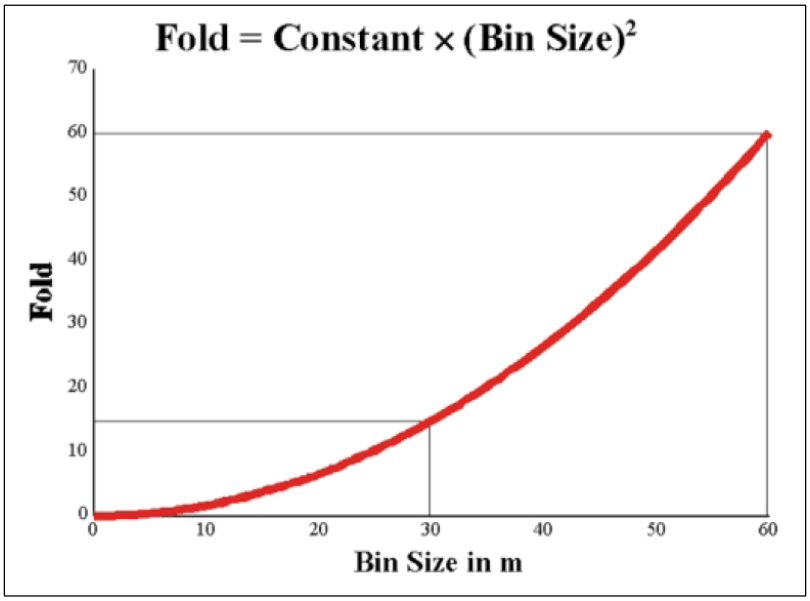

Figure 3.46. Fold versus bin size (after Cordsen et al., 2000).

The bin size is determined based on the target size, maximum un-aliased frequency due to dip, and lateral resolution analyses. These analyses can provide different bin size values. Budget of the survey is another factor determining the bin size proposed by different analyses.

The bin size of a survey using the target size is expressed in Eq. 3.17 as proposed by Cordsen et al. (2000).

$$\boldsymbol{Bin\ size} \leq \frac{\boldsymbol{Target\ size}}{\mathbf{3}} \qquad \text{(Eq. 3.17)}$$

Existence of dipping layers in the survey area is also an important factor for determining the bin size. The maximum possible un-aliased frequency before migration is related to the velocity of the target, the value of the geological dip, and the bin size. Different bin sizes can be obtained using maximum frequency – dip angle, and dip angle – bin tables. The equation for calculating the bin size for alias frequency is given in Eq. 3.18.

$$\boldsymbol{Bin\ Size} = \frac{\boldsymbol{V_{int}}}{\mathbf{4}\times\boldsymbol{f_{max}}\times\mathbf{sin}\,\boldsymbol{\theta}} \qquad \text{(Eq. 3.18)}$$

Many publication have recommended different definitions and equations for lateral resolution, such as Clearbout (1985), Embree (1985), Freeland and Hogg (1990), Ebrom et al. (1995), and finally Vermeer (1998). Cordsen et al. (2000) suggested Vermeer's equation to simply calculate the bin size assuming that lateral resolution can be between one quarter and one half the dominant wavelength (Eq. 3.19).

$$\boldsymbol{Bin\ Size} = \frac{\boldsymbol{V_{int}}}{\boldsymbol{N \times f_{dom}}} \quad \text{(Eq. 3.19)}$$

where;

V_{int} = interval velocity,

f_{dom} = dominant frequency,

N varies from 2 to 4.

Note that calculated resolution is always better than actual resolution since there will be resolution loss due to noise.

All bin size analyses give the maximum bin size to achieve minimum acceptable resolution on target. The bin size should be adjusted according to budget of the seismic survey.

3.3.1.3 Minimum Offset (X_{min})

The largest minimum offset is the diagonal of the box described with coincident source and receiver stations at corners (Figure 3.47). The receiver and source line intervals directly control the X_{min} value in many designs, such as orthogonal, brick, and zigzag designs (Cordsen et al., 2000). X_{min} can be calculated using Eq. 3.20.

$$\boldsymbol{X_{min}} = \sqrt{(\boldsymbol{RLI})^2 + (\boldsymbol{SLI})^2} \quad \text{(Eq. 3.20)}$$

Having small X_{min} is important in order to sample the shallowest reflector wanted to be mapped in three dimensions. According to Vermeer (1999), at least four-fold multiplicity is necessary to have enough confidence in a correct interpretation at a shallow horizon.

The four-fold formula for symmetric sampling at mute distance X_{sh} is defined using Eq. 3.21.

$$\boldsymbol{X_{sh} = RLI \times 2 \times \sqrt{2} = 2 \times X_{min}} \quad \text{(Eq. 3.21)}$$

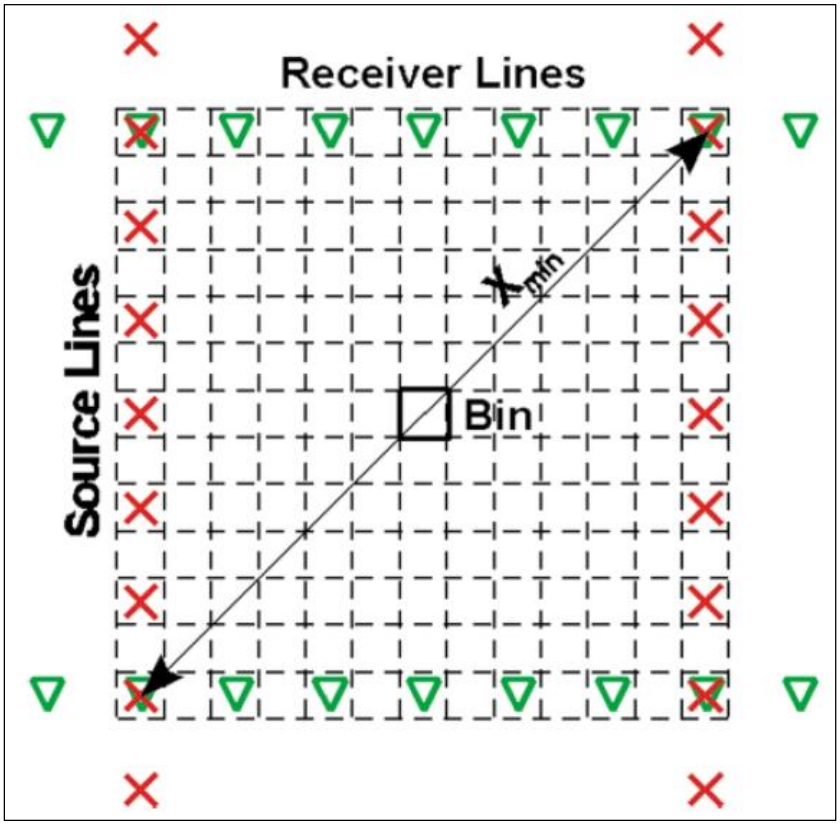

Figure 3.47. X_{min} definition with coincident source and receiver stations at corners of box (Cordsen et al, 2000).

3.3.1.4 Maximum Offset (X_{max})

An adequate maximum offset selection is needed to record the traces coming from deeper horizons. The maximum recorded offsets are affected by the processing mute of the far offsets as well. Muting the traces within the bin will decrease the fold coverage of

related bin. So, the X_{max} should be determined very well to keep the fold value stable. The fold within a circle of radius R is defined by Eq. 3.22.

$$\boldsymbol{Fold} = \frac{(\boldsymbol{SD}\times\boldsymbol{NC}\times\boldsymbol{B^2})}{\boldsymbol{Patch\ Size}} \qquad \text{(Eq.3.22)}$$

As shown in Figure 3.48, R represents the X_{max} and it is always advantageous to determine the X_{max} along the diagonal of the patch. If X_{max} is determined as the in-line maximum offset, some traces will be muted; otherwise, all traces will be used in the stack. Also using diagonal measurement will give a uniform offset distribution (Cordsen, 1995).

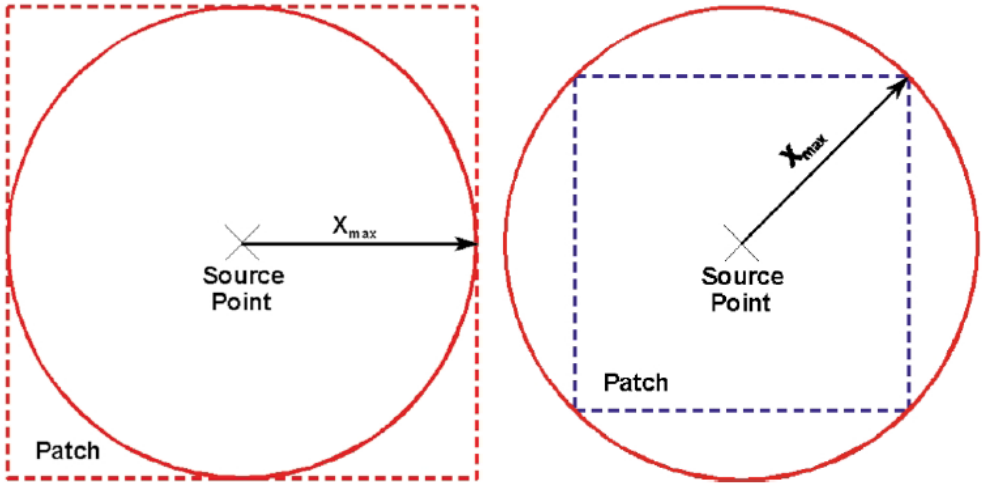

Figure 3.48. Definition of X_{max} two different approaches. In-line maximum offset (left) and diagonal maximum offset (right), after Cordsen et al. (2000).

Another approach to determine the X_{max} is to trace the rays on geological models. Conversion of reflected energy to refracted energy can be examined for each event in the model. Then suitable X_{min} and X_{max} values can be determined for entire model.

3.3.1.5 Offset Distribution

Each CMP bin stores many midpoints associated with different offsets and azimuths from the source to the receiver. The offset distribution is directly related to the fold. Higher folds always show better offset distribution. The main goal for a designer is obtaining a good mix of far and near offsets for each CMP bin.

3.3.1.6 Azimuth Distribution

Like the offset distribution, the azimuth distribution is also controlled by the fold. A good azimuth distribution allows to record the data having azimuth-dependent variations, such as anisotropy and/or dipping. The general rule to achieve a good azimuth distribution is keeping the aspect ratio between 0.6 and 1.0.

3.3.1.7 Recording Time

The minimum recording time for 2-D surveys is already explained in previous sections. The vertical travel time calculation will not be sufficient to record the diffractions from the deepest event in 3-D survey. Additionally, dip requirements, static shifts, multiples, and NMO reflections should also be considered. According to Margrave (1997), the minimum recording length should be calculated as follows (Eq. 3.23):

$$\boldsymbol{t = \frac{2Z}{V \cos \theta}} \qquad \text{(Eq. 3.23)}$$

3.3.1.8 Ray Trace Modeling

The ray trace modelling is one of the most useful methods to test the acquisition parameters so as to build an accurate geological model. Areas with complex geology, such as salt domes, faults, steeply dipping layers, and lateral velocity discontinuities, can be analyzed in terms of illumination by ray tracing. Using ray tracing method allows detection of the areas where illumination is required. Then, receiver and/or source intervals may be updated according to the imaging needs of the model (Neff and Rigdon, 1994).

3.3.2 3-D Seismic Survey Design using RTM Cases

The optimum parameter considerations and observations of the 2-D survey design in previous chapter provide an insight for determining the best 3-D design. However, there are some parameters not applicable in 2-D to be determined for 3-D survey design, such as survey geometry, regularity, offset and azimuth distributions, and fold in 3-D. In this section, the parameters determined using RTM images in 2-D will be modified for a 3-D seismic survey. Therefore, optimum survey parameters to image the salt structure in 3-D will be obtained.

3.3.2.1 Survey Geometry

There are many survey geometries that can be applied to 3-D surveys, such as swath, orthogonal, brick, non-orthogonal, zig-zag, and star. Each geometry has advantages over one another according to objectives of the surveys. Considering the popular geometries of 3-D survey, orthogonal geometry is more advantageous for this study. In terms of cost

effectiveness, orthogonal geometry is superior to parallel (swath) geometry. On the other hand, zig-zag geometry is more economic in open areas, such as deserts. All the other geometries usually do not provide desirable resolution and spatial continuity (Vermeer, 2002). Furthermore, survey and recording crews can make arrangements easily for deploying the equipment ahead of shooting and roll-along operation in orthogonal geometry (Cordsen et al., 2000). Therefore, considering these advantages orthogonal geometry was chosen to be used in this study.

3.3.2.2 Dimensions of the Survey Area

The size of the survey area was determined by reviewing the 2-D survey parameters. Therefore, 8 km by 8 km square survey area was considered adequate for imaging the salt structure and surroundings, since the salt model is in the center, circular, and there is no rooting to any direction.

Distances between the source and receiver lines determine the largest minimum offset (X_{min}) important to record shallow events. The source and receiver line intervals were selected as 250 m. Hence, X_{min} of the survey was calculated as 327 m small enough to sample shallow reflectors adequately. As a result, 33 in-lines and 33 cross-lines were distributed over the survey area with equal intervals (Figure 3.49).

3.3.2.3 Patch (Template) Description

The patch is defined as distribution of the active receivers that corresponds to one shot point in the survey. It is moved after each salvo along the survey and the survey area is

covered by the overlapping patches. Patch can be rolled along in-line or cross-line directions (Chaouch and Mari, 2006). The number of active receivers, group and shot intervals, in-line and cross-line intervals, and maximum offset should be described so as to define the patch of the survey.

In 3-D surveys, shot and group intervals are usually selected coarser than intervals in 2-D surveys to decrease the cost of the survey. On the other hand, intervals should be decided appropriately to resolve structural dips and to ensure the imaging needs (Cordsen et al., 2000).

Although RTM images of 2-D survey showed that increasing the group and shot intervals is possible, choosing very large intervals can affect the imaging objectives. Therefore, group and shot intervals were slightly increased to 25 m and 50 m, respectively. Square CMP bin dimensions were determined as 12.5 m which is one half length of the group interval. The patch includes 3000 m-long 13 in-lines (receiver line) and 33 cross-lines (shot lines) to keep the aspect ratio at 1:1. Eventually, number of geophones required for such a survey was calculated as 1573. Table 3.4 summarizes the parameters of the patch used for the 3-D survey. Also, illustration of the parameters is shown in Figure 3.50.

Table 3.4. Table summarizing the 3-D acquisition parameters

Receiver line direction	E-W	**Source line direction**	N-S
Receiver interval	25 m	**Shot interval**	50 m
Receiver line interval	250 m	**Shot line interval**	250 m
Length of the receiver line	3000 m	**Length of the shot line**	3000 m
Number of channels	1560	**Number of Receivers per line**	121
Aspect ratio of the patch	1	**Number of shots**	10583
Shot Density (Source per km^2)	83	**Bin shape and size**	Square 12.5 m x 12.5 m

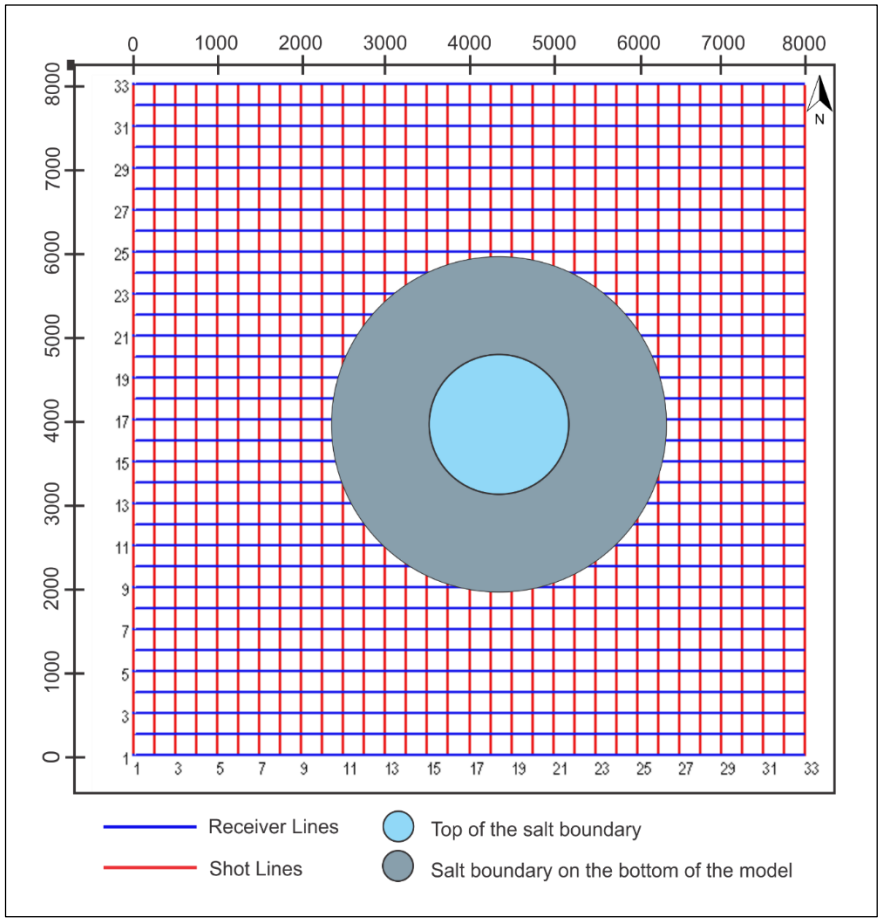

Figure 3.49. Designed 3-D survey area. Red and blue lines represent the shot and receiver lines, respectively. Boundary of the salt at the top and bottom of the model is shown by blue and grey circles, respectively.

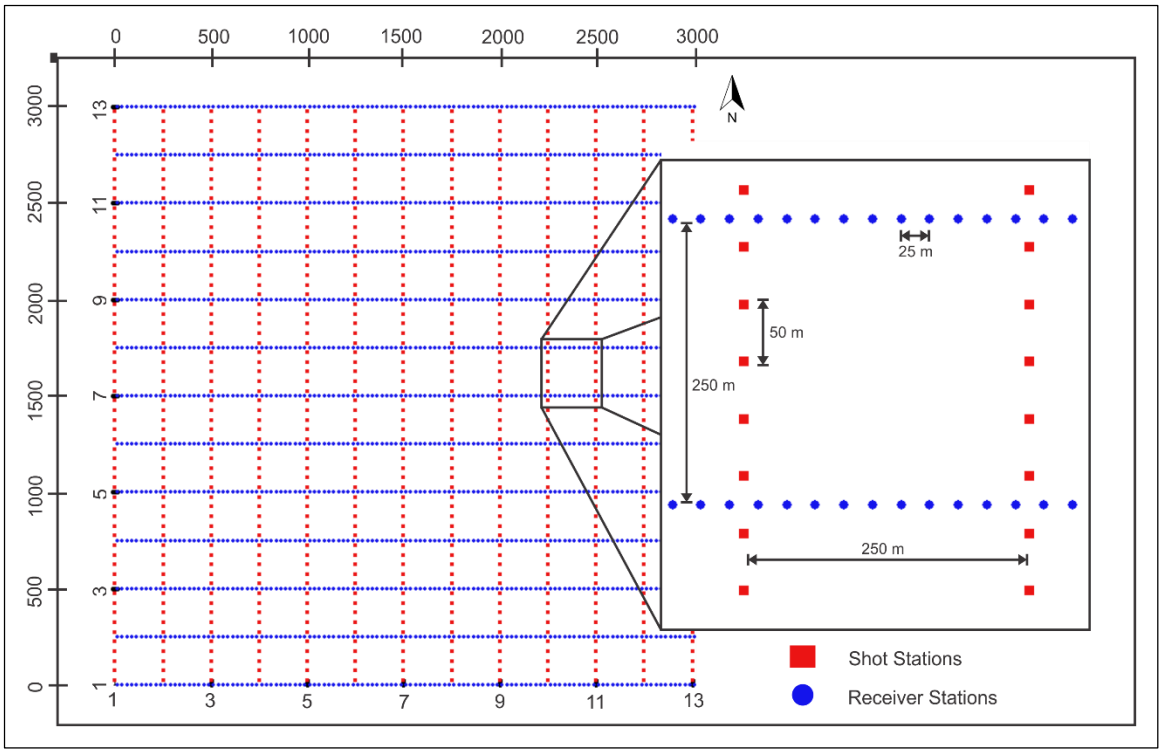

Figure 3.50. Definition of the 3-D patch. Red squares and blue circles represent the shot and receiver stations, respectively.

3.3.2.4 Analyses on 3-D survey with optimum parameters

Once the acquisition geometry and parameters were determined, the survey was analyzed based on the fold, offset and azimuth distribution, and shot contribution. The maximum total fold of 49 is uniformly distributed over the survey area. However, it is decreasing at the edges of the box, since the number of active receivers are decreased on the corners and edges of the survey area due to the shooting pattern. Figure 3.51 shows the number of receiver lines that have active stations for each shot. Nevertheless, 76.5% of the area is covered by the maximum fold appropriate to image the salt dome and surroundings. Also, even the fold values are less than the maximum at the sides of the

area, they have remarkable contribution to the data in the imaging process. The fold distribution of the survey is shown in Figure 3.52.

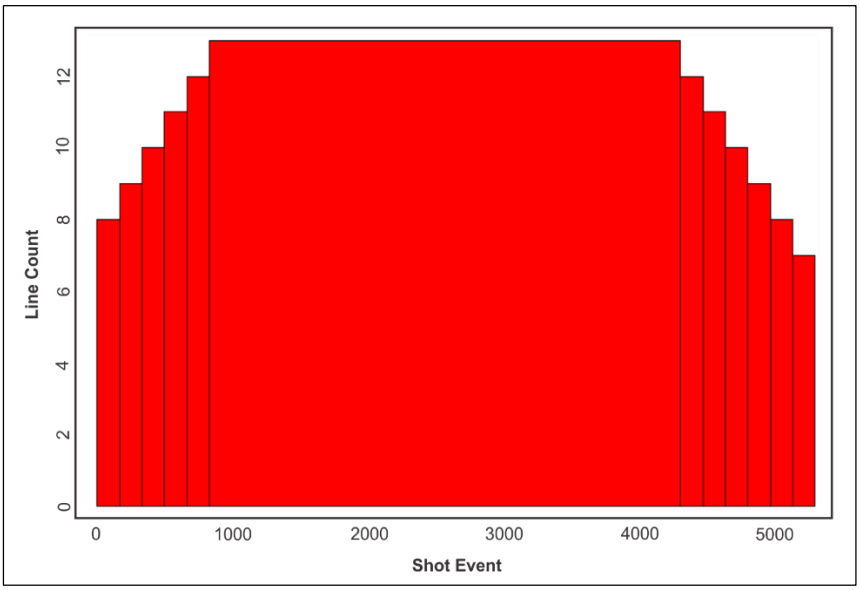

Figure 3.51. Line Count – Shot Event chart of 3-D survey. The chart shows how many receiver lines have active stations for each shot event.

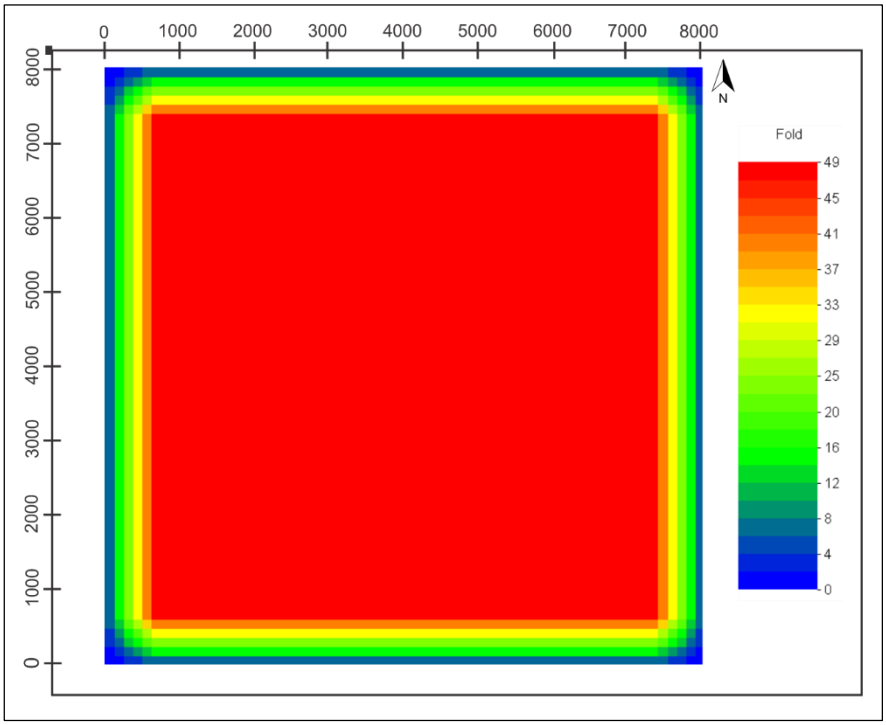

Figure 3.52. Fold distribution of the planned 3-D survey

The data acquired with poor offset distribution usually cause problems and limitations in processing and interpretation (Wright, 2003). It is always better to examine the fold distribution while designing the survey. In this study, the offset distribution of the designed survey was examined using Trace Count – Offset plot. As expected, a regular offset distribution was observed, since the aspect ratio of the patch is 1:1. As seen on Figure 3.53, the number of traces that fall in each bin of offset value is high enough to make valuable contribution to the final image.

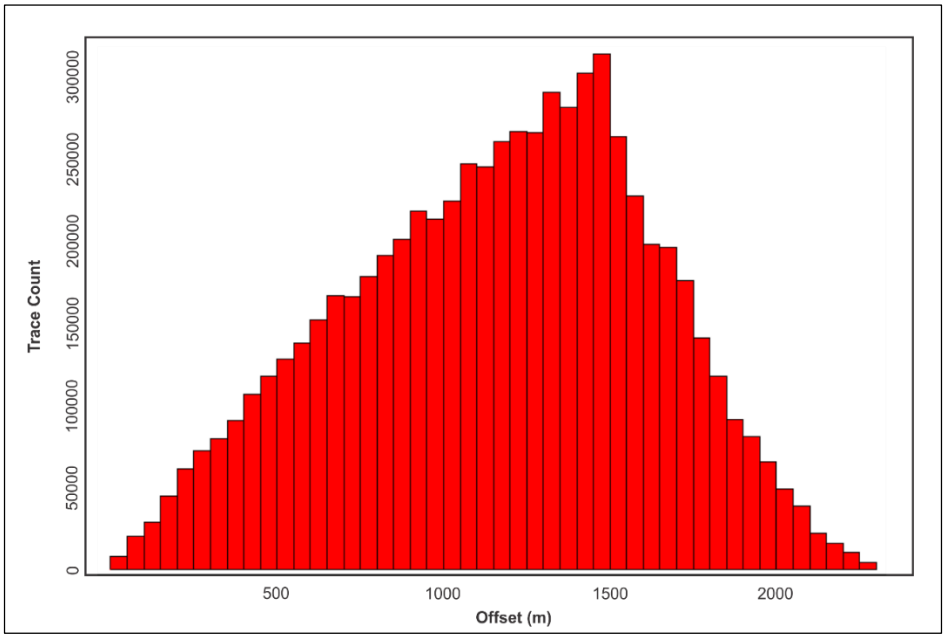

Figure 3.53. Trace Count – Offset plot of the planned 3-D survey.

Another important attribute that determines the data quality is the azimuth distribution. Each trace recorded from different azimuths stores valuable information about the subsurface structure in 3-D. Owing to the aspect ratio determined for the 3-D survey, uniform azimuth distribution was provided in order to image the target area adequately.

The Trace Count – Azimuth plot shows that the minimum number of traces that falls each azimuth bin is 90,000 (Figure 3.54). Moreover, the number of traces that falls 30°-60° and 120°-150° azimuth bins is higher than the average, as the missing traces on the corners and sides of the survey area provides poor azimuth distribution as a result of the shooting geometry. Even so, the average number of traces that falls each azimuth bin is acceptable to sample the data from every azimuth bin.

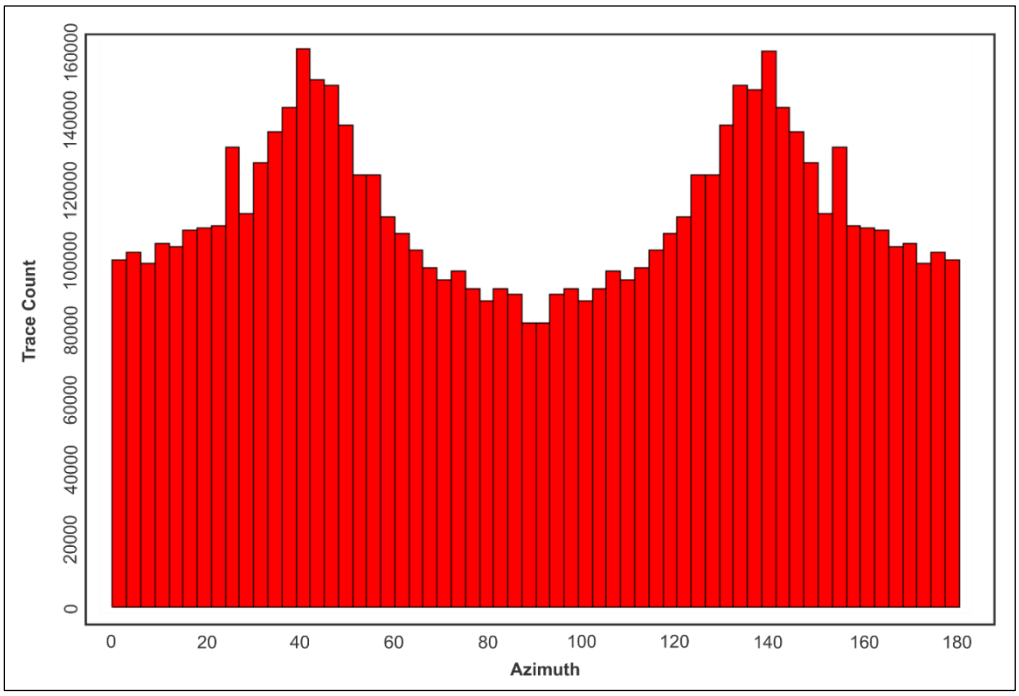

Figure 3.54. Trace Count – Azimuth plot of planned 3-D survey.

Both the azimuth and offset distributions can be examined using rose diagram. Rose diagram is colored by number of traces that fall in each sector defined by the offset and azimuth. The rose diagram of the planned survey is shown in Figure 3.55. As expected, the number of traces were increased with the larger offsets at every azimuth bin in the survey area.

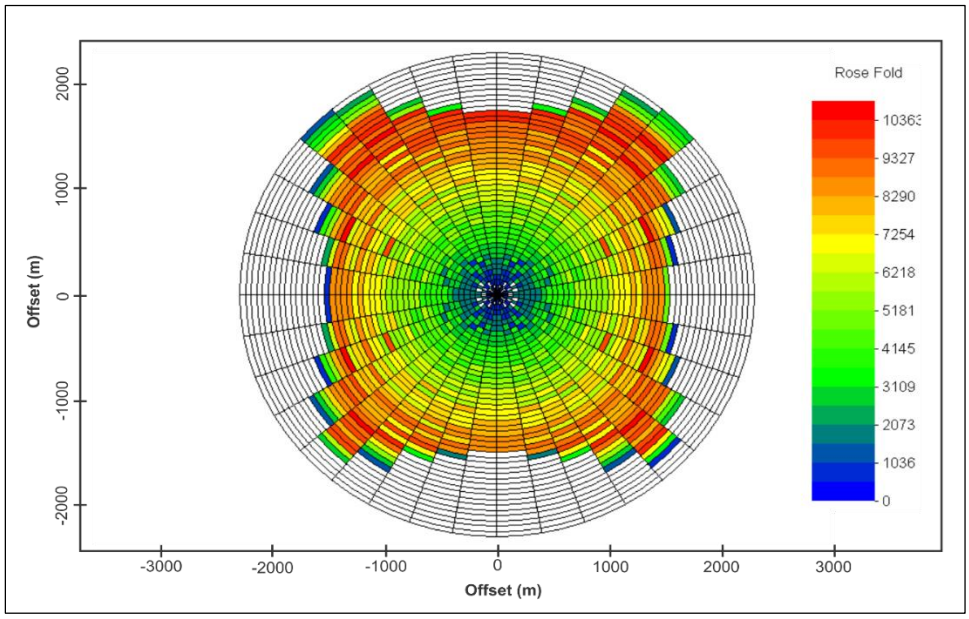

Figure 3.55. Rose diagram of the planned 3-D survey. Offset and azimuth sector steps are 50 m and 10°, respectively.

3.3.2.5 Pre-stack modeling and Imaging of 3-D seismic

The synthetic shot gathers of the designed 3-D seismic survey were modeled with finite difference method using full (two-way) acoustic wave equation. The pre-stack images of the data was produced with Reverse Time Migration (RTM). Before the shots gathers are modelled, CDP bins with 12.5 intervals were created over the velocity model. Therefore, CDP numbering ranges between 1 and 1279 in both in-line and cross-line directions. However, the survey area is limited between the 320th and 960th CDP numbers. The raw shot gathers created by finite difference method for the 2745th (shot at In-line CDP 486 – Cross-line CDP 420) and 4924th (shot at In-line CDP 618 – Cross-line CDP 440) shots are shown in Figure 3.56 and 3.57, respectively.

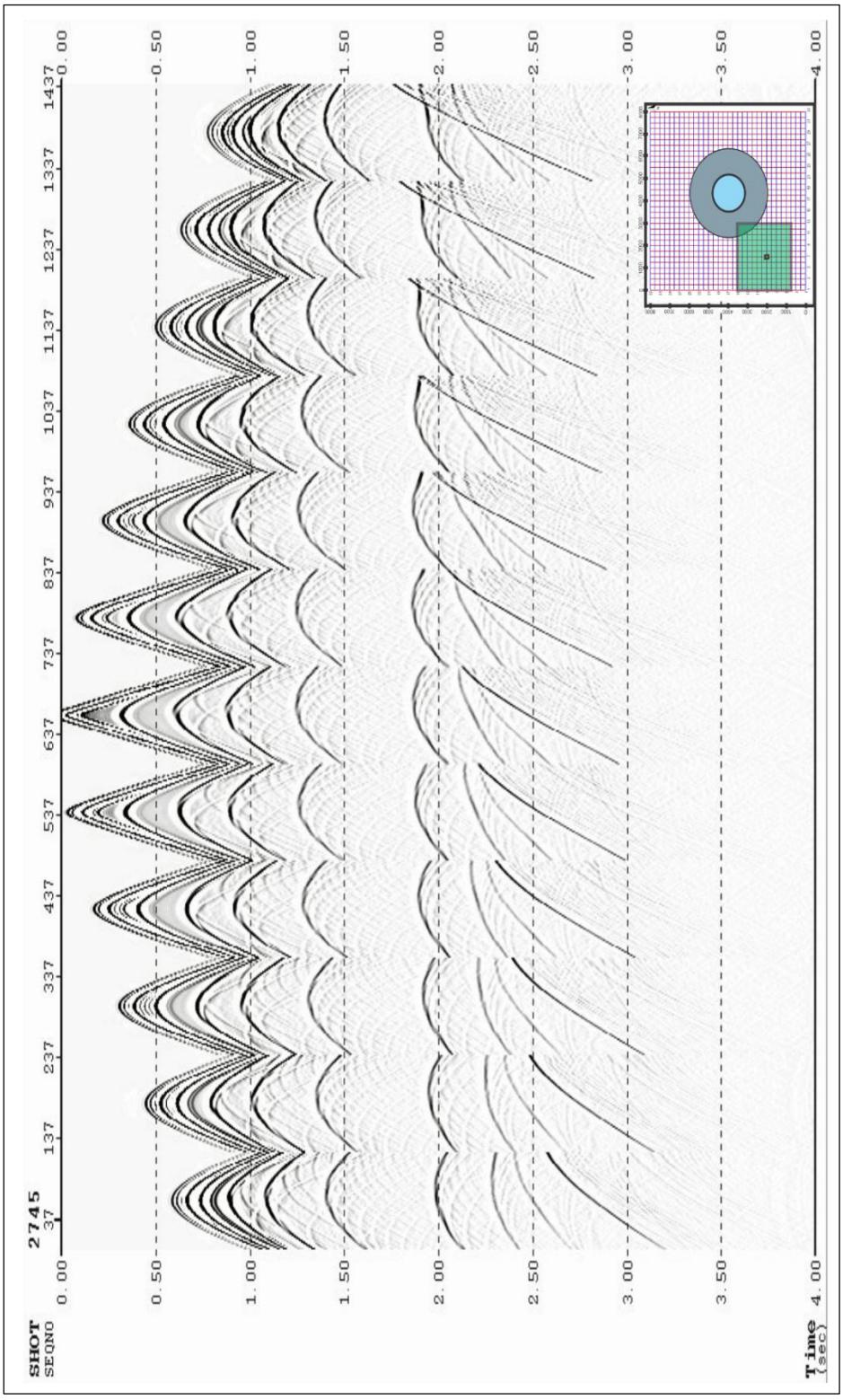

Figure 3.56. Raw shot gather of 2745th shot. The location of the shot and active channels associated with the shot are shown with yellow star and green square, respectively.

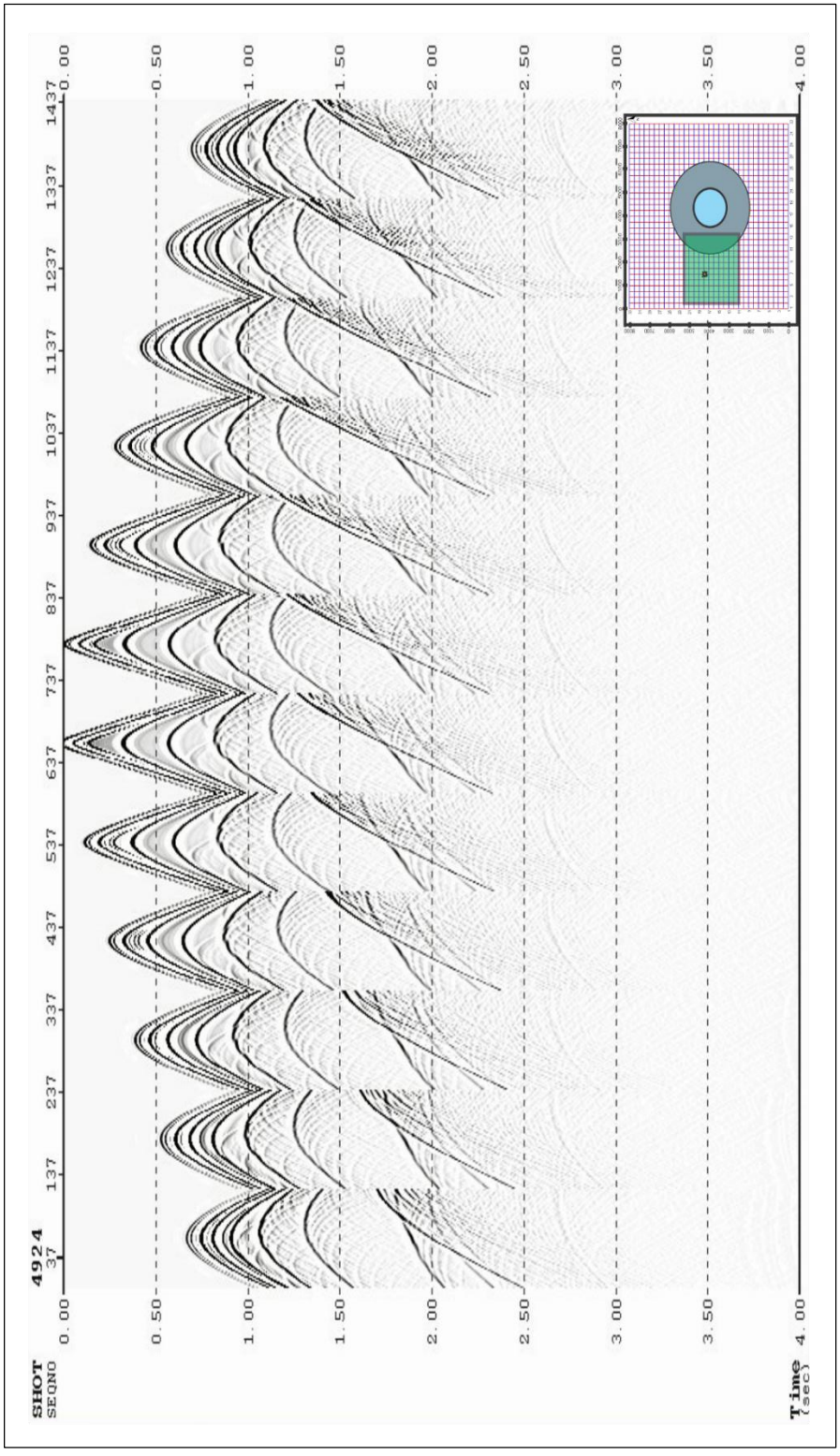

Figure 3.57. Raw shot gather of 2745th shot. The location of the shot and active channels associated with the shot are shown with yellow star and green square, respectively.

As observed in 2-D seismic imaging, especially shallow parts of the data contain low frequency noise caused by first breaks. Hence, the first breaks were filtered from each shot gather to increase the data quality. The RTM images of the synthetic 3-D data showed that the amplitudes of events are dramatically decreasing with increasing depth. Therefore, illumination of each shot was examined in order to be scaled with the raw RTM images. As a result, the amplitudes of the deeper events were normalized by scaling the RTM images with the illumination stack. The product of this process is shown in Figure 3.58.

After scaling with the illumination stack, the data were imaged with in-line, cross-line, and depth slices. As observed in in-line and cross-line images, the salt dome and surrounding sediments are adequately imaged with planned survey parameters (Figures 3.59-3.62). Also, the poorly built velocity model in 3-D has effects on the final RTM images. The stepped view of the horizons can be caused by coarse gridding, poor smoothing, or personal errors during modelling. Nevertheless, it can be counted as an advantage in order to test the survey design over the areas where faulting is also present.

Depth slices are very useful images for 3-D interpretation. The extension of the salt dome and location of the dipping horizons at exact depths can be observed by depth slices. The extension of the salt dome is symmetrical and circular at every depth range. But, the horizons are seen as asymmetric circles, since their dip angles are variable throughout the model. The RTM image slices from 408 m, 2460 m, and 3360 m are shown in Figures 3.63-3.65.

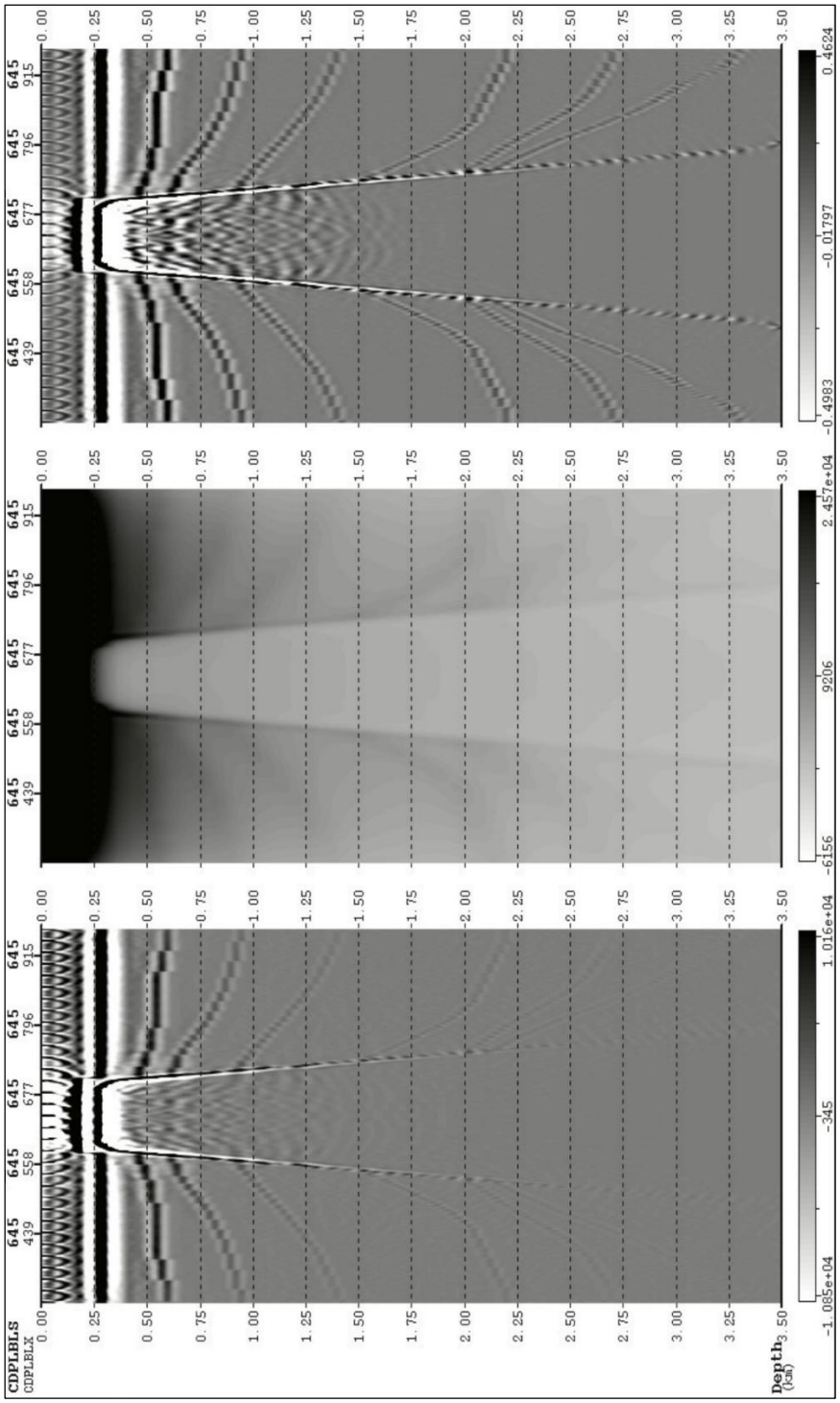

Figure 3.58. Process of scaling the RTM image with illumination stack. The raw RTM image (left), illumination stack (middle), and RTM image scaled with illumination stack (right) of inline 645 cross section.

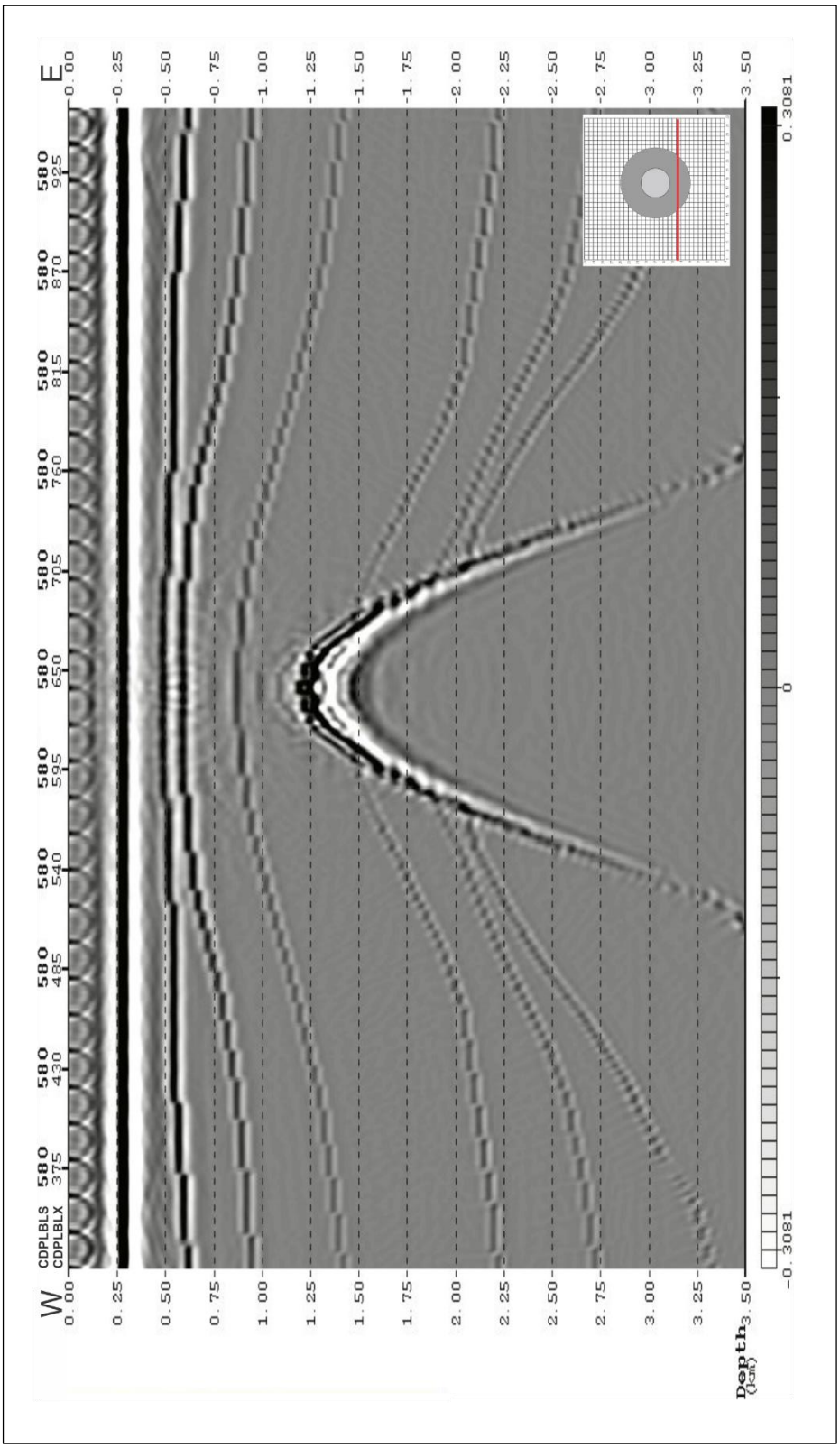

Figure 3.59. RTM image of in-line 580th cross section.

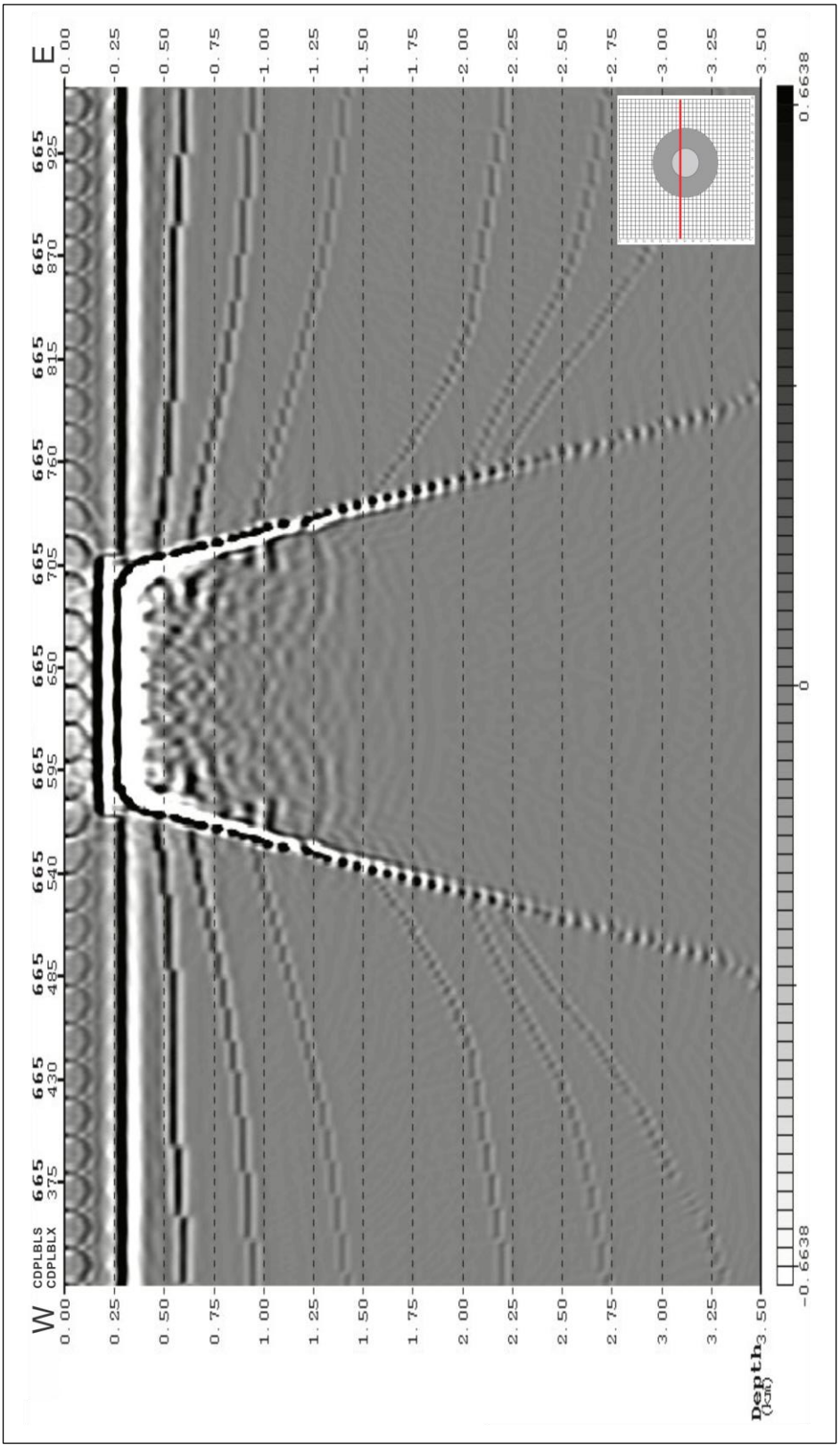

Figure 3.60. RTM image of in-line 665th cross section

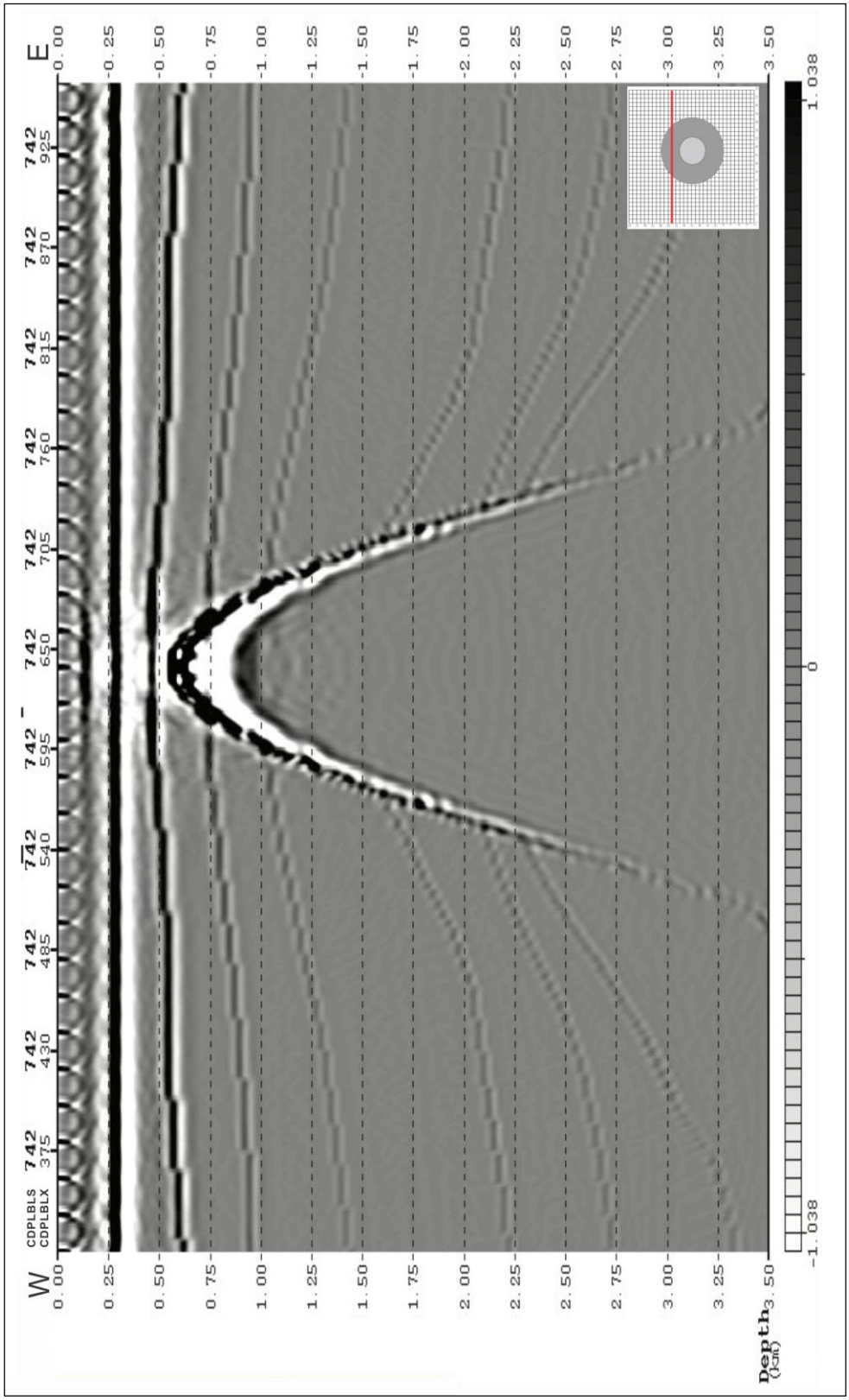

Figure 3.61. RTM image of in-line 742nd cross section.

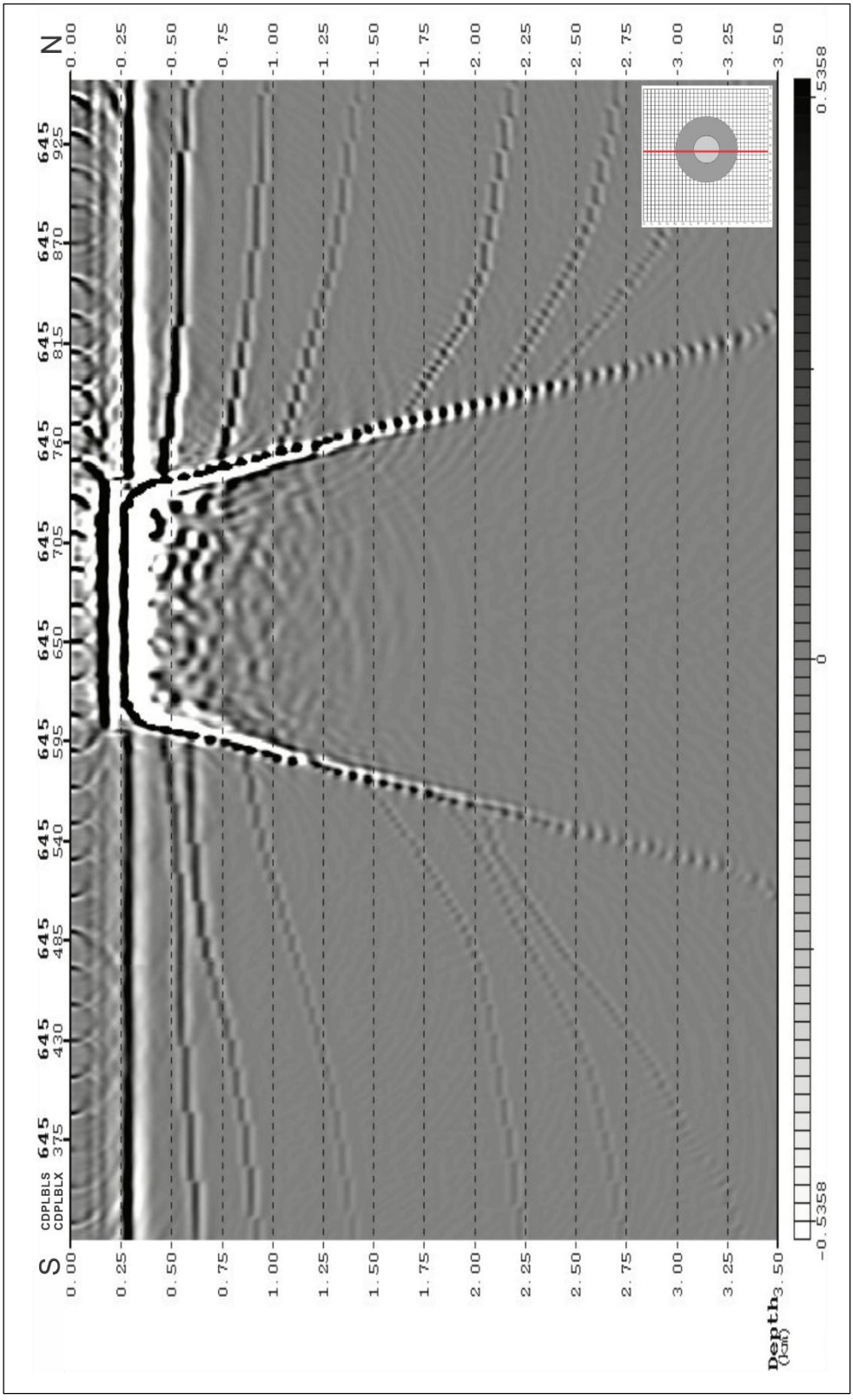

Figure 3.62. RTM image of cross-line 645th cross section

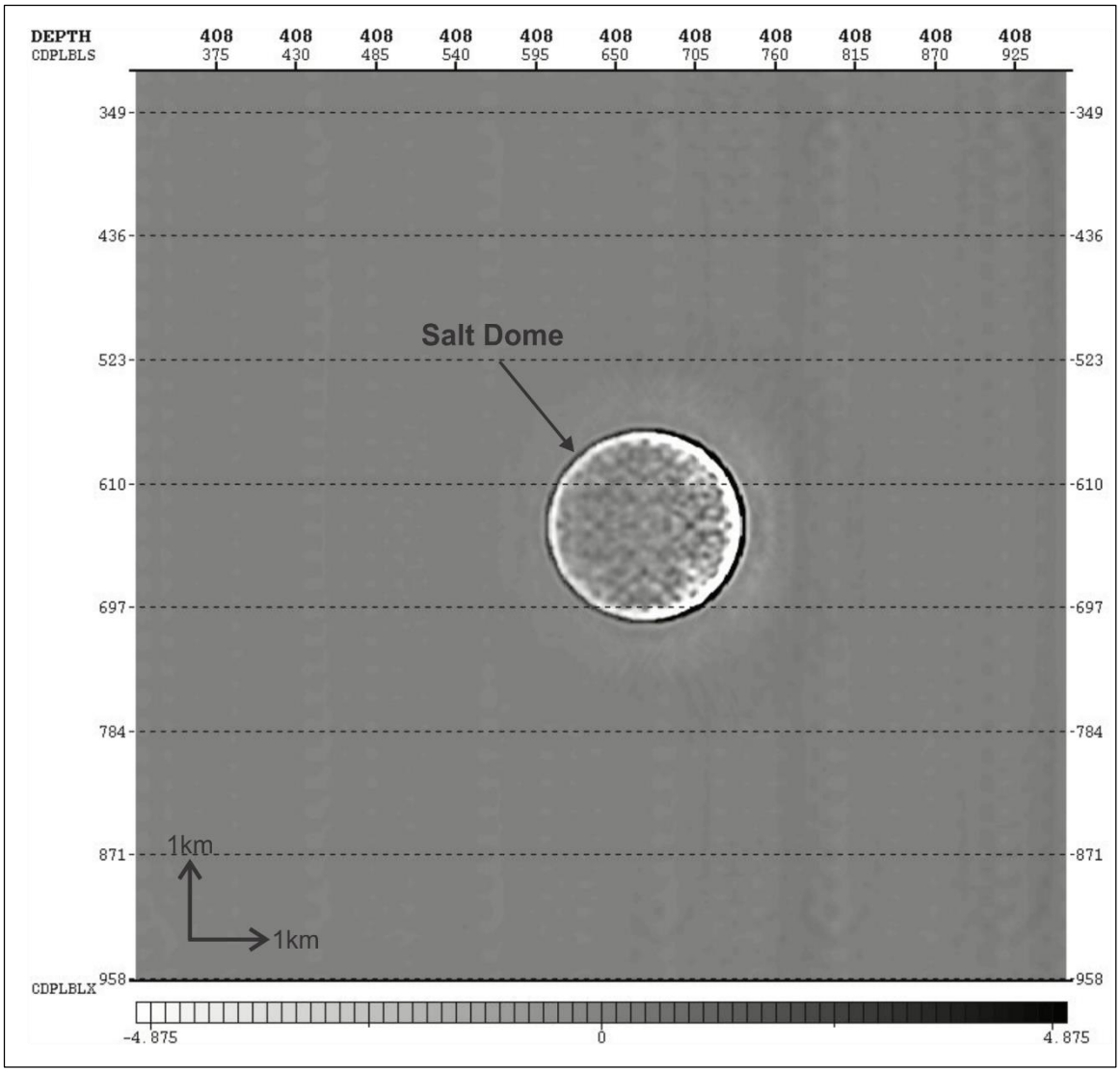

Figure 3.63. Depth slice image at 408 m. Circular reflection represents the boundary of the salt.

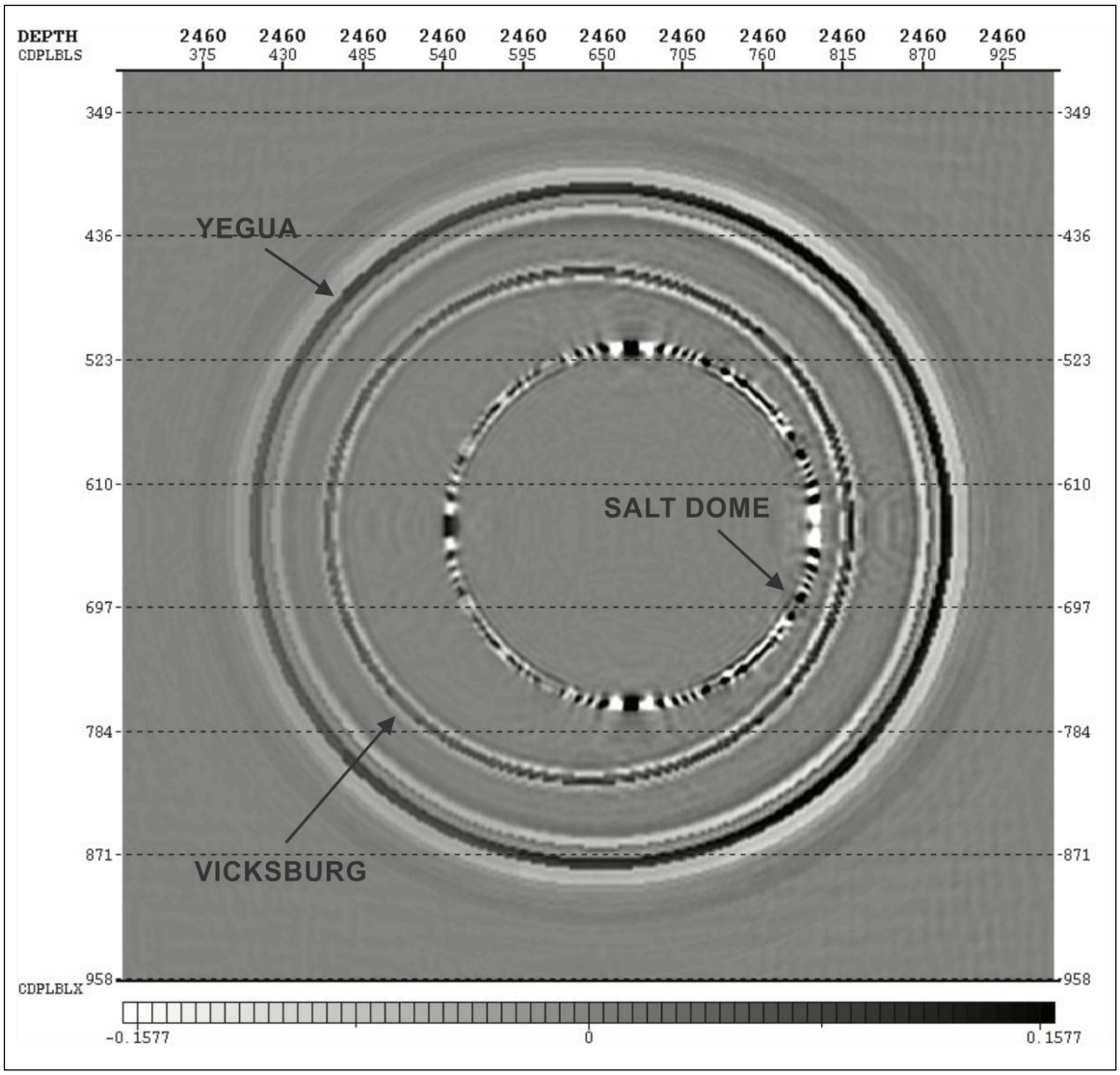

Figure 3.64. Depth slice image at 2460 m. Circular reflections represent the boundary of the salt, Vicksburg, and Yegua formations.

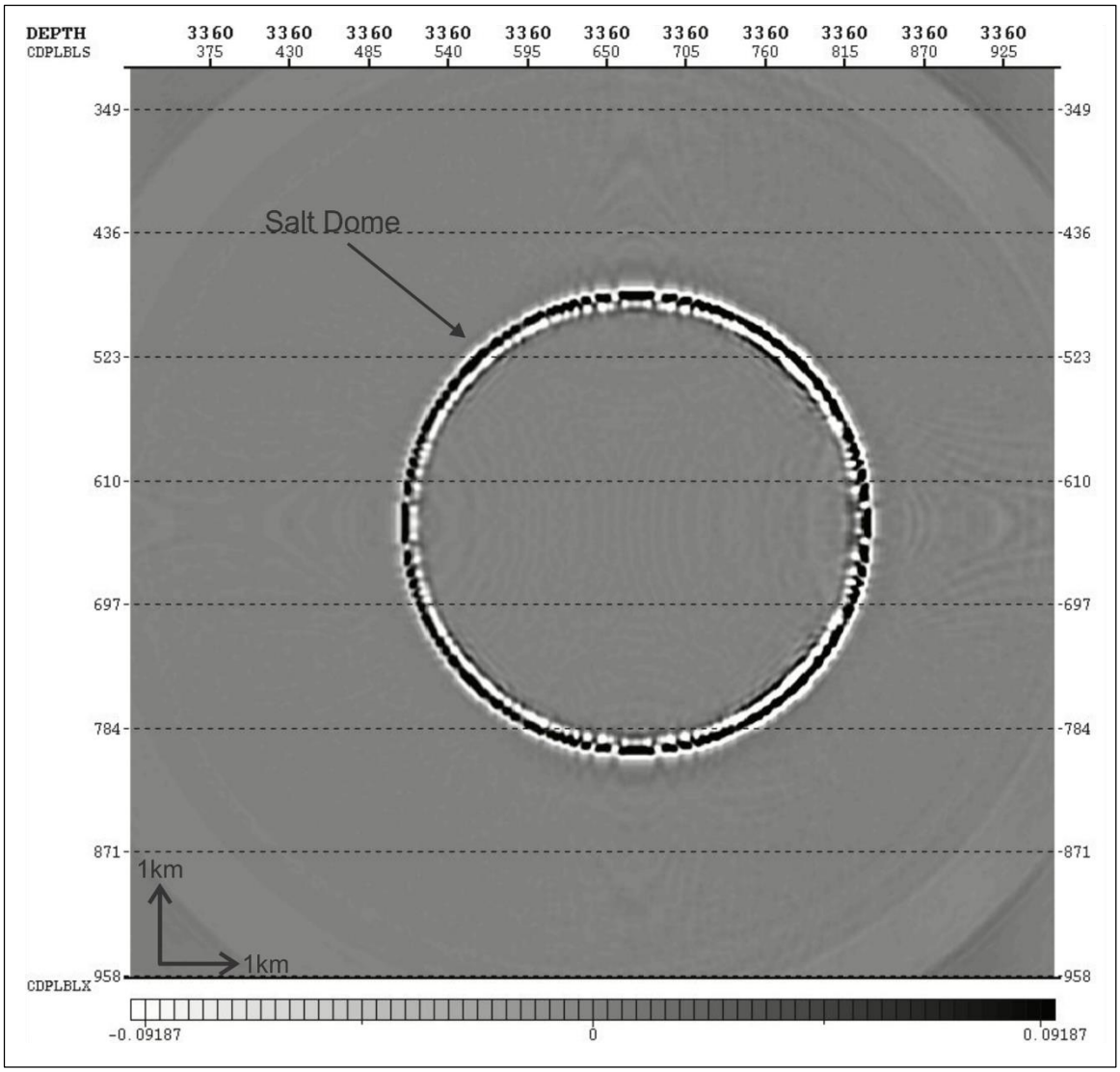

Figure 3.65. Depth slice image at 3360 m. Circular reflection represents the boundary of the salt almost bottom of the model.

CHAPTER FOUR: DISCUSSION

Two-D and 3-D seismic acquisition modelling studies in the Pierce Junction salt dome area were performed in order to find out the optimum parameters for cost effective surveys while meeting the imaging objectives. Moreover, the surveys were designed considering the limited equipment of the Allied Geophysical Laboratories (AGL) which has facilities like small companies and research institutions.

The proposed optimum survey parameters can be updated according to equipment capacity. Using less equipment than proposed for 2-D and 3-D surveys can prevent meeting the survey objectives.

In 2-D survey, decreasing the number of geophones using larger station intervals would cause aliasing issues, resulting low lateral resolution. On the other hand, reducing the maximum offset of the survey would result poor images due to the lack of offset contribution, especially from dipping layers. Using larger shot intervals would reduce the cost of the survey. However, the quality of the data will also decrease, since the maximum fold of the survey is diminished. Consequently, a survey designer whose objective is to image the area in 2-D adequately should use proposed parameters. Otherwise, the data will not meet the imaging objectives.

The number of geophones needed for the proposed optimum survey parameters in 3-D is 1573, an affordable number for a small company or research institution. The only way to decrease the number of geophones used in the patch is to decrease the aspect ratio.

An aspect ratio of 1:1 is recommended for 3-D survey in study are in order to obtain good offset and azimuth distributions. Narrow azimuth (aspect ratio of the patch is less than 0.5:1) surveys are not recommended since they provide limited range of azimuth and less uniform offset distribution while higher weights of far offsets are expected for better image quality (Cordsen et al., 2000). Therefore, although it is affordable as is, if the number of geophones is required to be reduced, it is better to keep aspect ratio higher than 0.5:1. Thus, the minimum number of geophones would be 968 for an aspect ratio of 0.6:1. Recording the seismic traces coming from every range of azimuth in the study area is quite important. Therefore, an aspect ratio of 1:1 is highly recommended for imaging the salt dome and the surrounding area.

The study area is situated in the middle of many busy highways, rail roads, and apartment complexes. Moreover, there are lots of oil producing wells and oil/gas storage facilities around. Hence, ambient noise in the area was the major problem for a seismic study. In this study, acquisitions were modelled without any noise addition to the raw shot gathers. The field tests applied before shooting the survey or available 2-D data can be helpful to determine the number of vertical stack to increase signal-to-noise-ratio. Increasing the maximum fold of the survey with higher shot density is another option to achieve better signal-to-noise-ratio.

RTM modeling has become more applicable with the recent advancements in computing technologies. Several companies leading the industry use this technique in many 3-D seismic projects. However, it is still counted as an expensive technique for small-scale

companies, since it requires powerful hardware along with a good storage capacity. This study has been done using Paradigm's powerful work stations. Recent improvements in computer systems and programming science will make this technique more viable for more common commercial use.

CHAPTER FIVE: LIMITATIONS OF THE STUDY

The main limitation of this study is the data unavailability for building a more accurate velocity model for the study area.

The two-D velocity model of the study area was built using 2-D seismic data acquired on the top of the salt, geological east-west cross section drawn by Glass (1953), and previous studies about Gulf Coast salt domes and sediments. However, there is no available documentation about the study area other than Glass (1953). Additional 2-D seismic data from sides of the salt dome would provide detailed velocity information to increase the complexity of the model by inserting sub-layers and velocity gradients. Also, an extensive geological cross section would provide thickness and dipping information about the layers. Moreover, petrophysical properties of the layers would affect the velocity building part of the study significantly.

A classic circular piercement salt dome shape having the dimensions of the Pierce Junction salt dome was used in 3-D velocity model. Also, horizons around the salt were created rotating the 2-D velocity model 360° around the origin. In order to build an accurate 3-D velocity model of the study area, sufficient number of well logs and 2-D seismic information around the salt dome and adequately sampled 3-D gravity data for modelling the shape of the salt dome and its surroundings are also required.

CHAPTER SIX: SUMMARY AND CONCLUSION

In conclusion, the optimum seismic survey parameters to image the Pierce Junction Salt dome and its surrounding sediments adequately in both 2-D and 3-D were determined by acquisition modeling. The velocity models of the study area were built with the help of the available data and previous studies. The synthetic raw shot gathers were created by finite difference method using full (two-way) acoustic wave equation and pre-stack imaging using Reverse Time Migration (RTM).

Instead of calculating the survey parameters with basic survey design formulas, 2-D survey parameters, such as maximum offset, group and shot interval, recording time, and profile length, were determined by observations on the final RTM images. However, the initial survey design parameters were calculated using basic formulas. Afterwards, the parameters were updated according to limited geophysical equipment of the Allied Geophysical Laboratories (AGL) while preserving the desirable image quality. Finally, it was proposed that a conventional 2-D survey can be performed using 150 geophones with 20 m interval and 200 shots with 40 m interval. The length of the receiver line (11 km) was chosen longer than shot profile (8 km) in order to have a good full-fold distribution. Although the maximum fold of the survey is high enough, the number of vertical stacks can be increased performing field tests in the real survey environment.

Once the optimum parameters for a 2-D seismic survey determined, they were adapted to the 3-D survey. The 3-D survey with orthogonal geometry was planned for an 8 km by 8

km square area. Thirty-three in-lines and 33 cross-lines were distributed over the survey area with 250 m intervals. The patch is the most important factor that determines the equipment requirements of a survey. The receiver interval of the patch was determined as 25 m for balancing the cost and imaging objectives of the survey. Consequently, it was proposed that minimum 1573 geophones are needed to image the study area adequately. Reducing the number of the geophones is possible by decreasing the aspect ratio of the patch. But, it is not recommended, since the poor azimuth and offset distributions will adversely affect the image resolution.

REFERENCES

Bain, R. C. (2010). Hidden Structure Revealed by a Simple 3D Velocity Model—McAllen Ranch Field, Hidalgo County, Texas. Gulf Coast Association of Geological Societies Transactions, v. 60, 39-55.

Barton, D. C. (1933). Mechanics of formation of salt domes with special reference to Gulf Coast salt domes of Texas and Louisiana. AAPG Bulletin, 17(9), 1025-1083.

Baysal, E., Kosloff, D. D., and Sherwood, J. W. (1983). Reverse time migration. Geophysics, 48(11), 1514-1524.

Beckman, J. D., and Williamson, A. K. (1990). Salt dome locations in the gulf coastal plain, south-central United States: US Geological Survey. Water-Resources Investigations Report, 90-4060.

Boyd, T. M., 2003. Introduction to Geophysical Exploration. [Online] Available at: http://galitzin.mines.edu/INTROGP/ [Accessed December 2010].

Carmichael, R. S. (1984). CRC handbook of physical properties of rocks. Volume III. CRC Press.

Castagna, J. P., Batzle, M. L., and Eastwood, R. L. (1985). Relationships between compressional-wave and shear-wave velocities in clastic silicate rocks. Geophysics, 50(4), 571-581.

Chaouch, A., and Mari, J. L. (2006). 3-D Land Seismic Surveys: Definition of Geophysical Parameter. Oil & Gas Science and Technology-Revue de l'IFP,61(5), 611-630.

Claerbout, J. F. (1985). Fundamentals of geophysical data processing.

Cordsen, A. (1995). Arrangement of source and receiver lines for three-dimensional seismic data acquisition. U.S. Patent No. 5,402,391. Washington, DC: U.S. Patent and Trademark Office.

Cordsen, A., Galbraith, M., and Peirce, J. (2000). Planning land 3-D seismic surveys (Vol. 9). B. A. Hardage (Ed.). Tulsa: Society of Exploration Geophysicists.

Darton, N. H. (1933). Guidebook of the Western United States: Part F. The Southern Pacific Lines, New Orleans to Los Angeles (Vol. 845). US Government Printing Office.

Ebrom, D., Li, X., McDonald, J., and Lu, L. (1995). Bin spacing in land 3-D seismic surveys and horizontal resolution in time slices. The Leading Edge, 14(1), 37-40.

Embree, P. (1985). Resolutions and rules of thumb. Seismic Field Techniques Workshop.

Ewing, T.E., Tyler, N., and Morton, R.A. (1983). Consolidation of geologic studies of geopressured geothermal resources in Texas. United States Department of Energy 1983 Annual Report, Contract No. ACOS-79ET27111.

Ewing, T. E., 1991. Structural framework. In: Salvador, A. (1991). Origin and development of the Gulf of Mexico basin. The Gulf of Mexico Basin, 389-444.

Freeland, J. M., and Hogg, J. E. (1990). “What does migration do to seismic resolution?”. Canadian Society of Exploration Geophysics, Recorder, Sept 1990.

Feely, H. W., and Kulp, J. L. (1957). Origin of Gulf Coast salt-dome sulphur deposits. AAPG Bulletin, 41(8), 1802-1853.

Glass, N.C. (1953). Pierce Junction field, Harris County Texas. Guidebook, field trip routes, oil fields, geology, Houston Geological Society.

Gore, R.H. (1992). The Gulf of Mexico. Pineapple Press, Inc. Sarasota Florida. 384 p.

Goupillaud, P., Grossmann, A., and Morlet, J. (1984). Cycle-octave and related transforms in seismic signal analysis. Geoexploration, 23(1), 85-102.

Halbouty, M. T., and Hardin, G. C. (1956). Genesis of salt domes of Gulf Coastal Plain. AAPG Bulletin, 40(4), 737-746.

Halbouty, M. T. (1967). Salt Domes: Gulf Region, United States, & Mexico. Gulf Publishing Company.

Halbouty, M.T. (1979). Salt domes of Gulf Region, United States and Mexico, 2nd ed. Houston, Texas: Gulf Publishing Company

Holzer, T. L., and Bluntzer, R. L. (1984). Land Subsidence Near Oil and Gas Fields, Houston, Texas. Ground Water, 22(4), 450-459.

Huang, Z. Y. (2012). Multidisciplinary investigation of surface deformation above salt domes in Houston, Texas: Master Thesis, University of Houston.

Hudec, M. R., and Jackson, M. (2007). Terra infirma: Understanding salt tectonics. Earth-Science Reviews, 82(1), 1-28.

Huffman, A. C. (2004). Salt Diapirs in the Gulf Coast. U.S. Geological Survey, DS-90, ver 1.0.

Jackson, M. T., and Talbot, C. J. (1986). External shapes, strain rates, and dynamics of salt structures. Geological Society of America Bulletin, 97(3), 305-323.

Jiao, K., Huang, W., Denes, V., Kapoor, J., Coates, R., Starr, E.W., Cheng, X. (2012). Elastic migration for improving salt and subsalt imaging and inversion. 82nd Annual International Meeting Society of Exploration Geophysicists.

Konyukhov, A. I. (2008). Geological structure, evolution stages, and petroliferous complexes of the Gulf of Mexico basin. Lithology and Mineral Resources, 43(4), 380-393.

Krey, T. C. (1987). Attenuation of random noise by 2-D and 3-D CDP stacking and Kirchhoff migration. Geophysical prospecting, 35(2), 135-147.

Kupfer, D.H. (1989). Diapirism sequences as indicated by internal salt structures. Gulf Coast Section Society of Economic Paleontologists and Mineralogists Foundation Tenth Annual Research Program and Abstracts, p.79-89.

Kyle, J. R., Ulrich, M. R., and Gose, W. A. (1987). Textural and paleomagnetic evidence for the mechanism and timing of anhydrite cap rock formation, Winnfield salt dome, Louisiana. Dynamical geology of salt and related structures: Academic Press, Inc., New York, New York, 497-542.

Lash, C. C. (1980). Shear waves, multiple reflections, and converted waves found by a deep vertical wave test (vertical seismic profiling). Geophysics, 45(9), 1373-1411.

Liner, C. (2004). Elements of Three-D Seismology. PennWell Books.

Margrave, G. F. (1997, November). Seismic acquisition parameter considerations for a linear velocity medium. In 1997 SEG Annual Meeting.

Moritz, H. (1980). Geodetic reference system 1980. Journal of Geodesy, 54(3), 395-405.

Morlet, J., Arens, G., Fourgeau, E., and Glard, D. (1982). Wave propagation and sampling theory-Part I: Complex signal and scattering in multilayered media. Geophysics, 47(2), 203-221.

Murray, G. E. (1961). Geology of the Atlantic and Gulf coastal province of North America (p. 692). New York: Harper.

Neff, W. H., and Rigdon, H. K. (1994). Incorporating structure into 3D seismic survey preplanning: A mid-continent example. Presented at the MESA Technology Conference.

Nelson, T. H. (1991). Salt tectonics and listric-normal faulting. The Gulf of Mexico Basin: Geological Society of America, The Geology of North America, v. J, 73-89.

Nettleton, L. L. (1934). Fluid mechanics of salt domes. AAPG Bulletin, 18(9), 1175-1204.

Nettleton, L. L. (1976). *Gravity and magnetics in oil prospecting* (Vol. 464). New York: McGraw-Hill.

Oezsen, R. (2004). Velocity modelling and prestack depth imaging below complex salt structures: a case history from on-shore Germany. Geophysical prospecting, 52(6), 693-705.

Oppenheim, A. V., Schafer, R. W., and Buck, J. R. (1999). Discrete-time signal processing (Vol. 5). Upper Saddle River: Prentice Hall.

Otoum, M. A. (2011). An Integrated Geophysical Investigation to Map the Hockley Active Fault in Northwest Harris County, Texas (Doctoral dissertation, University of Houston).

Parra, O.J. and Collier, H.A. (1997). Petrophysical properties and geology of selected intervals in the Frio formation, Stratton field for modeling interwell seismic logging responses. SPWLA 38th Annual Logging Symposium.

Partyka, G., Gridley, J., and Lopez, J. (1999). Interpretational applications of spectral decomposition in reservoir characterization. The Leading Edge, 18(3), 353-360.

Posey, H. H., and Kyle, J. R. (1988). Fluid-rock interactions in the salt dome environment: an introduction and review. Chemical geology, 74(1), 1-24.

Prieto, C. (2000). Gravity/magnetic signatures of various geologic models-an exercise in pattern recognition. Geophysical References Series, 8, 20-27.

Robinson, E.A., and Treitel, S. (1980). Geophysical Signal Analysis, Prentice Hall, Englewood Cliffs, N.J.

Querio, C. W. (1974). Simultaneous Storage of LPG and Production of Brine, Pierce Junction Dome, Houston, Texas. In Fourth Symposium on Salt (Vol. 2, p. 285). Northern Ohio Geological Society.

Salvador, A. (1991). Origin and development of the Gulf of Mexico basin. The Gulf of Mexico Basin, 389-444.

Seigel, H. O., Brcic, I., and Mistry, P. (1995). A guide to high precision land gravimeter surveys. Scintrex LTD, Concord, Ontraio.

Seni, S. J., Mullican, W. F., and Hamlin, H. S. (1984). Texas Salt Domes--Aspects Affecting Disposal of Toxic-chemical Waste in Solution-mined Caverns. Bureau of Economic Geology, University of Texas at Austin.

Sheriff, R. E. (2002). In Encyclopedic Dictionary of Applied Geophysics. Society of Exploration Geophysicists.

Stone, D. G. (1994). Designing seismic surveys in two and three dimensions (Vol. 5). Soc of Exploration Geophysicists.

Taner, M. T., Koehler, F., and Sheriff, R. E. (1979). Complex seismic trace analysis. Geophysics, 44(6), 1041-1063.

Thomas, R. L., and Gehle, R. M. (2000). A brief history of salt cavern use. In Proc. 8th World Salt Symposium. [S. l.]: Elsevier (pp. 207-214).

Vermeer, G. J. (1998). 3-D symmetric sampling in theory and practice. The Leading Edge, 17(11), 1514-1519.

Vermeer, G. J. (1999). Factors affecting spatial resolution. Geophysics, 64(3), 942-953.

Vermeer, G. J. O. (2002) 3-D Seismic survey design. Society of Exploration Geophysicists Geophysical References Series 12, Tulsa, Oklahoma, 205 p.

Willis, M. E., Lu, R., Campman, X., Nafi Toksöz, M., Zhang, Y., and Hoop, M. V. D. (2006). A novel application of time-reversed acoustics: Salt-dome flank imaging using walkaway VSP surveys. Geophysics, 71(2), A7-A11.

Wright, S. (2003). Is the 3-D Survey 'Good Enough?'. AAPG Explorer, June 2003.